ISJET

INTERNATIONAL SCIENTIFIC JOURNAL OF ENGINEERING AND TECHNOLOGY

Volume 9 No. 2 July-December 2025

ISSN 2586-8527 (Online)

Panyapiwat Institute of Management

Indexed in the Thai-Journal Citation Index (TCI 1)

INTERNATIONAL SCIENTIFIC JOURNAL OF ENGINEERING AND TECHNOLOGY (ISJET)

Volume 9 No. 2 July-December 2025

ISSN 2586-8527 (Online)
PANYAPIWAT INSTITUTE OF MANAGEMENT

INTERNATIONAL SCIENTIFIC JOURNAL OF ENGINEERING AND TECHNOLOGY (ISJET)
Volume 9 No. 2 July-December 2025
ISSN 2586-8527 (Online)

Panyapiwat Institute of Management
85/1 Moo 2, Chaengwattana Rd.,
Bang Talat, Pakkred,
Nonthaburi, 11120, Thailand
Tel. +66 2855 1560
E-mail: isjet@pim.ac.th
Website: https://ph02.tci-thaijo.org/index.php/isjet/index

INTERNATIONAL SCIENTIFIC JOURNAL OF ENGINEERING AND TECHNOLOGY (ISJET)

Volume 9 No. 2 July-December 2025 ISSN 2586-8527 (Online)

Objective:
International Scientific Journal of Engineering and Technology will be dedicated to serving as a forum to share knowledge on research advances in all fields of sciences: Engineering, Technology, Innovation, Information Technology, Management Information Systems, Logistics and Transportation, Agricultural Science and Technology, Animal Science and Aquaculture, Food Science, and other areas in Sciences and Technology. Submissions are welcomed from both PIM as well as other Thai and foreign institutions.

Scope:
Engineering, Technology, Innovation, Information Technology, Management Information Systems, Logistics and Transportation, Agricultural Science and Technology, Animal Science and Aquaculture, Food Science, and other areas of Sciences and Technology.

Type of Article:
• Research article
• Academic article
• Review article

Languages of academic works:
An article written in either English language is accepted for publication.

Reviewing Policy:
1. Any manuscript to be accepted for publication must have been reviewed and approved by at least three peer reviewers in that particular field or related fields. The Journal has a double-blind peer review policy which means that neither the peer reviewer nor the author knows the identity of each other.
2. The submitted manuscript must have never been published in any other periodical, and must not be in the approving process for publication by any other periodical. Also, the author must not plagiarize the work of other people.
3. The article, expression, illustrations, and tables that are published in the Journal are the sole responsibility of the author, and definitely not that of Panyapiwat Institute of Management.
4. The Editorial Board of International Scientific Journal of Engineering and Technology reserves the right to change or revise the name(s) and unit(s) of the author(s) in all cases after the issuance of the letter.
5. The Editorial Board of International Scientific Journal of Engineering and Technology reserves the right to cancel the publication that has been issued a certification of publication in the Journal.
6. The Editorial Board of International Scientific Journal of Engineering and Technology reserves the right for decision making on publishing any article in the Journal.

Frequency of Publication:
Twice a year
• The first issue: January-June
• The second issue: July-December

Publication and Access Charges:
There are no charges to submit and publish all types of articles. Full articles in PDF format can be downloaded free from the journal website at https://ph02.tci-thaijo.org/index.php/isjet/index

ISJET Journal Editorial Board
The office of Research and Development
Panyapiwat Institute of Management
85/1 Moo 2, Chaengwattana Rd.,
Bang Talat, Pakkred, Nonthaburi, 11120, Thailand
Tel. +66 2855 1560
E-mail: isjet@pim.ac.th
Website: https://ph02.tci-thaijo.org/index.php/isjet/index

INTERNATIONAL SCIENTIFIC JOURNAL OF ENGINEERING AND TECHNOLOGY (ISJET)
Volume 9 No. 2 July-December 2025
ISSN 2586-8527 (Online)

INTERNATIONAL SCIENTIFIC JOURNAL OF ENGINEERING AND TECHNOLOGY (ISJET)
Volume 9 No. 2 July-December 2025
ISSN 2586-8527 (Online)

Peer Reviewers

Prof. Dr. Parames Chutima	Chulalongkorn University, Thailand
Assoc. Prof. Dr. Charnnarong Saikaew	Khon Kaen University, Thailand
Assoc. Prof. Dr. Chotirat Ratanamahatana	Chulalongkorn University, Thailand
Assoc. Prof. Dr. Nattapon Chantarapanich	Kasetsart University Sriracha Campus, Thailand
Assoc. Prof. Dr. Nivit Charoenchai	Chiang Mai University, Thailand
Assoc. Prof. Dr. Panomkhawn Riyamongkol	Naresuan University, Thailand
Assoc. Prof. Dr. Papot Jaroenapibal	Khon Kaen University, Thailand
Assoc. Prof. Dr. Patomsok Wilaipon	Naresuan University, Thailand
Assoc. Prof. Dr. Werasak Kurutach	Mahanakorn University of Technology, Thailand
Asst. Prof. Dr. Chorkaew Jaturanonda	King Mongkut's University of Technology Thonburi,Thailand
Asst. Prof. Dr. Jaratsri Rungrattanaubol	Naresuan University, Thailand
Asst. Prof. Dr. Khajitpan Makaratat Kritpolviman	Sukhothai Thammathirat Open University, Thailand
Asst. Prof. Dr. Manachai Toahchoodee	University of the Thai Chamber of Commerce, Thailand
Asst. Prof. Dr. Narongdech Keeratipranon	Chulalongkorn University, Thailand
Asst. Prof. Dr. Thanawin Rakthanmanon	Kasetsart University, Thailand
Asst. Prof. Dr. Udsanee Pakdeetrakulwong	Nakhon Pathom Rajabhat University, Thailand
Asst. Prof. Satien Janpla	Suan Sunandha Rajabhat University, Thailand
Dr. Kwankamon Dittakan	Prince of Songkla University, Thailand

INTERNATIONAL SCIENTIFIC JOURNAL OF ENGINEERING AND TECHNOLOGY (ISJET)
Volume 9 No. 2 July-December 2025
ISSN 2586-8527 (Online)

Dear Colleagues,

Welcome to this latest volume of The International Scientific Journal of Engineering and Technology (ISJET). It is with great pleasure that we present a collection of papers that exemplify our mission: To highlight rigorous, innovative, and practical research addressing contemporary challenges. This volume showcases the sheer breadth of modern engineering. We feature advancements in m-Health with an IoT-based system for Foot Drop; enhancements in logistics via K-means clustering for Vehicle Routing; and AI-driven quality control with Shrimp Weight Anomaly detection. Further, we explore Industry 4.0 with Low-Cost Digitization in semiconductor manufacturing; foundational mechanical engineering with the optimization of Tricycle (Tuk-Tuk) Suspension systems; and critical security research on Physical Interference Attacks on Autonomous Driving. These papers collectively illustrate the power of applying intelligent and connected technologies to solve specific, practical problems. We extend our sincere gratitude to all the authors and to our dedicated community of reviewers whose expertise was essential in shaping this volume.

We trust you will find these articles insightful and inspiring. As we continue to advance the discourse in our field, we warmly invite researchers and practitioners to submit their own high-quality, original articles to ISJET. We look forward to sharing your novel work with the global engineering community.

With kind regards,
Assoc. Prof. Dr. Parinya Sanguansat
Editor-in-chief
isjet@pim.ac.th

INTERNATIONAL SCIENTIFIC JOURNAL OF ENGINEERING AND TECHNOLOGY (ISJET)
Volume 9 No. 2 July-December 2025
ISSN 2586-8527 (Online)

CONTENTS

- **Design and Development of a Wireless Functional Electrical Stimulation and m-Health Application for Foot Drop Using an IoT-Based Architecture** 1
  Jirawat Jitprasutwit, Anan Banharnsakun, Kathawach Satianpakiranakorn and Kanjana Eiamsaard

- **Enhancing Vehicle Routing with Time Windows Solutions via K-means Clustering: A Comparative Study of Elbow and Truck Utilization Methods** 18
  Kanokporn Boonjubut, Prat Boonsam, and Sirichai Yodwangjai

- **Intelligent Mobile-Based Detection of Shrimp Weight Anomalies Using Random Forest Regression** 30
  Kanjana Eiamsaard, Kathawach Satianpakiranakorn, Anan Banharnsakun and Jirawat Jitprasutwit

- **Low-Cost Digitization for Monitoring Manual Processes: A Case Study of Tray Cleaning in Semiconductor Manufacturing** 41
  Pathitta Timtong, Pornnapat Kwanboonya, and Warut Pannakkong

- **Optimizing Tricycle (Tuk-Tuk) Suspension Systems Using Mathematical Modeling** 49
  Chaiyawoot Narintharangkul and Poom Jatunitanont

- **Physical Interference Attacks on Autonomous Driving** 64
  Chuanxiang Bi and Jian Qu

Design and Development of a Wireless Functional Electrical Stimulation and m-Health Application for Foot Drop Using an IoT-Based Architecture

Jirawat Jitprasutwit[1], Anan Banharnsakun[2], Kathawach Satianpakiranakorn[3] and Kanjana Eiamsaard[4*]

[1,2,3,4]Department of Computer Engineering, Faculty of Engineering at Sriracha, Kasetsart University Sriracha Campus, Thailand

Email : jirawat@eng.src.ku.ac.th, ananb@ieee.org, kathawach@eng.src.ku.ac.th, kanjana@eng.src.ku.ac.th*

Received: May 30,2025 / Revised: September 29, 2025 / Accepted: October 20, 2025

***Abstract*—To enhance accessibility in foot drop rehabilitation, this study presents the design and development of a wireless functional electrical stimulation system integrated with a mobile health (m-Health) application and an ESP32-based IoT (Internet of Things) platform. The system comprises a stimulation node and a sensor node that communicate via Bluetooth Low Energy (BLE) for heel-strike-triggered stimulation. The stimulation node delivers symmetrical biphasic pulses to the peroneal nerve with adjustable parameters. A cloud-based backend using MQTT supports real-time logging and device management, while the m-Health application enables mode selection, parameter tuning, and usage tracking. Key hardware includes a 70V boost converter, programmable current limiter, and H-bridge pulse generator. Evaluations show reliable pulse output (400.3 µs width, 2.1 µs rise/fall), low BLE latency (6.16 ms), and accurate analog-to-digital converter readings. Results confirm the system's feasibility as a compact, portable solution for home-based rehabilitation, addressing limitations of traditional wired systems.**

***Index Terms*— Functional Electrical Stimulation (FES), Foot Drop, Home-based Rehabilitation, Wireless Sensor, Biphasic Pulse Generation, IoT, Embedded System, m-Health Application**

I. Introduction

Stroke remains one of the leading causes of long-term disability worldwide, especially among the elderly and individuals with underlying conditions such as diabetes and hypertension. According to the World Health Organization (WHO) in 2022, nearly 15 million people suffer a stroke each year, with more than 5 million experiencing significant motor impairments that affect their ability to perform daily activities such as grasping, standing, and walking [1], [2].

One of the most common post-stroke complications is foot drop, a condition in which patients are unable to lift the front part of their foot due to muscle weakness or paralysis. This impairment causes the toes to drag while walking, increasing the risk of falling and significantly impacting mobility and independence [2]. To handle foot drop, patients often rely on Ankle-Foot Orthoses (AFOs), which help position the foot during gait. However, prolonged use of AFOs may lead to muscle atrophy from disuse [3]. Functional Electrical Stimulation (FES) offers an alternative by applying timed electrical impulses to the affected muscles or nerves, typically triggered by sensors placed on the heel while walking. In addition to improving gait by enabling dorsiflexion during the swing phase, FES has been shown to prevent muscle atrophy and support motor relearning through enhanced neuroplasticity [4]-[6]. Recent clinical studies have demonstrated that FES can improve walking speed, endurance, and balance in stroke survivors with foot drop, contributing to long-term improvements in mobility and functional independence [7]-[9]. Other treatments include physical therapy, muscle strengthening exercises, and surgical interventions when necessary [10].

A prior study developed and distributed a functional electrical stimulator for foot drop patients through regional hospitals in Thailand [11]. Subsequent clinical research conducted using that system demonstrated its effectiveness in improving walking speed and mobility among patients [4], [5]. Building upon the clinically validated Dearndee FES system previously distributed in regional hospitals, this study introduces a new wireless platform aimed at improving mobility and user engagement through modern IoT and mobile health technologies.

In response to these challenges, this study presents the design and development of a compact, wireless

FES system intended to assist individuals with foot drop. The proposed system comprises a stimulator node that delivers electrical pulses to the peroneal nerve area, a sensor node that detects heel pressure during walking, and a mobile application for device control and monitoring. Communication between nodes is achieved through Bluetooth Low Energy (BLE), supporting real-time, cable-free interaction among system components.

The design emphasizes technical aspects through the integration of custom-designed hardware, firmware, and wireless communication protocols to ensure low-latency performance and accurate electrical stimulation. A microcontroller is utilized to generate precise stimulation waveforms and manage synchronized communication between the sensor and stimulator nodes. In addition, the Mobile Health (m-Health) application is developed not only as a user interface but also as a platform for data logging and remote configuration. It is designed based on the Mobile Health (m-Health)Technology Acceptance Model (MoHTAM) [12], and follows guideline themes for Mobile Health system usability and accessibility as proposed in [13], ensuring that it meets standards for practical deployment in real-world scenarios.

While this paper does not involve human trials to avoid ethical concerns, this study demonstrates the system's technical feasibility and performance through electrical measurements, establishing a foundation for future home-based rehabilitation applications and clinical validation.

II. Background and Knowledge

This section outlines the foundational principles and design considerations underlying the proposed system, encompassing the FES methodology, electrical signal parameters, microcontroller platform, and mobile health application integration.

A. Functional Electrical Stimulation

FES applies electrical pulses to peripheral nerves to induce muscle contractions for restoring specific motor functions. For foot drop, FES stimulates the common peroneal nerve to activate dorsiflexion during gait, aiding mobility and preventing muscle atrophy. This study focuses on its application in gait rehabilitation for stroke patients [14], [15].

B. Electrical Signal Parameters

The effectiveness of FES depends heavily on how the electrical signals are configured. In this study, stimulation signals are designed based on three key parameters: Waveform, frequency, and pulse characteristics, including durtion and Intensity.

- Waveform

A symmetrical biphasic waveform was used to reduce skin irritation and prevent charge buildup, providing balanced current flow and improved comfort. Its symmetry supports precise motor unit activation, crucial for functions like foot dorsiflexion. Controlled waveform parameters also enhance stimulation selectivity and reduce fatigue [16], [17] holding a toothbrush, standing, and walking. The technology was developed in the sixties, during which initial clinical use started, emphasizing its potential as an assistive device. Since then, functional electrical stimulation has evolved into an important therapeutic intervention that clinicians can use to help individuals who have had a stroke or a spinal cord injury regain their ability to stand, walk, reach, and grasp. With an expected growth in the aging population, it is likely that this technology will undergo important changes to increase its efficacy as well as its widespread adoption. We present here a series of functional electrical stimulation systems to illustrate the fundamentals of the technology and its applications. Most of the concepts continue to be in use today by modern day devices. A brief description of the potential future of the technology is presented, including its integration with brain–computer interfaces and wearable (garment. Fig. 1 illustrates the waveform structure implemented in the system.

- Frequency

The stimulation frequency directly influences the nature of muscle contraction. Frequencies in the range of 40 Hz to 100 Hz were considered optimal for producing tetanic muscle contractions, which are essential for effective foot lifting [11], [17]. Frequencies outside the optimal range can cause either fatigue or weak contractions, so the system allows real-time frequency adjustment based on patient response.

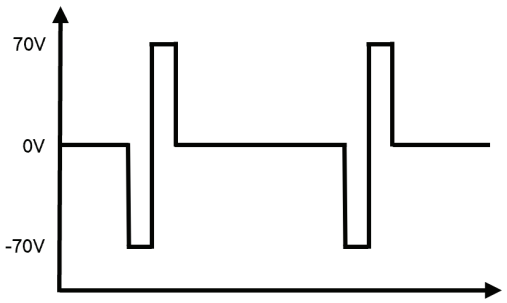

Fig. 1. A symmetrical biphasic waveform

- Pulse Duration and Intensity

Pulse duration and intensity are key to effective muscle activation, but individual differences require adjustable settings. This system allows tuning of pulse width and voltage, typically using 100-1000 µs pulses, 10-100 Hz frequency, and 60-70 V output [11], [17]. Parameters were chosen through initial testing to balance effective contraction with user comfort and minimal fatigue [18]. Stimulation parameters are adjustable in real time to match individual responses and reduce overstimulation risk.

C. Microcontroller and BLE Communication

The system employs the ESP32 microcontroller, which features a dual-core Xtensa LX6 processor operating at up to 240 MHz, with integrated Wi-Fi and BLE capabilities. ESP32 was selected over platforms such as nRF52, STM32, or Arduino due to its unique combination of built-in wireless connectivity, low cost, dual-core architecture, and native support for real-time task scheduling via Free RTOS. This architecture enables the system to handle concurrent operations efficiently, with BLE controller tasks assigned a high priority to meet real-time requirements [19]. BLE enables low-latency, energy-efficient communication between components, which is crucial for synchronized stimulation and sensing [20]. Its implementation using ESP32 modules is detailed in the hardware design section.

III. Literature Review

Functional electrical stimulation has long been established as a rehabilitative solution for foot drop, particularly among stroke survivors and individuals with neurological disorders. Over the past decade, significant advancements in embedded systems, sensor technologies, and wireless communication have influenced the design of both academic and commercial FES systems, aiming to improve usability, adaptability, and accessibility.

Early academic implementations of FES focused on basic stimulation functionality. Bhattacharya and Manjunatha reviewed microcontroller-based FES systems with capabilities for precise current modulation but noted that such systems often lacked real-time personalization and mobile connectivity, which limited their practical usability in home rehabilitation settings [21]. Jitprasutwit *et al*. presented a culturally adapted, cost-sensitive FES system for Thai users, utilizing wired stimulation without advanced feedback or wireless features [11]. Melo *et al*. advanced FES control by incorporating continuous motion feedback from the foot, allowing real-time modulation of stimulation patterns during gait [22]. The emergence of wireless technology, particularly BLE, led to portable and user-friendly system designs. Watanabe et al. developed a portable FES rehabilitation prototype featuring inertial sensors for gait event detection and Bluetooth communication with a tablet, enabling stimulation based on real-time sensor data [23]. Aqueveque *et al*. introduced a capacitive step sensor positioned under the heel, which achieved accurate real-time detection of swing-phase transitions and transmitted synchronization signals wirelessly, enhancing timing precision for stimulation delivery [24]. Additionally, York and Chakrabarty conducted a comprehensive survey highlighting the clinical effectiveness of FES in improving walking speed, quality of life, and patient preference over alternatives like AFOs, though challenges remained with system cost and sensory feedback integration [25].

In the past five years, low-cost, open-platform FES solutions have gained traction in academic research. Kipli et al. developed an Arduino Nano-based FES prototype suitable for educational or prototyping purposes, focusing on simplicity and affordability, but lacking advanced features such as mobile connectivity or AI-assisted control [26]. De Almeida et al. presented a 4-channel IoT-enabled electro stimulator using ESP32, capable of closed-loop joint angle control via inertial feedback and MQTT protocol, though it did not integrate a mobile application [27]. Gangadharan et al. introduced an intelligent system with sensor-based auto-triggering to enhance timing precision [28]. Chiriac et al. followed with a design focused on cost-effectiveness and usability in low-resource environments, though the system remained basic in function and lacked BLE or application integration [29]. Most recently, Cao et al. proposed a wearable ultrasound-FES integrated system capable of high-accuracy intention recognition using muscle thickness detection. This allowed precise real-time control of stimulation, although no mobile application or user interface for direct interaction was described [30].

In parallel, several commercial systems have been developed with higher performance but significantly higher costs. The Bioness L300 Go, for instance, integrates 3D motion sensors and mobile connectivity to optimize stimulation timing but is priced over $6,000 [31]. The WalkAide uses tilt sensors for gait detection and real-time stimulation but lacks mobile programmability [32]. Meanwhile, XFT-2001D, marketed as a semi-intelligent foot drop stimulator, features MEMS sensors and AI algorithms for adaptive output, with mobile application control, at a cost exceeding $2,199 [33].

In terms of intellectual property, patents such as US20170106189A1 present a system with multi-pad electrodes and movement sensors for adaptive stimulation control [34], while US11406821B2 outlines a compact, waterproof, stainless-steel integrated apparatus with ergonomic design features aimed at long-term usability [35].

Existing FES systems often trade off between cost and functionality. Commercial devices offer advanced features but lack flexibility, while academic prototypes are affordable yet limited in control and connectivity. This study proposes an IoT-based FES system with BLE-triggered stimulation, adjustable parameters, application control, and cloud monitoring to bridge that gap.

IV. Research Methodology

This study follows an engineering design research methodology to evaluate the feasibility of a wireless Functional Electrical Stimulation (FES) system for foot drop rehabilitation. The methodology was structured into five main stages.

A. Research Framework

The research focused on designing, prototyping, and validating a compact wireless FES system without human trials. The objective was to demonstrate technical feasibility through engineering tests of system components, communication performance, and power efficiency.

B. Hardware Methodology

The hardware was developed using a modular approach that separated the system into a stimulation node and a sensor node. The stimulation node was designed to generate programmable biphasic pulses, while the sensor node detected heel pressure and transmitted signals wirelessly through BLE. Both nodes were implemented on ESP32-based platforms due to their integrated wireless capability and suitability for real-time applications. This methodology enabled iterative prototyping and testing before full integration, while detailed hardware schematics and circuit descriptions are presented in Section V.

C. Firmware Methodology

The firmware was developed on the ESP32 platform with an interrupt-driven approach to achieve precise pulse timing and modular task organization to support real-time operation. Its main functions included pulse control, stimulation logic, BLE communication, and cloud connectivity, with implementation details described in Section V.

D. Mobile Application Methodology

The mobile application proposed in this study was constructed using the Agile development methodology. The process began with developing user stories related to rehabilitation activities. The most critical stories were then selected for development in the first iteration. After these stories were verified to be working properly, subsequent increments were developed until all user stories were completed. Finally, all functionalities were verified during the system testing process. Detailed application features and interfaces are presented in Section V.

E. Experimental Methodology

The evaluation was conducted through a structured set of experiments designed to validate system functionality. These included verification of the boost converter and current limiter circuits, assessment of waveform precision, benchmarking of ADC accuracy, measurement of BLE latency across multiple trials, and testing of battery life under continuous operation. Experiments were performed in a controlled environment using calibrated instruments to ensure accuracy. The complete setup and parameters are described in Section VI.

V. Proposed System Architecture and Design

The proposed FES system for foot drop consists of three components: A sensor node, a stimulation node, and an m-Health application. As shown in Fig. 2, the sensor node, placed near the ankle, detects foot plantar flexion and transmits real-time gait data to the stimulation node via BLE [24]. Upon receiving the trigger, the stimulation node delivers electrical stimulation to the common peroneal nerve to induce dorsiflexion and assist the user during the swing phase [4], [5], [25]. In addition to real-time stimulation control, the stimulation node collects usage data and periodically synchronizes with the cloud server, which serves as a remote repository for long-term storage and activity logging [36].

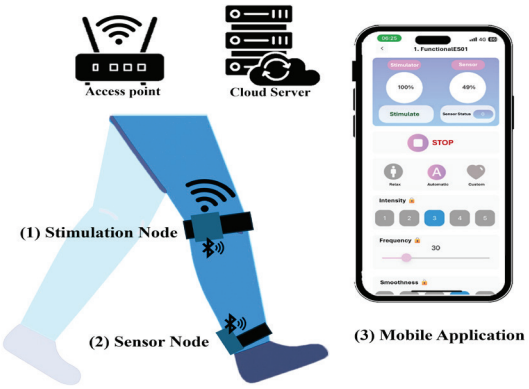

Fig. 2. System overview of the proposed FES platform for foot drop: (1) Stimulation Node for delivering electrical pulses, (2) Sensor Node for gait event detection, and (3) Mobile Application for parameter control and monitoring

The mobile application enables users or clinicians to configure stimulation parameters, monitor system performance, and visualize historical usage data. It serves as the primary interface for interacting with the system outside the stimulation hardware.

The system leverages BLE for communication between the sensor and stimulation nodes [24], while internet connectivity (via Wi-Fi or mobile hotspot) supports data exchange between the stimulation node, cloud server, and mobile application [36]. The cloud communication architecture follows IoT design principles [37], utilizing the MQTT protocol for real-time messaging with a Node-RED-based server and NoSQL database for user and session data storage [38].

When such a system is in an offline mode, the stimulation node operates using saved settings, with basic onboard adjustments.

This study focuses on system-level design across hardware, firmware, communication, and mobile interface. Initial tests evaluate latency, control response, parameter tuning, and data synchronization to support future clinical validation.

A. Hardware Design

The proposed FES system comprises two ESP32-based modules: a sensor node (M5StickC Plus) for heel-pressure detection and BLE signaling, and a stimulation node (M5Stack) for generating programmable biphasic pulses using boost, current limit, and pulse control circuits. As shown in Fig. 3, this compact design supports real-time, low-latency operation suitable for wearable FES applications.

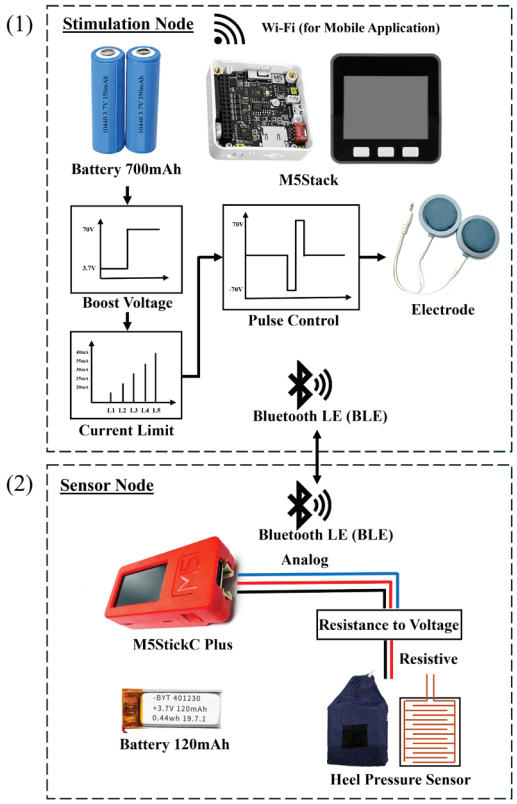

Fig. 3. Hardware architecture of the proposed FES system, consisting of (1) Stimulation Node and (2) Sensor Node

1) Stimulation Node Design

The stimulation node serves as the system's output module, delivering electrical pulses for gait rehabilitation. It is built on the M5Stack, which includes a dual-core ESP32, Wi-Fi/BLE, a 2.0-inch IPS LCD, and three user buttons [39]. This platform was chosen for its modularity and high level of integration, which allows for rapid prototyping and reduces the need for extensive peripheral circuit design [40], [41]. Although the default configuration includes a small internal battery, it was removed in this implementation to support an external 3.7 V 520 mAh lithium polymer battery, providing sufficient capacity for stimulation tasks.

The stimulation node integrates three main circuits: a boost converter (3.7 V to 70 V), a current limiter for user safety, and a pulse generator for symmetrical biphasic waveforms. These are managed by the ESP32, which handles BLE input from the sensor node and Wi-Fi communication with the cloud and mobile application. Physical switches on the M5Stack allow offline control and testing. Key specifications are shown in TABLE I, with the system structure illustrated in Fig. 3 (1).

TABLE I
TECHNICAL SPECIFICATIONS OF THE STIMULATION NODE HARDWARE

Feature	Stimulation Node	Sensor Node
Microcontroller	ESP32-D0WDQ6-V3 (240 MHz dual-core Xtensa 32-bit LX6, 520 KB SRAM)	ESP32-PICO-D4 (240 MHz dual-core Xtensa 32-bit LX6, 520 KB SRAM)
Platform	M5Stack [45]	M5Stick C Plus [46]
Flash Memory	4 MB	4 MB
Wireless Connectivity	Wi-Fi 802.11 b/g/n, Bluetooth 4.2 (BLE)	Wi-Fi 802.11 b/g/n, Bluetooth 4.2 (BLE)
Display	2.0 IPS TFT LCD, 320p×240p	1.14 IPS TFT LCD, 135p×240p
Interfaces	3x programmable buttons, USB Type-C, 26 GPIO pins, GROVE (I²C/UART)	1x programmable button, USB Type-C, 14 GPIO, GROVE (I²C/UART)
Battery	External 3.7 V Li-Po (520 mAh)	Internal 3.7 V Li-Po (120 mAh)
Dimensions (mm)	54 × 54 × 17	48.2 × 25.5 × 13.7
Weight	**45 g**	**24 g**

a) Boost Voltage Circuit

The boost circuit steps up the 3.7 V Li-Po battery to ~70 V using the ZXSC410 DC-DC controller [42], It employs an inductor (22 µH), a MOSFET (IRLML0100), a fast diode (BAS516), and a feedback divider (R1, R2) to ensure stable high-voltage output with low ripple. The regulation is based on the ZXSC410's 300 mV reference, as expressed in (1)

$$V_{out} = V_{FB}\left(1 + \frac{R1}{R2}\right) \quad (1)$$

Assuming R1 = 1 MΩ and V_{FB} = 300 mV, the required value of R2 to achieve 70 V output can be calculated using (2).

$$R2 = \left(\frac{V_{FB}R1}{V_{out} - V_{FB}}\right) = 4{,}304.16\Omega \quad (2)$$

By selecting R2 = 4.3 kΩ, the output voltage is regulated at approximately 70.07 V, which meets the system requirement. The final boost converter configuration and component placement are illustrated in Fig. 4.

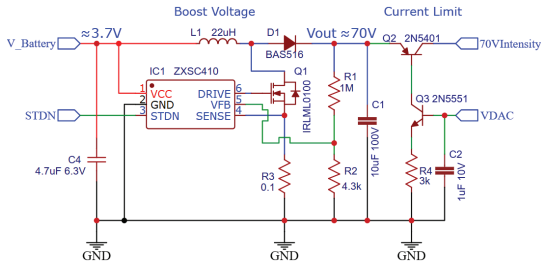

Fig. 4. Schematic of the stimulation node, showing the boost converter using ZXSC410 for 70 V output and the current limit circuit for VDAC-controlled stimulation

b) Current Limit Circuit

To ensure safe and programmable stimulation, the system incorporates a current limit circuit that regulates output current independently of voltage amplitude. A PNP transistor (Q2, 2N5401) [43] is controlled by an NPN transistor (Q3, 2N5551) [44], with the base of Q3 driven by an 8-bit DAC output from the ESP32. Adjusting the DAC voltage allows the microcontroller to modulate the base current of Q2, thereby setting the stimulation current, which is related to the base current via the transistor's current gain.

$$I_{OUT} = I_C(Q2) = I_B(Q2) \times h_{FE}(Q2) \quad (3)$$

Since Q3 directly sources this base current, $I_C(Q3) = I_B(Q2)$, and thus the DAC output controls Iout indirectly via Q3. Applying Ohm's law across R4 gives the collector current of Q3 as:

$$I_C(Q3) = \left(\frac{V_{dac} - V_{BE}(Q3)}{R_4}\right) \quad (4)$$

Combining (3) and (4), the required DAC voltage for a given output current can be expressed as:

$$V_{DAC} = \left(\frac{I_{OUT}}{h_{FE}(Q2)} \times R_4\right) + V_{BE}(Q3) \quad (5)$$

To support a maximum stimulation current of 40 mA with hFE (Q2) = 50, VBE = 0.7 V, and a conservative VDAC (max) = 3.0 V (leaving approximately 10% headroom from the ESP32's 3.3 V theoretical DAC limit), the value of R4 is selected as:

$$R_4 = \left(\frac{(V_{dac} - V_{BE}(Q3)) \times h_{FE}}{I_{OUT}(max)}\right) = \left(\frac{(3.0 - 0.7) \times 50}{0.04}\right) = 2{,}875\Omega \quad (6)$$

A standard value of R_4 = 2.7 kΩ or 3.0 kΩ may be selected depending on design tradeoffs. In this study, R_4 is fixed at 3.0 kΩ, ensuring compatibility with ESP32 DAC output range while maintaining operational margin for BJT gain variation, as implemented in the current-limiting circuit shown in Fig. 4. Using (5-6), the required DAC voltages for output currents of 20-40 mA (in 5 mA increments) are summarized in Table II. All DAC voltages fall within the ESP32's 8-bit DAC output range, validating the design. This indirect current control approach enables safe, energy-efficient, and scalable current delivery, ideal for wearable FES systems requiring compact and flexible stimulation control.

TABLE II
REQUIRED DAC VOLTAGES FOR PROGRAMMABLE OUTPUT CURRENT LEVELS

Level	Iout (mA)	Ib (Q2) (mA)	VDAC (V)
1	20	0.4	1.9
2	25	0.5	2.2
3	30	0.6	2.5
4	35	0.7	2.8
5	40	0.8	3.1

c) Pulse Control Circuit

The pulse control circuit is designed to generate biphasic symmetric stimulation waveforms, which are essential for FES to avoid tissue damage and ensure charge balance across the stimulation electrodes. To accomplish this, the system employs an H-Bridge topology that allows bidirectional current flow between two output terminals [41]. This design enables the generation of alternating positive and negative pulses in response to control signals from the ESP32 microcontroller. As shown in Fig. 5, the H-Bridge consists of four high-voltage transistor pairs: two PNP transistors (Q4 and Q5, 2N5401) [43] at the high side, and four NPN transistors (Q6-Q9, 2N5551) [44] at the low side. The 70 V stimulation voltage is applied at the top of the bridge, and the switching logic from the ESP32 determines which path current will take through the load (electrodes), thus controlling pulse polarity. The base drive for the high-side PNP transistors is provided through resistors R5 and R6, each set to 33 kΩ. These values are chosen to limit the base current to an appropriate level (~1-2 mA) while minimizing unnecessary power dissipation from the high-voltage source. For the low-side NPN transistors, resistors R7-R10 are set to 2.2 kΩ to ensure sufficient base current delivery from the ESP32's 3.3 V digital outputs, enabling fast transistor switching and clean pulse transitions.

This configuration supports stimulation pulses of 100-1000 µs at 10-100 Hz, with resistor values optimized for efficient switching and safe transistor operation. A high-speed diode (D2, BAS516) [45] is placed at the ground rail to suppress reverse transients and protect switching components during polarity changes. This enables precise, safe biphasic stimulation and forms a key link between the power stage and microcontroller logic in a compact design.

2) Sensor Node Design

The sensor node detects heel contact using a Force-Sensing Resistor (FSR) and wirelessly

triggers stimulation. It is built on the M5StickC Plus, an ESP32-based unit with BLE, TFT display, 120 mAh battery, and 4-pin connector for rapid prototyping [46]. Its compact size, onboard battery, and wireless capability make it ideal for wearable use. As shown in Fig. 3 (2), the sensor node consists of a heel pressure sensor and a circuit for signal processing and data transmission.

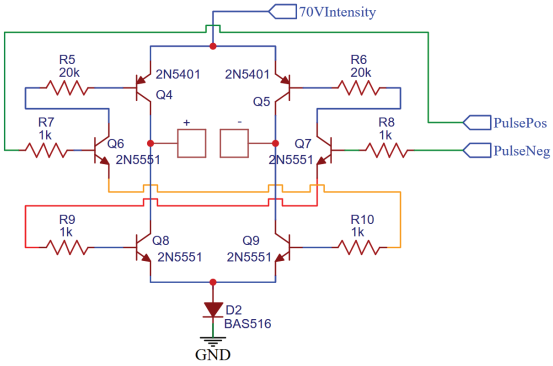

Fig. 5. H-bridge-based pulse control circuit for generating biphasic stimulation waveforms

a) Heel Pressure Sensor Design

To detect heel strike events, a custom force sensor with interdigitated electrodes on a 2-layer PCB detects heel strikes. The 0.8 mm pitch and trace width ensure uniform sensitivity across the 40 × 42 mm sensing area, with enhanced durability under foot pressure. To convert pressure into resistance, a conductive rubber strip (Neo Plastomer Co., Ltd., EP50) with a thickness of 0.6 mm and a nominal resistance range of 20-70 kΩ was placed on top of the electrode array. Under no load, the total resistance between sensor terminals ranged from 800-900 kΩ, and when pressure of approximately 10-15 kgf was applied (as estimated from manual pressing) [47], the resistance dropped to around 500-600 kΩ. This range effectively detects heel contact during walking. A custom sensor was developed due to limited commercial FSR options in the required size and form, with construction designed to endure repeated compression. The layout is shown in Fig. 6.

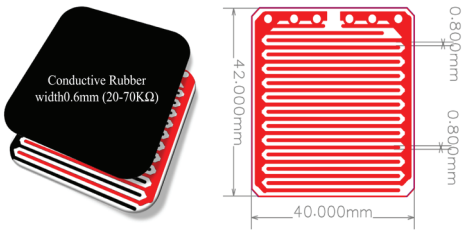

Fig. 6. Custom heel pressure sensor using conductive rubber and interdigitated PCB layout

b) Signal Conditioning and Data Transmission

To interface the sensor with the ESP32's analog-to-digital converter (12-bit ADC), a voltage divider using a 1 MΩ resistor converts the FSR's pressure into a 0.4-2.5 V signal. A 2.0 V threshold was set to detect heel contact, converting the signal to binary for BLE transmission and real-time stimulation control. The interface circuit is shown in Fig. 7.

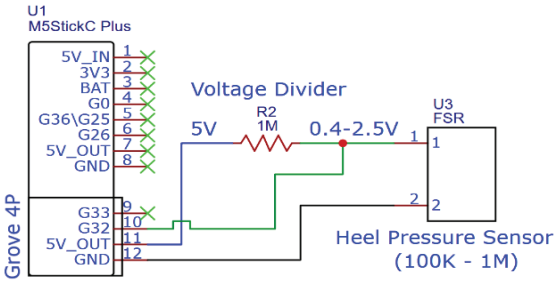

Fig. 7. Voltage divider interface circuit for sensor node using M5StickC Plus

B. *Firmware Design*

The firmware is split between the ESP32-based stimulation and sensor nodes. The stimulation node manages pulse generation, timing, and application communication, while the sensor node handles gait detection, threshold logic, and low-power BLE transmission. Details are provided in the following sections.

1) Firmware for Stimulation Node Design

The stimulation node firmware generates precise biphasic pulses and manages real-time tasks like BLE communication and user control. To achieve microsecond-level accuracy for 100-1000 µs pulses, a 50 µs hardware timer interrupt is used for waveform phase control. The core logic is handled in the pulse control task. Other functions, such as user interface control, BLE reception, cloud logging, and mode selection, run as separate Free RTOS tasks within the loop Task. This task separation ensures responsiveness while avoiding interference with pulse timing, as shown in Fig. 8.

Development used the Arduino Core for ESP32 (v3.1.1) with C/C++. Key libraries include the M5Stack library for hardware control, Free_Fonts library for display, Pub Sub Client library for MQTT, and BLE Device library for BLE server functionality. This implementation enables low-latency, reliable reception of gait triggers for synchronized stimulation. A task-based firmware architecture was adopted to ensure modularity and support future expansion. Two key tasks, pulse Control and signal Logic, handle stimulation timing, intensity, and phase control, ensuring accurate and reliable biphasic waveform generation during operation.

a) Pulse Control Task

The pulse control task handles real-time biphasic stimulation output using a hardware timer interrupt that triggers every 50 µs. The firmware

employs the pulseControl task for pulse control. The Interrupt Service Routine (ISR) is initialized during firmware startup in the setup function, as shown in Fig. 8, where the timer is configured to invoke pulseControl. The task receives timing parameters from the signal Logic task, including pulse duration and waveform phase lengths. During each interrupt, a counter is incremented and compared against these parameters to determine the output state, activating the positive, negative, or idle phase through H-bridge control signals. By isolating time-critical operations in this ISR and delegating logic handling to signal Logic, the system ensures accurate and consistent waveform generation, regardless of background processing load.

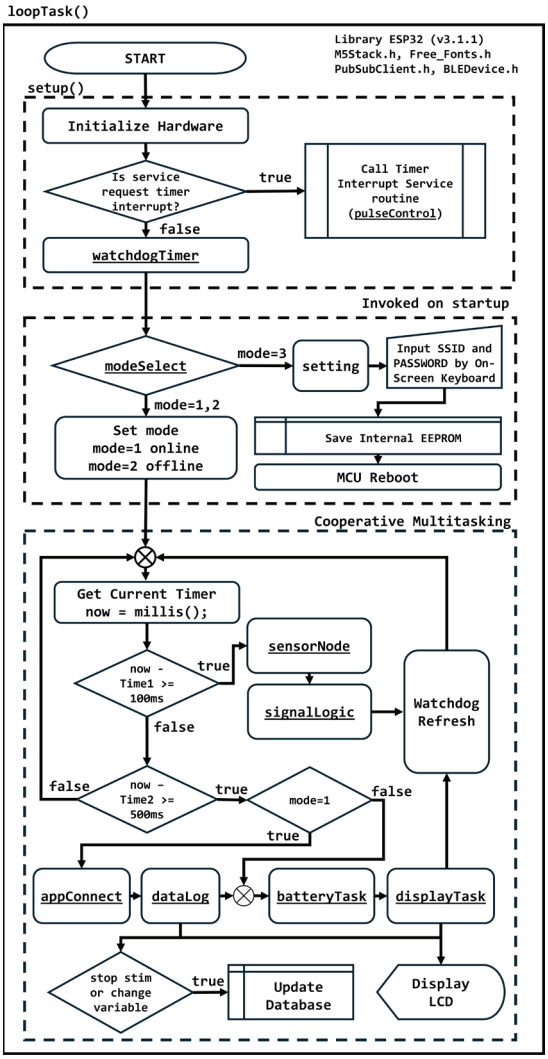

Fig. 8. Firmware execution flowchart of the stimulation node

b) Signal Control Task

The firmware employs the signalLogic task for signal control. This task is responsible for orchestrating the logical control of stimulation behavior, acting as the intermediary between user input, sensor trigger events, and the low-level pulse Control task responsible for waveform output. This task plays a key role in ensuring synchronized, programmable stimulation that adapts dynamically to both manual commands and sensor-based inputs. Within each control cycle, the task evaluates the current stimulation status. This status may originate from two independent sources: a user-defined input, such as pressing a physical button or toggling a mobile application control, or a real-time signal received from the sensor node via BLE, which corresponds to a detected heel strike.

When activated, the signalLogic task sets control flags and prepares waveform parameters. Based on the selected intensity level (1-5), it enables the boost converter via the STDN signal and adjusts the DAC output voltage according to a predefined current map (20-40 mA), regulated by the current limit circuit. For systems using an 8-bit DAC with a 3.3 V reference, the digital value sent to the DAC is calculated by scaling the desired voltage proportionally to the full range of 255 steps. For example, a DAC output of 1.65 V would correspond to roughly half of the maximum digital value.

Another key role of the signalLogic task is to compute timing parameters for each stimulation cycle, including ticks for the positive phase, negative phase, and idle period, based on user-defined pulse duration and frequency. These values, calculated using Equations (7)-(9), are essential for the pulseControl task to generate accurate waveforms.

$$N_{pulse} = \frac{t_{pulse}}{T_{ISR}} \tag{7}$$

$$N_{total} = \frac{1}{f \times T_{ISR}} \tag{8}$$

$$N_{idle} = N_{total} - 2N_{pulse} \tag{9}$$

Equations (7) to (9) define ISR tick counts for each pulse phase and idle period, based on user-defined pulse width and frequency. These values ensure correct waveform structure and are passed to the pulseControl task for real-time output. As shown in Fig. 8, signalLogic operates as a cooperative task at 100 ms intervals and handles key functions such as condition checks, DAC configuration, and tick calculation.

2) Firmware for Sensor Node Design

The sensor node firmware handles periodic heel pressure sensing and low-latency BLE transmission. It uses cooperative multitasking via a loopTask and non-blocking timing with the time function. At each interval, the 12-bit ADC reads sensor voltage, which is compared to a fixed threshold to detect heel strikes, encoded as binary output (1 = detected, 0 = not detected).

The system also monitors battery voltage and estimates its percentage, combining it with the pressure status into a 3-byte data frame. Operating as a BLE GATT server, the sensor node uses a custom

characteristic with notifications to asynchronously transmit data to the stimulation node, which acts as the BLE client.

The firmware was developed using Arduino Core for ESP32 (v3.1.1) in C++, leveraging the M5StickCPlus library for hardware control and the BLEDevice library for wireless communication. This setup enables efficient event detection, low power use, and real-time BLE synchronization with the stimulation node. The execution flow is shown in Fig. 9.

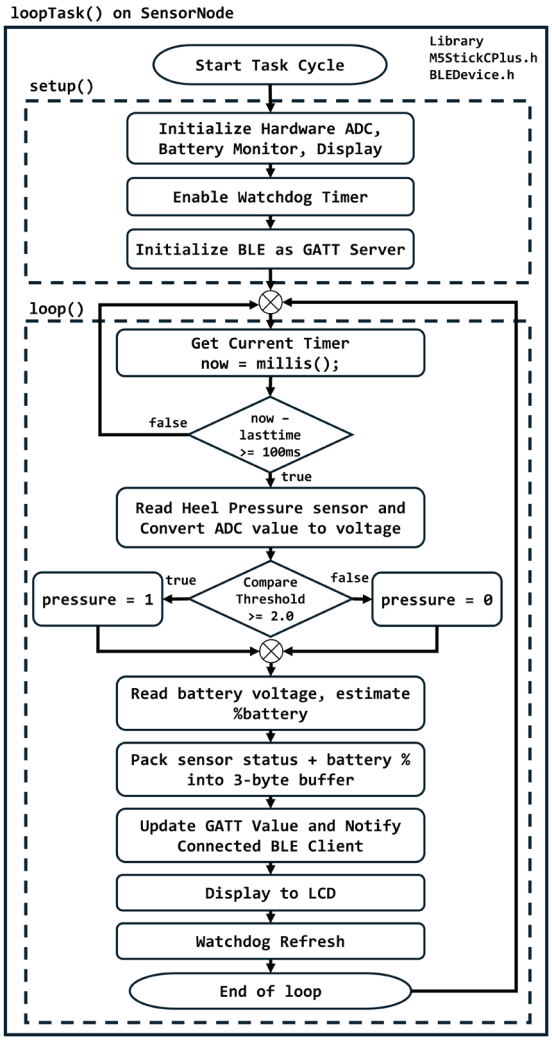

Fig. 9. Flowchart for Sensor Node Design

C. Mobile Health Application (m-Health) Design

The mobile health application (m-Health) developed in this study was designed based on the Technology Acceptance Model for m-Health (MoHTAM) [12] and the design themes proposed by Peng et al. [13], which emphasize perceived ease of use and perceived usefulness.

To improve user control, the application enables adjustment of stimulation parameters, including intensity, frequency, pulse width, and signal smoothness. It also offers pre-configured programs such as muscle relaxation and foot drop routines.

Effective data representation was also a key design objective. As such, the application provides a user-friendly interface that displays personal information, foot drop stimulation history, and the real-time status of stimulation and sensor nodes. The control flow and data representation design are summarized below.

Awareness & Literacy: Onboarding tutorials must be incorporated to familiarize users with the purpose, benefits, and operational procedures of the FES devices prior to engaging with the application.

Time & Effort: The interface is designed to minimize procedural steps and enhance user flow efficiency. Key features include shortcut pathways, One-Time-Password (OTP)-based registration, intuitive navigation structures, and automated stimulation program selection to reduce overall setup time.

Information Needs: Personalized content is delivered through both preset and manual configuration of stimulation parameters. The system also supports multiple-device scenarios for individual users.

Tracking and Feedback: Real-time visual feedback, delivered through charts and status indicators, enables users to effectively monitor stimulation activity and overall device performance.

Reminders: The application must provide users with the option to enable or disable the reminder system, as frequent notifications, whether auditory or visual, may cause annoyance or disrupt the user experience.

D. Communication Design

The system's communication architecture is structured into four layers: 1) the sensor node, which is responsible for collecting physiological data, 2) the stimulation node, which receives data from the sensor node via BLE, acts as the master controller for FES, and transmits data to 3) the cloud server, using the MQTT protocol over a Wi-Fi connection, and 4) the m-Health application, which serves as the user interface layer, supporting interaction and presenting data from the overall system as illustrated in Fig. 10.

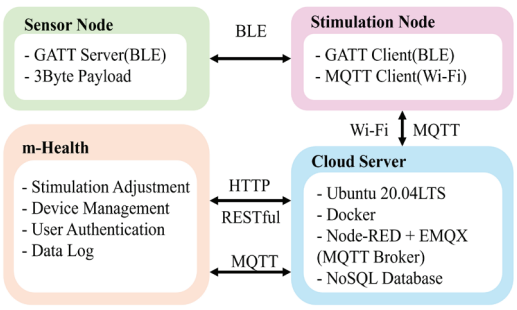

Fig. 10. System communication architecture

The data contained in the BLE payload, communicated between the GATT server and client, was designed to consist of three bytes: 1) the heel pressure state (pressed or unpressed), 2) a separator byte (0x2C), and 3) the battery level represented as a percentage. For example, a data value of 0x01, 0x2C, 0x64 indicates that heel pressure is detected and the battery level is 100%. This structure is optimized for rapid, energy-efficient transmission. The complete data format is described in TABLE III, while its The stimulation node also acts as an MQTT client, communicating with a cloud server hosted on Google Cloud Platform (GCP). The server runs Ubuntu 20.04 LTS with Docker, hosting containers for Node-RED and EMQX (used as an MQTT broker and monitor). Node-RED handles device logic and bridges MQTT messages to NoSQL database services for data logging and user interaction. The mobile health application connects directly to a NoSQL database using HTTP-based RESTful APIs. It provides a frontend interface for displaying system data, controlling stimulation modes, and visualizing user metrics. Communication between the mobile application and cloud backend occurs entirely through a NoSQL database, without requiring direct device-to-app connectivity. This communication design ensures modularity and reliability for distributed control and real-time synchronization.Experimental setup.

TABLE III
THE DESIGNED BLE DATA FORMAT

Byte Index	Description	Data Type	Value Range / Notes
0	Press/Release	uint8_t	0 = not pressed, 1 = pressed
1	Separate	uint8_t	ASCII ‘,’ (0x2C)
2	Battery percent	uint8_t	[0, 100]

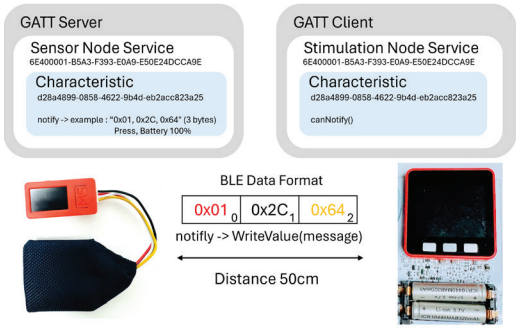

Fig. 11. BLE communication structure between stimulation and sensor nodes with 3-byte payload

To evaluate the performance of the proposed wireless FES system, a series of experimental tests was designed and conducted to assess the accuracy, latency, electrical characteristics, and power efficiency of both the stimulation and sensing modules. The system configuration and test parameters are summarized in TABLE IV. Each test aligns with specific system design domains, including hardware, firmware, communication, and mobile integration, ensuring comprehensive validation across all core components. The five primary experiments were structured as follows, with their respective linkage to system design components.

E. Boost Converter and Current Limit Test

The voltage boosting and current regulation functions of the stimulation node were evaluated in two stages. First, the boost converter (ZXSC410) was tested under open-circuit conditions to confirm voltage elevation from 3.7 V to ~70 V. Second, current regulation was assessed using an RC load (1.75 kΩ 100 nF) across five intensity levels, adjusted via DAC output (1.9–3.1 V). Voltage was monitored with a digital oscilloscope, and current was measured using a multimeter. Results validated the effective operation of both circuits under unloaded and loaded conditions.

F. Timing and Waveform Precision Test

Waveform timing was evaluated by measuring rise/fall times and pulse durations. Using a Rigol DS1022C, the stimulation signal showed sharp transitions under 5 µs and consistent 400 µs biphasic pulses at 50 Hz. Results confirmed accurate timing and waveform stability suitable for nerve stimulation.

G. Sensor Accuracy Test

The Analog-to-Digital Converter (ADC) of the sensor node (ESP32, 12-bit) was validated by comparing its digitized voltage output to a calibrated digital oscilloscope (Siglent SHS810). A heel pressure sensor was used to produce analog voltage values in the range of 0.4-2.5 V via a voltage divider. The sensor node read this voltage via its internal ADC and converted the result back to voltage, which was then compared against reference values from the digital multimeter. A total of 1,000 measurements were collected to compute the mean absolute error and maximum deviation.

TABLE IV
SUMMARY OF SPECIFICATIONS AND TEST PARAMETERS USED IN THE EXPERIMENTAL SETUP

Item	Specification
Stimulation Node Platform	M5Stack (ESP32-based microcontroller)
Sensor Node Platform	M5Stick C Plus (ESP32-based microcontroller)
Sensor	FSR (4x4.2cm pitch 0.8mm) Analog Output
Sampling Rate	10 Hz (100ms)
Wireless Communication Protocol	Bluetooth Low Energy (BLE)
Stimulator Circuit	H-Bridge Driver
Waveform	Symmetric Biphasic
Boost Converter	DC to DC Boost Convertor
Current limit	VDAC with BJT
Stimulation Frequency	50Hz
Stimulation Voltage	±70 V peak-to-peak
Pulse Duration	Positive 400us / Negative 400us
Inter-phase delay	100us
Measurement	Siglent SHS810 and Rigol DS1022C
Stimulation Node Battery	Li-po 3.7v 540mAh (2 × 270 mAh, parallel)
Sensor Node Battery	Li-po 3.7V 120mAh

H. Latency Test

A latency test was conducted to evaluate the communication delay between the sensor node (BLE GATT server) and stimulation node (GATT client) during real-time gait-triggered stimulation. The experiment took place in a 4 × 8 m concrete room with all external communication devices turned off. Both doors and windows were closed to minimize radio interference. The devices were positioned 50 cm apart in a line-of-sight configuration to simulate wearable placement. On the stimulation node, a timestamp was recorded immediately before executing the notifyCallback function. Upon receiving the 3-byte payload from the sensor node, a second timestamp was recorded. The latency (Δt) was calculated as the time difference between these two timestamps. This measurement was repeated 1,000 times, and the data were compiled for statistical analysis.

I. Operation Time and Power Consumption Test

Energy efficiency was evaluated by powering both nodes with internal batteries under continuous operation. New lithium-based cells with fewer than 50 charge cycles were used to minimize degradation effects [48]. The stimulation node, consisting of two parallel 10440 Li-ion cells (3.7 V, 270 mAh each, total 540 mAh), was configured to deliver 70 V biphasic pulses at 40 mA and 50 Hz into a 1.75 kΩ 100 nF load. The sensor node (M5StickC Plus with 3.7 V 120 mAh Li-Po) transmitted heel pressure data via BLE every 100 ms. Battery voltage was sampled every minute using the ESP32's internal ADC, and the system initiated automatic shutdown once voltage dropped below 3.1 V. This threshold was selected based on prior research indicating that operating lithium-ion cells below 3.0 V can accelerate degradation and compromise stability [49]. Continuous runtime was recorded until this cutoff was reached, providing a measure of the system's full-load endurance.

VI. RESULTS

The experimental results are presented in two parts. The first confirms hardware reliability through tests on latency, voltage boosting, current regulation, signal timing, and battery life. The second validates the mobile application's responsiveness, data synchronization, and control over stimulation modes.

A. Hardware System Result

The complete hardware system was successfully fabricated and assembled into a working prototype, comprising a stimulation node and a sensor node with supporting circuits. The final assembled devices are shown in Fig. 12 (a-b). Firmware for both nodes was successfully developed and deployed, Fig. 13 (a-b), enabling pulse generation, BLE communication, battery monitoring, and real-time task execution. In a foot drop use case, the stimulation node was positioned near the common peroneal nerve, and the sensor node under the heel, as illustrated in

Fig. 14 The stimulation device was positioned near the knee to align the electrode with the common peroneal nerve, which lies just below the knee on the lateral side of the leg. Together, Figs. 12-14 highlight the physical realization of the system, from hardware assembly to firmware deployment and electrode placement, demonstrating how the proposed prototype can be applied in a foot drop rehabilitation scenario. To avoid ethical concerns, no human subjects were involved; instead, the study focused on engineering design and functional validation through electrical and communication performance tests. Five key performance categories form the basis for technical evaluation, as outlined in Table V, and detailed in the following sections.

(a) (b)

Fig. 12. Overview of hardware components: (a) stimulation node, (b) sensor node

(a) (b)

Fig. 13. Firmware on hardware (a) firmware on stimulation node (b) firmware on sensor node

Fig. 14. The wireless FES attachment was affixed to the knee and heel.

Performance evaluation of the system was conducted across five core test categories, as summarized in Table V. The circuit was also verified under no-load conditions. A typical output waveform, measured using a Rigol DS1022C oscilloscope at a 400 µs pulse duration with a 100 µs inter-phase interval and 50 Hz frequency, is shown in Fig. 15, confirming that the designed hardware accurately produces symmetrical biphasic waveforms with sharp rise and fall transitions.

The latency test revealed a consistent response time with an average of 6.16 ms and a standard deviation of ±0.88 ms over 1,000 BLE transmission events. The complete latency distribution is presented in Fig. 16, confirming low-latency communication suitable for gait-synchronized stimulation.

TABLE V
SUMMARY OF EXPERIMENTAL RESULTS

Test Item	Description	Result Summary
Latency	Response delay measured from the BLE transmission	1000 samples collected. Average Latency: 6.16 ms SD: ±0.88 ms Max: 8.34 ms Min: 4.91 ms
ADC Module Accuracy	Accuracy of the 12-bit ADC in the sensor node	Vout range: 0.4-2.5 V MAE: 1.2 Max Error: 4 Error < 1.1% Samples: 1000
Boost Converter and Full Load Output Measure-ment	Verification of the voltage boosting capability and output current regulation across programmable intensity levels	Open Circuit Test: - Peak output voltage: 73.6 V - Ripple voltage: ±3.45 V Intensity Test: - L1: 19.35 mA, Err: 3.26% - L2: 25.75 mA, Err: 2.99% - L3: 30.25 mA, Err: 0.85% - L4: 33.42 mA, Err: 4.52% - L5: 39.31 mA, Err: 1.74%
Rise/Fall Time and Pulse Duration	Transition speed and Timing consistency of biphasic 400 µs	Pulse Duration(avg): 400.3 µs Measured rise/fall time: 2.1 µs
Operation Time (Stimula-tion node)	Battery life of the stimulation node under full load	Full system operation at 70 V 40 mA load BLE read every 100 ms Duration: ~4 hours 4m
Operation Time (Sen-sor node)	Battery life of the sensor node during full load	BLE active, convert sensor data every 100 ms Duration: ~1 hour 6m

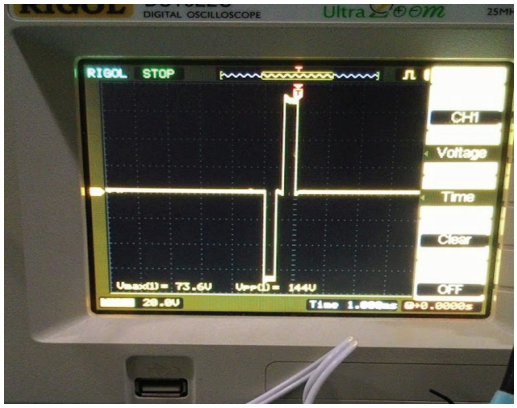

Fig. 15. Symmetrical biphasic waveform measured at 400 µs pulse duration

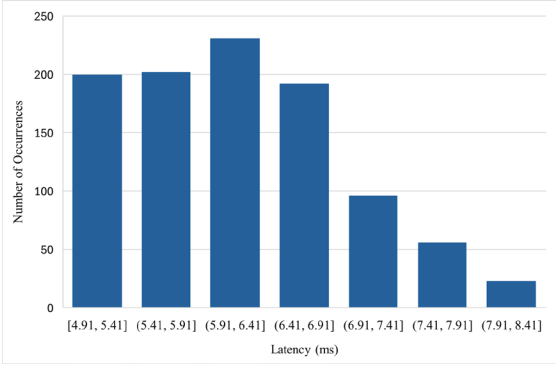

Fig. 16. Distribution of measured BLE latency over 1,000 trans-missions

In terms of power management, battery endurance was assessed under continuous full-load conditions over five independent trials. The stimulation node, operating at 70 V and 40 mA, maintained functionality for approximately 4 hours, while the sensor node, transmitting BLE data at 100 ms intervals, operated for over 1 hour. As shown in the voltage discharge curves in Fig. 17, all trials terminated just above 3.1 V, confirming the consistent performance of the power system and proper functioning of the voltage protection mechanism.

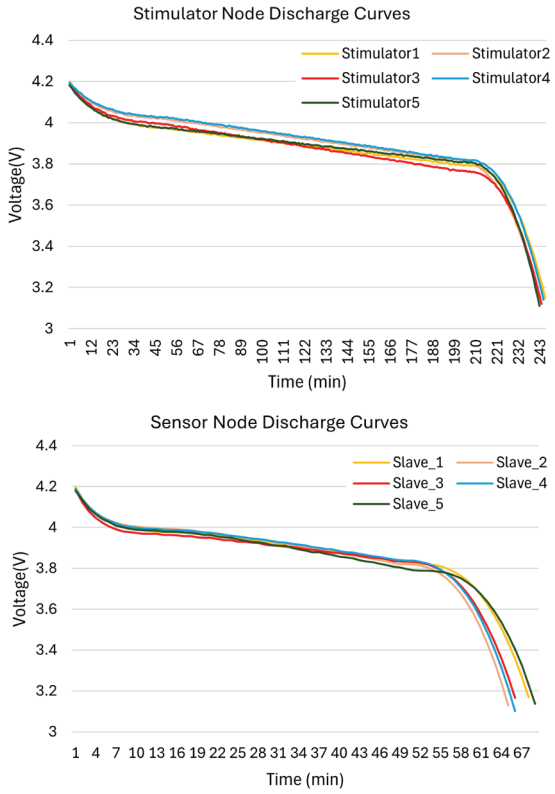

Fig. 17. Battery voltage profile of the stimulation node and sensor node

These results collectively validate the system's functionality, timing precision, power delivery, and wireless communication reliability, supporting its use as a robust, wearable rehabilitation device and a versatile research platform for FES-based neuromuscular interventions.

B. Mobile Health Application Result

The design implications outlined in the previous section were implemented using React Native for the development of the m-Health application in this study. Upon installation, users are directed to a series of welcome screens as illustrated in Fig. 18 (a-c), which introduce the system's objectives and provide guidance on how to use the electrical stimulation features. Users may choose to proceed by tapping the "Continue" button to access more information, or "Skip" to begin using the application immediately. Subsequently, users who have previously registered are automatically signed in. New users are required to register using their email or phone number and a One-Time Password (OTP) sent via SMS, as illustrated in Fig. 19 (a-b).

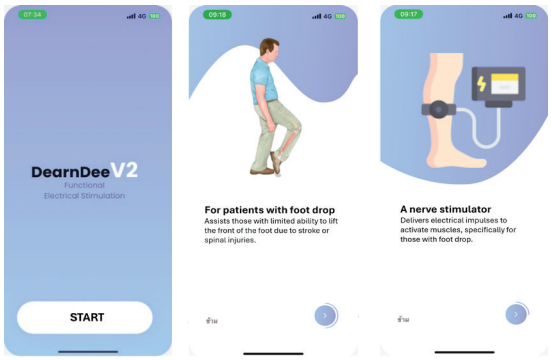

(a) (b) (c)

Fig. 18. (a) Initial welcome screen, (b) example of the system objective screen, and (c) instructional screen for wearing the device

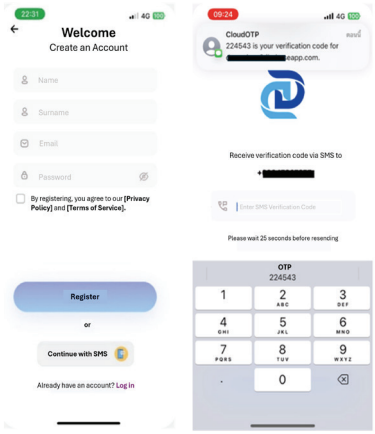

(a) (b)

Fig. 19. (a) Registration screen via email, and (b) registration screen using phone number and One-Time Password (OTP)

Upon entering the application, users are presented with a set of stimulation device management interfaces, as illustrated in Fig. 20 (a) and Fig. 20 (b), which show the device status. These interfaces include screens for adding, deleting, updating, and viewing device information, as well as a usage history screen for monitoring device activity.

After completing the setup tutorial, users are instructed to wear the stimulation node around the knee and place the sensor node near the ankle. They then select the target device from the list shown in Fig. 19 (a). Upon selection, the control interface illustrated in Fig. 21 is displayed, consolidating all available functionalities for operating the stimulation node.

The top section of the interface displays battery levels and communication status for both the stimulation and sensor nodes. Directly below, toggle buttons

allow users to power both devices on and off at the same time. Electrical parameters such as program type, intensity, frequency, signal smoothness, and pulse width can be configured through the interface. In relaxation mode, all parameters except intensity are automatically set based on predefined values stored in the firmware. Users can still manually adjust the intensity level to suit personal comfort and preferences.

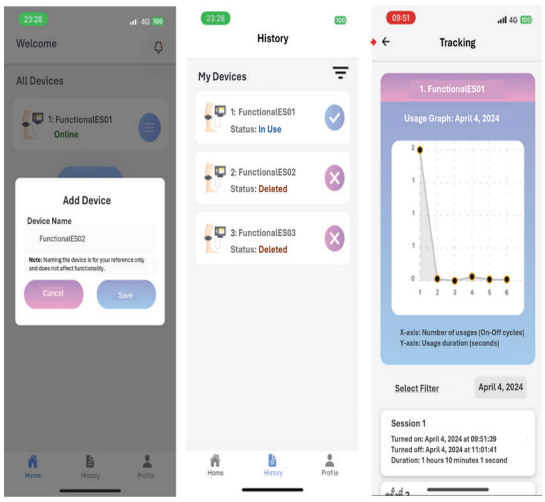

(a) (b) (c)

Fig. 20. (a) Screen for adding stimulation devices, (b) screen for deleting and viewing stimulation devices

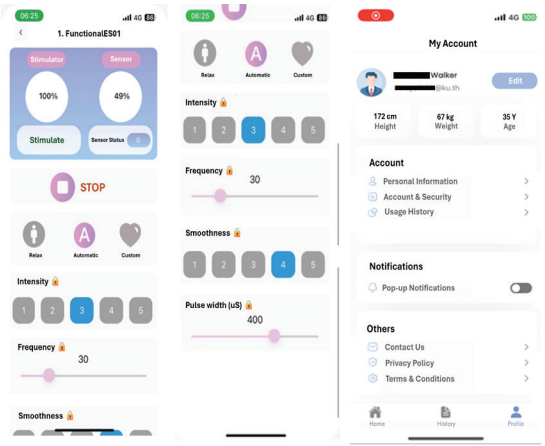

(a) (b) (c)

Fig. 21. (a) Upper section of the stimulation control interface, (b) lower section of the interface

In preset mode, the stimulation node adjusts electrical parameters based on firmware-derived values tailored to the user's physiological profile, activating only upon receiving a sensor signal. In manual mode, user-defined parameters are applied, with activation also triggered by the sensor node.

Lastly, users are provided with a configuration screen that allows them to update their personal information and enable or disable the reminder system through notification messages.

VII. Discussion

This study presents the design and development of a wireless functional electrical stimulation system for foot drop rehabilitation, integrating a stimulation node, a sensor node, a cloud-based data layer, and a mobile health application. The system achieved reliable performance in key areas, including biphasic pulse generation, low-latency BLE communication, real-time parameter control, and mobile feedback.

Experimental validation demonstrated accurate waveform generation (400.3 µs pulse width, 2.1 µs rise/fall time) and stable current delivery across different loads. BLE latency averaged 6.16 ms, meeting the <50 ms threshold for real-time gait stimulation [50]. Power tests showed the stimulation node operated for ~4 hours, while the sensor node lasted ~1 hour.

The wireless architecture posed engineering challenges, addressed by using interrupt-driven firmware for microsecond-level control and cooperative multitasking for reliable BLE communication and UI handling within ESP32 constraints.

The functionality and workflow of the mobile application developed in this study cover rehabilitation activities, providing a module for parameter adjustment and real-time feedback from the installed sensors.

Despite its strengths, the system has limitations. Clinical effectiveness is unverified due to the absence of human testing. The use of a single heel pressure sensor may not fully capture complex gait patterns, and the sensor node's limited battery life and lack of closed-loop current control restrict long-term use and precise stimulation.

Compared to prior FES systems, this design offers advantages in modularity, portability, and integration. While previous works often lacked mobile interfaces or relied on fixed setups, the proposed system combines open-source hardware, real-time BLE, and mobile-cloud support, making it well-suited for home-based rehabilitation. In contrast to a previously deployed wired FES system [11], the present design enhances portability, user control, and home-based applicability through wireless communication and mobile application integration. In comparison with commercial devices such as the Bioness L300 Go [31] or WalkAide [32], which offer advanced features but at high cost, the proposed system provides a more accessible solution. Similarly, compared with recent academic prototypes, which often sacrifice mobile integration or connectivity to maintain low cost, this work achieves a balanced approach that bridges the gap between expensive commercial systems and limited academic designs.

VIII. Conclusion and Future Work

This work demonstrates the feasibility of a low-cost, wireless FES system that integrates real-time stimulation control, BLE-based sensor input, and mobile-cloud connectivity. The system performed reliably across electrical, communication, and software layers, supporting its potential use for home-based rehabilitation in foot drop patients.

Future development will focus on enhancing sensor flexibility by integrating IMU or sensor-less gait analysis, improving battery life through optimized power management, and implementing closed-loop current control to ensure stimulation accuracy. Clinical testing with human participants is also essential to evaluate usability, therapeutic outcomes, and long-term effectiveness.

Funding: This research received no external funding.

Data Availability Statement: The original contributions presented in the study are included in the article; further inquiries can be directed to the corresponding author on reasonable request.

Acknowledgments: The authors would like to thank the Faculty of Engineering at Sriracha, Kasetsart University, for providing the facilities for experimentation.

Conflicts of Interest: The authors declare no conflicts of interest.

References

[1] V. L. Feigin et al., "World Stroke Organization (WSO): Global stroke fact sheet 2022," *Int. J. Stroke*, vol. 17, no. 1, pp. 18-29, Jan. 2022, https://doi.org/10.1177/17474930211065917

[2] S. L. Nori and M. F. Stretanski, *Foot Drop.* Treasure Island, FL, USA: StatPearls Publ., 2025.

[3] D. Totah, M. Menon, C. Jones-Hershinow, K. Barton, and D. H. Gates, "The impact of ankle-foot orthosis stiffness on gait: A systematic literature review," *Gait Posture*, vol. 69, pp. 101-111, Jan. 2019.

[4] P. Chayaratanasin, S. Vongpipatana, and W. Chira-Adisai, "Comparison of gait pattern during walking with and without functional electrical stimulation 'Dearndee™' in stroke patients with foot drop: A pilot study," *ASEAN J. Rehabil. Med*., vol. 25, no. 2, pp. 65-72, Aug. 2015.

[5] S. Kumnoonsup, M. Buntragulpoontawee, and A. Kovindha, "Effectiveness of functional electrical stimulator (FES-Dearndee™) on physiological cost index in subacute stroke patients with foot drop: A pilot study," *ASEAN J. Rehabil. Med.*, vol. 25, no. 3, pp. 95-102, Dec. 2015.

[6] A. Behboodi, N. Zahradka, H. Wright, J. Alesi, and S. C. Lee, "Real-time detection of seven phases of gait in children with cerebral palsy using two gyroscopes," *Sensors*, vol. 19, no. 11, p. 2517, Jun. 2019.

[7] Y. R. Mao et al., "Spatiotemporal, kinematic and kinetic assessment of the effects of a foot drop stimulator for home-based rehabilitation of patients with chronic stroke: A randomized clinical trial," *J. Neuroeng. Rehabil.*, vol. 19, no. 1, p. 56, Dec. 2022, https://doi.org/10.1186/s12984-022-01036-0/

[8] D. B. Popović, "Foot drop stimulator," in *Handbook of Biochips*, M. Sawan, Ed. New York, NY, USA: Springer, 2022, pp. 1241-1255.

[9] F. Alnajjar, R. Zaier, S. Khalid, and M. Gochoo, "Trends and technologies in rehabilitation of foot drop: A systematic review," *Expert Rev. Med. Devices*, vol. 18, no. 1, pp. 31-46, Jan. 2021, https://doi.org/10.1080/17434440.2021.1857729

[10] A. E. Carolus, M. Becker, J. Cuny, R. Smektala, K. Schmieder, and C. Brenke, "The interdisciplinary management of foot drop," *Dtsch. Arztebl. Int.*, vol. 116, no. 20, pp. 347-354, 2019.

[11] J. Jitprasutwit, R. Chaiwattanatham, and Z. Lertmanorat, "Development and distribution of functional electrical stimulator for foot drop for Thais," in *Proc. 8th Biomed. Eng. Int. Conf. (BMEiCON*), 2015, pp. 1-4.

[12] A. H. H. Mohamed, H. Tawfik, D. Al-Jumeily, and L. Norton, "MoHTAM: A technology acceptance model for mobile health applications," in *Proc. Developments E-Syst. Eng.*, 2011, pp. 13-18.

[13] W. Peng, S. Kanthawala, S. Yuan, and S. A. Hussain, "A qualitative study of user perceptions of mobile health apps," *BMC Public Health*, vol. 16, no. 1, p. 1158, Dec. 2016, https://doi.org/10.1186/s12889-016-3808-0

[14] A. Kralj and T. Bajd, *Functional Electrical Stimulation: Standing and Walking after Spinal Cord Injury*. Abingdon, U.K: Routledge, 2022, p. 208.

[15] J. S. Park, S. H. Lee, W. G. Yoo, and M. Y. Chang, "Immediate effect of a wearable foot drop stimulator to prevent foot drop on the gait ability of patients with hemiplegia after stroke," *Assist. Technol.*, vol. 33, no. 6, pp. 313-317, Nov. 2021, https://doi.org/10.1080/10400435.2019.1634658

[16] G. Hsu, F. Farahani, and L. C. Parra, "Cutaneous sensation of electrical stimulation waveforms," *Brain Stimul.*, vol. 14, no. 3, pp. 693-702, 2021.

[17] C. Marquez-Chin and M. R. Popovic, "Functional electrical stimulation therapy for restoration of motor function after spinal cord injury and stroke: A review," *Biomed. Eng. Online*, vol. 19, no. 1, p. 34, Dec. 2020, https://doi.org/10.1186/s12938-020-00773-4

[18] A. S. Gorgey, H. J. Poarch, D. D. Dolbow, T. Castillo, and D. R. Gater, "Effect of adjusting pulse durations of functional electrical stimulation cycling on energy expenditure and fatigue after spinal cord injury," *J. Rehabil. Res. Dev.*, vol. 51, no. 9, pp. 1455-1468, Aug. 2014.

[19] Espressif Systems, "ESP32 Bluetooth Architecture," *Espressif*, 2025. [Online]. Available: https://www.espressif.com/sites/default/files/documentation/esp32_bluetooth_architecture_en.pdf. [Accessed: May 19, 2025].

[20] D. Hercog, T. Lerher, M. Truntič, and O. Težak, "Design and implementation of ESP32-based IoT devices," *Sensors*, vol. 23, no. 15, p. 6739, Jul. 2023.

[21] S. D. Bhattacharya and M. Manjunatha, "Functional electrical stimulation on improving foot drop gait in poststroke rehabilitation: A review of its technology and clinical efficacy," *Crit. Rev. Biomed. Eng.*, vol. 41, no. 2, Jan. 2013.

[22] P. L. Melo, M. T. Silva, J. M. Martins, and D. J. Newman, "Technical developments of functional electrical stimulation to correct drop foot: sensing, actuation and control strategies," *Clin Biomech*, vol. 30, no. 2, pp. 101-113, 2015.

[23] T. Watanabe, S. Endo, and R. Morita, "Development of a prototype of portable FES rehabilitation system for relearning of gait for hemiplegic subjects," *Healthc. Technol. Lett.*, vol. 3, no. 4, pp. 284-289, Dec. 2016, https://doi.org/10.1049/htl.2016.0045

[24] P. Aqueveque et al., "A novel capacitive step sensor to trigger stimulation on functional electrical stimulators devices for drop foot," *IEEE Trans. Neural Syst. Rehabil. Eng.*, vol. 28, no. 12, pp. 3083-3088, Jan. 2020.

[25] G. York and S. Chakrabarty, "A survey on foot drop and functional electrical stimulation," *Int. J. Intell. Robot. Appl.*, vol. 3, no. 1, pp. 4-10, Mar. 2019, https://doi.org/10.1007/s41315-019-00088-1

[26] K. Kipli, M. N. Ulia, L. Roslan, A. Jamali, and N. Soin, "Functional Electrical Stimulation (FES) study for foot drop rehabilitation using Arduino Nano Atmega328p," in *Proc. 4th Int. Conf. Innov. Biomed. Eng. Life Sci. (IFMBE P)*, vol. 107, 2024, pp. 242-249, https://doi.org/10.1007/978-3-031-56438-3_24
[27] T. F. De Almeida, L. H. B. Borges, and A. F. O. de A. Dantas, "Development of an IoT electrostimulator with closed-loop control," *Sensors*, vol. 22, no. 9, p. 3551, 2022.
[28] N. Gangadharan, S. Balasubramanian, G. Tharion, J. John, T. Senthilvelkumar, and S. Devasahayam, "An intelligent system for automatic footdrop correction in stroke patients using FES: A pilot study," *Int. J. Sci. Eng. Res.*, vol. 10, no. 4, pp. 1102-1110, Apr. 2019.
[29] O. A. Chiriac, F. C. Adochiei, N.-I. Trocan, and M. I. Nistor, "Design and implementation of a cost-effective, functional electrical stimulation device for foot drop rehabilitation," *Rev. Roum. Sci. Tech. Electrotech. Energ.*, vol. 70, no. 1, pp. 151-156, 2025.
[30] Y. Cao et al., "Development of a wearable ultrasound–FES integrated rehabilitation and motor-functional reconstruction system for post-stroke patients," *Biomed. Signal Process. Control*, vol. 100, p. 106846, Feb. 2025.
[31] Bioness, "L300 Go System for foot drop," *BionessMedical*, 2025. [Online]. Available: https://bionessmedical.com/l300/ [Accessed: Jan. 19, 2025].
[32] BioMetrics Prosthetic and Orthotic CT, "WalkAide® System for foot drop," *BioMetrics*, 2025. [Online]. Available: https://biometricsct.com/custom-orthopedic-care/walkaide/ [Accessed: May 19, 2025].
[33] XFT, "Foot Drop System (XFT-2001D)," *China*, 2025. [Online]. Available: https://www.xft-china.com/foot-drop-system [Accessed: Jan. 19, 2025].
[34] X. I. E. Chunhu and C. Liu, "Functional electrical stimulation therapeutic apparatus for foot drop," China, CN Patent 113965021 B, Aug. 9, 2022.
[35] T. Keller, N. Malesevic, and G. Bijelic, "System and method for functional electrical stimulation," U.S. Patent 10,772,544, Sep. 15, 2020.
[36] M. T. Anton, H. M. Greenberger, E. Andreopoulos, and R. L. Pande, "Evaluation of a commercial mobile health app for depression and anxiety (Able to Digital+): Retrospective cohort study," *JMIR Form. Res*., vol. 5, no. 9, p. e27570, Sep. 2021.
[37] S. Rianmora and S. Seng, "Keep It Cool' smart bag by Internet of Things (IoT) for better living with alternative design," *Int. Sci. J. Eng. Technol. (ISJET)*, vol. 5, no. 2, pp. 38-54, Dec. 2021.
[38] K. Wongwut, C. Chaisermvong, and D. Angamnuaysiri, "The development of smart farming system for sea lettuce cultured process," *Int. Sci. J. Eng. Technol. (ISJET)*, vol. 8, no. 2, pp. 47-53, Dec. 2024.
[39] M5Stack, "M5Stack Basic Development Kit,' M5Stack documentation." *M5Stack*, 2025. [Online]. Available: https://docs.m5stack.com/en/core/basic [Accessed: May 19, 2025].
[40] ON Semiconductor, "2N5401: PNP silicon transistor, datasheet, Rev. 2.1," *Onsemi*, 2025. [Online]. Available: https://www.onsemi.com/pdf/datasheet/2n5401-d.pdf [Accessed: Feb. 19, 2025].
[41] H. Nisar, A. R. Malik, M. Asawal, and H. M. Cheema, "An electrical stimulation based therapeutic wearable for pressure ulcer prevention," in *Proc. IEEE EMBS Conf. Biomed. Eng. Sci. (IECBES)*, 2016, pp. 411-414.
[42] Diodes Inc., "ZXSC410: Voltage mode boost controller." *Diodes*, 2025. [Online]. Available: https://www.diodes.com/part/view/ZXSC410 [Accessed: Feb. 19, 2025].
[43] ON Semiconductor, "2N5401: PNP silicon transistor, datasheet, Rev. 2.1," *On Semiconductor*, 2025. [Online]. Available: https://www.onsemi.com/pdf/datasheet/2n5401-d.pdf [Accessed: Feb. 19, 2025].
[44] ON Semiconductor, "2N5551: NPN silicon transistor, datasheet, Rev. 6," *On Semiconductor*, 2025. [Online]. Available: https://www.onsemi.com/download/data-sheet/pdf/2n5551t-d.pdf [Accessed: May 19, 2025].
[45] Nexperia, "BAS516: High-speed switching diode, datasheet," *Nexperia*, 2025. [Online]. Available: https://www.nexperia.com/product/BAS516 [Accessed: May 19, 2025].
[46] M5Stack, "M5StickC Plus Development Kit,' M5Stack documentation," *M5Stack*, 2025. [Online]. Available: https://docs.m5stack.com/en/core/m5stickc_plus [Accessed: May 19, 2025].
[47] S. Aali, F. Rezazadeh, G. Badicu, and W. R. Grosz, "Effect of heel-first strike gait on knee and ankle mechanics," *Medicina*, vol. 57, no. 7, p. 657, Jun. 2021.
[48] P. Keil and A. Jossen, "Charging protocols for lithium-ion batteries and their impact on cycle life—an experimental study with different 18650 high-power cells," *J. Energy Storage*, vol. 6, pp. 125-141, May. 2016.
[49] G. J. Páez Fajardo et al., "Synergistic degradation mechanism in single crystal Ni-rich NMC//graphite cells," *ACS Energy Lett*., vol. 8, no. 12, pp. 5025-5031, Dec. 2023, https://doi.org/10.1021/acsenergylett.3c01596

Jirawat Jitprasutwit is a lecturer in the Department of Computer Engineering, Faculty of Engineering at Sriracha, Kasetsart University Sriracha Campus,Thailand. He received an M. Eng. in Electrical Engineering from Mahidol UniversityThailand. His research , interests include biomedical engineering, Artificial Intelligence, Internet of Things, embedded systems, and smart intelligent systems.

Anan Banharnsakun is an Associate Professor in the department of computer engineering, Faculty of Engineering at Sriracha, Kasetsart University, Campus, Thailand. He received a Ph.D. degree in Electrical and Computer engineering from King Mongkut's University of Technology Thonburi (KMUTT), Thailand. His research interests include biologically inspired computational intelligence, robust optimization, pattern recognition, and high-performance computing.

Kathawach Satianpakiranakorn is a lecturer in the Department of Computer Engineering, Faculty of Engineering at Sriracha, Kasetsart University, Sriracha Campus, Thailand. He received M.Eng. in Computer Applied Technology from Harbin Engineering University, P.R. Harbin, China. His research field includes Artificial Intelligence, computer vision, and digital image processing.

Kanjana Eiamsaard is an Assistant Professor in the department of computer engineering, Faculty of Engineering at Sriracha, Kasetsart University Sriracha Campus, Thailand. She received an M.S. in Software Engineering from Chulalongkorn University, Thailand. Her research interests include Artificial Intelligence, machine learning, and software engineering.

Enhancing Vehicle Routing with Time Windows Solutions via K-means Clustering: A Comparative Study of Elbow and Truck Utilization Methods

Kanokporn Boonjubut[1], Prat Boonsam[2], and Sirichai Yodwangjai[3*]
[1,2]Department of Engineering Management, Faculty of Industrial Technology,
Nakhon Ratchasima Rajabhat University, Nakhon Ratchasima, Thailand
[3]Department of Industrial Engineering Technology, College of Industrial Technology,
King Mongkut's University North Bangkok, Bangkok, Thailand
E-mail: kanokporn.b@nrru.ac.th, prat.b@nrru.ac.th, sirichai.y@cit.kmutnb.ac.th*

Received: May 10, 2025 / Revised: September 29, 2025 / Accepted: October 2, 2025

***Abstract*—The vehicle routing problem with time windows is important in optimizing logistics distribution. For VRPTW optimization, a strategy is used to classify and optimize routes using artificial intelligence methods. Therefore, an improved two-phase algorithm is required to find a solution. Namely, a customer group can be divided into several regions using the K-means algorithm in the first phase, and each region can be decomposed into smaller subgroups according to certain constraints. In the second phase, local search from OR-tools solves the routing problem. In this experiment, two different methods of determining the number of clusters, namely, the elbow method and the truck utilization method, are compared by experimenting with a total of 26 standard instances. The results show that the truck utilization ratio outperforms the elbow method for the K-means algorithm in terms of overall results. The results from this experiment can be highly beneficial for routing, particularly when handling huge amounts of data that need to be subdivided ahead.**

***Index Terms*—Clustering, K-means, Routing Problem, Time Windows**

I. Introduction

Nowadays, people are using the internet to purchase items more and more because of these factors. The primary issue for the businesses in this situation is to offer more demanding clients a more effective distribution service. A number of large online merchants have begun searching for more creative and efficient ways to expedite last-mile and same-day delivery.

The rapid economic growth at both national and global levels has intensified business competition. To remain competitive, companies must enhance their logistical and transportation systems, as these are crucial components of efficient business operations. In supply chain management, one of the fundamental challenges is optimizing vehicle selection and routing to minimize shipping costs. This problem aligns with the Vehicle Routing Problem (VRP), which addresses transportation system issues such as route optimization, vehicle capacity management, transportation time windows, and accommodating diverse customer requirements [1].

The emergence of the Internet of Things (IoT) and big data analytics has significantly improved logistics operations. These technologies enable precise and effective monitoring of transportation processes through cloud computing, enhancing logistics efficiency and reducing operational costs [2]. However, many companies still rely on outdated logistics management systems that require significant manual effort. As businesses handle increasing order volumes, the need for a robust and efficient decision-support system for logistics distribution becomes critical.

A widely adopted approach in solving vehicle routing problems is the Cluster-First Route-Second (CFRS) strategy. This method consists of two main stages: first, decomposing shipping points into smaller clusters, followed by optimizing routes within each cluster [3]. Clustering plays a vital role in managing transportation route problems, as it helps break down complex logistics challenges into manageable subgroups.

Several clustering techniques have been applied in logistics, with K-means being one of the most prominent methods. K-means effectively clusters groups of delivery points based on proximity and shared transportation constraints, forming distinct clusters before applying route optimization algorithms [4]. Transportation route optimization can be approached by grouping delivery points into clusters based on factors such as distance or time windows, allowing each cluster to be assigned a specific vehicle for efficient deliveries [5].

The CFRS strategy is particularly useful in solving the Vehicle Routing Problem with Time Windows (VRPTW), where deliveries must adhere to strict time constraints. By first clustering delivery points and then optimizing routes within each cluster, computational time is reduced, and solution quality is improved, particularly in large-scale logistics operations [6]. Therefore, clustering should be effectively executed to maximize its impact on logistics efficiency and overall supply chain performance.

While the Cluster-First, Route-Second (CFRS) strategy has demonstrated effectiveness in addressing the Vehicle Routing Problem with Time Windows (VRPTW), a significant research gap persists in the optimal determination of the number of clusters. Existing literature predominantly employs the elbow method to determine the appropriate number of clusters in K-means clustering. However, this technique does not sufficiently account for operational constraints such as vehicle capacity utilization, which is critical for practical logistics applications.

The research question explored in this study is: How does the elbow method for cluster determination compare with optimization based on truck utilization ratio in terms of overall logistics efficiency and cost-effectiveness? This comparison is particularly significant because while the elbow method aims to minimize within-cluster variance as a statistical measure of clustering quality, it may not align with the practical objective of maximizing vehicle capacity utilization, which directly impacts operational expenses and resource efficiency. Current literature predominantly employs the elbow method for determining optimal cluster numbers in vehicle routing problems with time windows without a systematic evaluation of its operational effectiveness. This creates a research gap where statistically optimal clustering is assumed to translate into operationally efficient routing without empirical validation.

This study addresses this gap by making several key contributions to logistics optimization. First, this work develops the first systematic comparison framework between statistical clustering validation and operational optimization approaches for vehicle routing problems with time windows. Second, it provides empirical validation demonstrating the conditions under which each clustering approach delivers superior performance in terms of cost reduction and resource utilization. These contributions advance both theoretical understanding of clustering effectiveness in transportation systems and provide practical guidance for logistics optimization in real-world applications.

II. Literature Review

The Vehicle Routing Problem (VRP) is a critical issue frequently addressed by managers in logistics and transportation. A VRP involves the distribution of goods from an origin as a single depot or multiple depots to multiple destinations [7]. Solving VRPs provides significant benefits to businesses, including optimized routes and travel times, reduced vehicle requirements, and improved vehicle utilization. These efficiencies lead to lower overall logistics costs and increased profitability for organizations [7].

An extension of the VRP is the Vehicle Routing Problem with Time Windows (VRPTW), which not only focuses on minimizing route costs but also incorporates time constraints to ensure that customers are serviced within predefined time windows, bounded by the earliest and latest permissible times [8], [9].

In the VRPTW framework, the optimization model must account for specific time-based service requirements designated by each customer within the distribution network. These temporal constraints are formally defined through a dual-parameter system: (e_i) represents the earliest permissible service initiation time, while (l_i) denotes the latest allowable service completion time for each customer. This temporal framework introduces an additional dimension of complexity to the traditional spatial routing optimization problem.

A notable characteristic of VRPTW implementations is the concept of soft time windows, which introduces operational flexibility while maintaining service quality standards. Under this constraint structure, delivery vehicles are permitted to arrive at customer locations before the designated earliest start time (s_i). However, in such instances, service commencement must be delayed until the customer's specified time window officially begins. This waiting time, while not subject to direct penalties, must be incorporated into the overall route optimization calculations as it impacts operational efficiency and resource utilization. Fig. 1 shows an example of a VRPTW problem where each customer has their specific service time window.

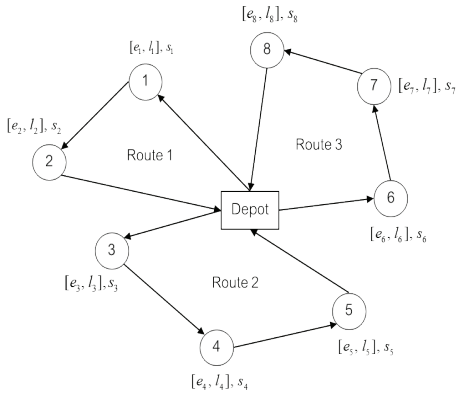

Fig. 1. Eight customers and one depot network

This study employs a "one-to-all" routing model, where each vehicle departs from and returns to a designated depot. The warehouse serves as the storage site and the departure point for vehicles. Vehicle routes are visually depicted with directional arrows, and polygons in various colors represent customer groups assigned to distinct routes. Products are loaded onto vehicles at the depot and delivered to their respective customers.

The model also considers vehicle storage constraints, ensuring that each vehicle's capacity accommodates the weight and quantity of transported goods. Two key assumptions underpin this model: (1) the total number of available vehicles is sufficient to meet the daily demand of all customers, and (2) each customer's daily order does not exceed the capacity of a single vehicle. Under these conditions, each vehicle is assigned a route to serve multiple customers and deliver various goods. While a single vehicle can cater to multiple customers along its route, only one vehicle is allocated to serve a particular customer at any given time.

The Vehicle Routing Problem with Time Windows (VRPTW) represents a complex combinatorial optimization problem that seeks to determine optimal routes for a vehicle fleet serving customers within specified time windows while satisfying capacity constraints. A prominent solution methodology for VRPTW is the two-phase Cluster-First Route-Second (CFRS) approach, which decomposes the problem into computationally tractable subproblems. The clustering phase partitions customers into geographically coherent groups using algorithms such as K-means, ensuring that vehicle capacity and temporal constraints are maintained within each cluster through appropriate parameter adjustments. Subsequently, the routing phase applies heuristic algorithm improvements to optimize vehicle routes within individual clusters while minimizing travel distance and satisfying time window constraints. This decomposition strategy reduces computational complexity from exponential to polynomial time for large-scale instances, enabling near-optimal solutions for practical applications. The CFRS methodology has demonstrated effectiveness in various logistics domains, including perishable goods distribution and urban delivery systems, where it successfully balances solution quality with computational efficiency. The approach's scalability and adaptability make it particularly suitable for large-scale VRPTW instances where exact methods become computationally prohibitive, thereby providing a practical framework for real-world logistics optimization applications.

While various clustering methodologies exist for addressing VRPTW applications, including hierarchical clustering, heuristic-based clustering approaches, and spectral clustering, K-means clustering has emerged as the most widely adopted approach in various domains due to its computational efficiency and scalability. Although K-means has not yet gained widespread adoption specifically in logistics optimization, its proven effectiveness in partitioning data points into coherent groups and its ability to handle large datasets efficiently make it a promising candidate for vehicle routing applications. Consequently, this research employs K-means clustering as the primary clustering methodology to investigate the comparative effectiveness of different cluster determination approaches in vehicle routing optimization.

A. K-means Clustering Algorithm

One well-known clustering technique is K-means clustering, which divides n observations into k clusters, where k is prioritized. The client's cluster is determined by the K-means clustering; a second clustering is then applied to each of the K-means clusters. As far as possible, the method aims to segregate each compact class and minimize the goal function. According to Khan and Ahmad [10], K-means clustering can be explained as follows.

First, the K-means algorithm selects k objects at random, each of which represents a mass of grouping relationships. Based on each grouping's mass to object distance, each object is then assigned to the most similar clustering. Next, figure out each clustering's new mass. Continue doing the aforementioned till the guideline function is put together. In general, the square error guideline function [11] is the adopted guideline function.

Assume that $X = \{x_1, x_2 \ldots, x_n\}$ is a set of observations, with d being the dimension of each real vector. c_k is the formula for a set of K centers: $K = \{1,2,\ldots,K\}$. With sj = {d | d is a member of the cluster k}, the set of samples that belong to the k^{th} the cluster is displayed. Euclidean distance is the distance between a point and the cluster center c_k, as given in (1).

$$\sum_{i=1}^{n} dist(d_i, c_k) \tag{1}$$

Step 1: Random sampling was used to generate a set of c_k.

Step 2: Decide each cluster's members according to the requirements for the minimum distance from the cluster center.

Step 3: Equation (2) will be used to calculate c_k. $|S_k|$ Represents the number of data elements in the k^{th} cluster.

$$c_k = \frac{\sum_{d_i \in S_k}^{n} d_i}{|S_k|} \tag{2}$$

Step 4: Until the objective is optimal, steps 2 and 3 could be repeated. When evaluating the K-means

clustering procedure, the Sum of Squares Error (SSE) criterion is most frequently utilized. The greatest results are obtained from the clustering result with the lowest SSE value. Equation (3) computes the sum of the squares of the object distances from the cluster center points [12].

$$SSE = \sum_{i=1}^{K} \sum_{x \in c_i} dist^2(m_i, x) \quad (3)$$

B. Determine the Optimal Number of K-Means Clusters

From the relevant research literature, multiple methodologies for determining the optimal number of clusters (k) in vehicle routing applications have been identified, each with distinct theoretical foundations and practical implications. Among the prominent approaches, Comert *et al.* [13] proposed a mathematical formulation for calculating the number of clusters based on operational constraints, specifically incorporating truck capacity and customer demand parameters. Their methodology determines cluster numbers by optimizing the truck utilization ratio, thereby directly linking clustering decisions to vehicle capacity management and operational efficiency. This approach represents a paradigm shift from traditional statistical clustering validation methods by prioritizing operational feasibility over purely geometric or statistical cluster quality measures. Additionally, the elbow method constitutes another widely recognized technique for cluster number determination, which employs a different theoretical framework based on the analysis of the within-cluster sum of squares, with details presented as follows:

1) Therefore, to solve a capacitated VRP problem using K-means clustering, Comert et al. [14] provided an equation for calculating the number of clusters. Employing (4) as the calculation formula, the number of clusters is determined by truck capacity and demand, or the truck utilization ratio.

$$\text{number of clusters} = \frac{\text{total demand}}{\text{truck capacity}} \quad (4)$$

2) The elbow approach uses the K-means clustering algorithm to plot the explained variations against the number of clusters. The elbow curve is then used to determine the number of clusters. The quality of aggregation within a cluster and the separation between clusters are represented by summing the squared errors of all data points within the cluster. Thorndike came up with the elbow method [14], which uses the variation graph (data dispersion) as a function of the number of clusters to compute the ideal number of clusters to utilize. The elbow curve is the result of this method. Bertagnolli [15] states that the Elbow approach can be expressed mathematically (5), (6) as follows:

$$W_k = \sum_{r=1}^{k} \frac{1}{n_r} D_r \quad (5)$$

$$D_r = \sum_{i=1}^{n_r - 1} \sum_{j=1}^{n_r} \left\| d_i - d_j \right\|_2 \quad (6)$$

Where W_k is the average internal sum of squares, and D_r are the sum of the distances between each point in a cluster, k is the number of the cluster, and n_r is the number of points in the cluster.

For different values of k (number of clusters), calculate the Sum of Squared Distances (SSE) between each data point and its nearest centroid. Plot the number of clusters (k) versus the SSE values. Then, locate the point on the graph where the SSE decline begins to level out and take the shape of an elbow. This is the ideal number of clusters.

III. Methodology

This research presents an experimental study focused on VRPTW applications, specifically investigating the comparative effectiveness of two fundamentally different approaches for determining the optimal number of clusters (k) in K-means clustering algorithms. This work conducts experimental investigations on VRPTW instances to evaluate two distinct methodologies for determining the optimal number of clusters (k) in K-means clustering: The truck utilization ratio approach and the elbow method. The objective of this study is to assess the comparative performance and effectiveness of these two clustering determination techniques in optimizing logistics operations and overall system efficiency within vehicle routing optimization scenarios.

The CFRS approach represents a systematic two-phase methodology for solving VRPTW by decomposing the complex optimization problem into computationally manageable subproblems. This methodology leverages K-means clustering in the first phase to partition customers into geographically coherent groups, followed by route optimization within each cluster in the second phase, as shown in Fig. 2.

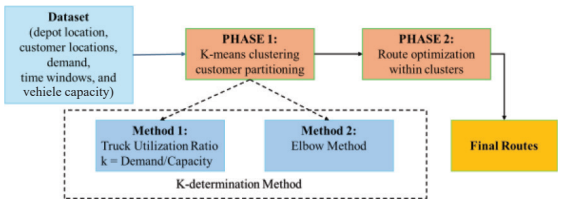

Fig. 2. CFRS methodology with different K-determination methods

In this study, standard VRPTW instances were employed, selected randomly to ensure unbiased representation. The analysis focused on comparing different subgroup initialization strategies for the K-means clustering method in the first phase of the

solution process. In the subsequent routing phase, vehicle capacity and time window constraints were imposed to reflect realistic operational conditions.

The performance of the designed algorithm is compared to models from the existing literature in this section through computational studies. Using Solomon's instances [16], six different types of problems that impact the behavior of algorithms for VRPTW are identified. They are divided into three categories: Random (R), Clustered (C), and Random-Clustered (RC). Of these, there are two types: Type 1, which has a short scheduling horizon (R1, C1, RC1), and type 2, which has a long scheduling horizon (R2, C2, RC2). The variables, which are drawn from Solomon [17], include the number of customers, geographic location, demand level, time windows (ready and due times), service time, and vehicle capacity. These benchmarks enable thorough testing of VRPTW algorithms in various scenarios.

VRPTW algorithms are still evaluated using the Solomon benchmark problems. These instances are divided into six groups according to operational characteristics, time window restrictions, and customer spatial distribution, with each problem's details presented as shown in Figs. 3 to Fig. 8.

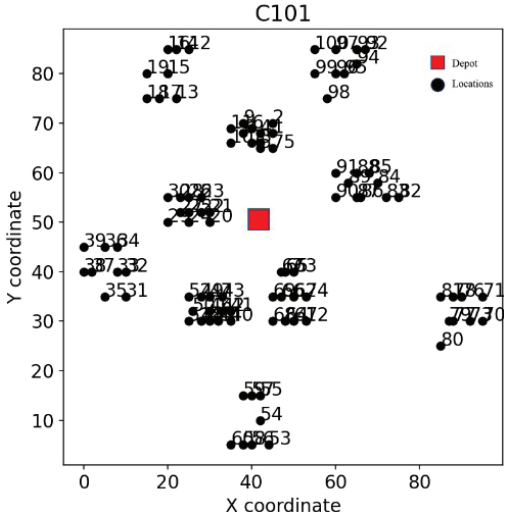

Fig. 3. Distribution of instance C101

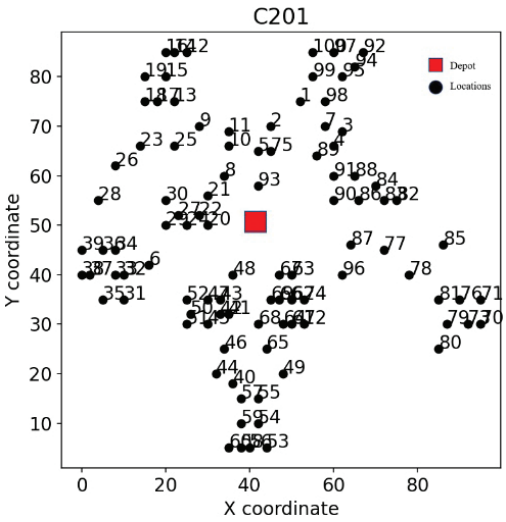

Fig. 4. Distribution of instance C201

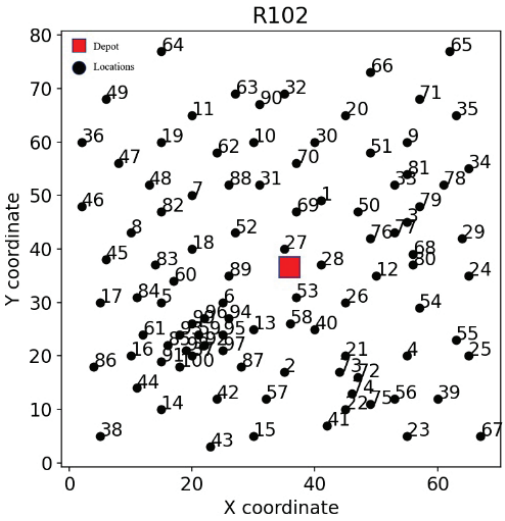

Fig. 5. Distribution of instance R102

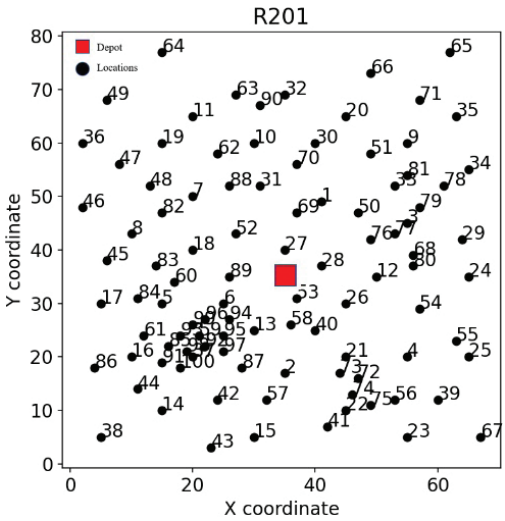

Fig. 6. Distribution of instance R201.

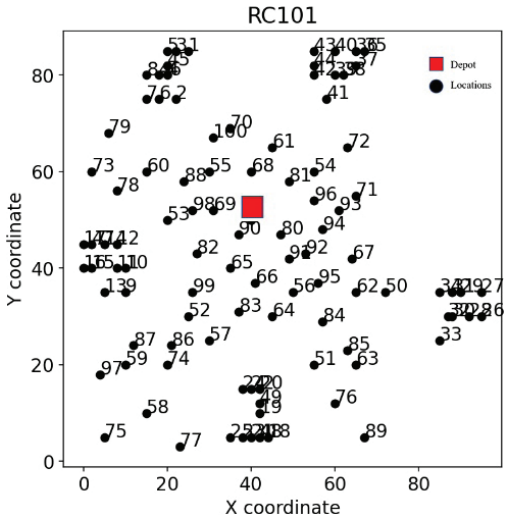

Fig. 7. Distribution of instance RC101

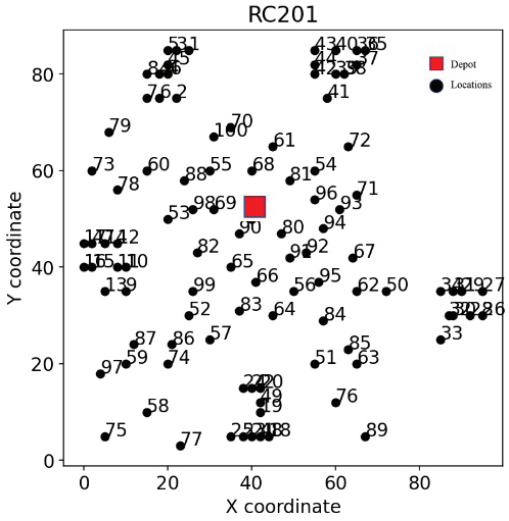

Fig. 8. Distribution of instance RC201

The strategy in this approach involves utilizing the K-means algorithm. Determining the appropriate number of clusters for a given dataset is a crucial step in this algorithm. The elbow method identifies the optimal number of clusters by examining the curve representing the within-cluster sum of squares plotted against the number of clusters. The elbow point on this curve indicates where adding additional clusters yields diminishing returns in variance reduction. Thus, the optimal number of clusters identified through the elbow method is then utilized in the K-means algorithm to perform clustering.

In this research, the experiment is conducted on the Solomon benchmark problem, which involves 26 problems: 5 problems of C1, 5 problems of C2, 5 problems of R1, 5 problems of R2, 3 problems of RC1, and 3 problems of RC2. The experiment was designed to compare the efficiency of routing with different K-means clustering methods, with each cluster being routed using OR-Tools' local search method. Employing local search to address vehicle routing problems is a pragmatic decision owing to its capacity to effectively traverse complex, large-scale solution spaces efficiently. Local search heuristics iteratively refine a candidate solution by exploring its nearby "neighborhood" of solutions, making small, incremental adjustments that often yield quick improvements in route cost or feasibility. This method is particularly valuable for VRP, which is NP-hard and difficult to solve optimally within a reasonable time, especially as the number of customers grows.

IV. Results

Based on Solomon's problem classification, the six problem types, R1, R2, C1, C2, RC1, and RC2, are distinguished by customer distribution and vehicle constraints. For R1 problems, which involve narrow time windows and low vehicle capacity, the elbow method produces a shorter total distance than the clustering approach proposed by Comert *et al.* [13], as measured by the truck utilization ratio. However, for R2 problems, which feature wider time windows and higher vehicle capacity, the clustering method by Comert *et al.* [13] achieves better performance in terms of total distance.

According to the findings of 26 experiments, the clustering by using the truck utilization ratio outperforms the elbow approaches for all 14 of the 26 instances, as shown in Table I and Fig. 9. The following are examples of the experimental findings from applying the CFRS approach in routing utilizing K-means with various techniques for determining the number of groups (k), namely the elbow method and truck utilization ratio: C101, and C203.

TABLE I
Fesible Solution

Instance	Elbow Method			Truck Utilization Ratio		
	Distance	**Car**	k	**Distance**	**Car**	k
C101	**1880.82**	20	5	1976.79	66	10
C102	1441.24	16	5	**1422.62**	41	10
C105	**1277.93**	15	5	1291.30	40	10
C108	892.50	11	5	**879.05**	21	10
C109	**723.78**	11	5	742.66	16	10
C201	**629.94**	8	5	648.81	4	3
C203	634.33	8	5	**568.05**	4	3
C205	623.53	7	5	**567.24**	4	3
C206	1449.01	11	5	**1350.08**	5	3
C207	840.62	8	5	**567.84**	4	3
R102	**1039.85**	12	4	1103.9	15	8
R103	**905.37**	11	4	930.43	12	8
R105	1031.43	12	4	**972.16**	15	8
R109	**838.95**	10	4	947.31	12	8
R112	756.22	9	4	**750.25**	9	8

TABLE I
FESIBLE SOLUTION (CON.)

Instance	Elbow Method			Truck Utilization Ratio		
	Distance	Car	*k*	Distance	Car	*k*
R201	1438.99	9	4	**1373.70**	6	2
R202	1302.69	8	4	**1203.58**	6	2
R203	1069.22	9	4	**1054.87**	4	2
R208	740.19	6	4	**710.58**	3	2
R210	**979.25**	7	4	985.45	5	2
RC101	**1126.71**	12	4	1176.68	17	9
RC103	**981.57**	10	4	1003.06	13	9
RC104	**857.34**	10	4	916.37	12	9
RC201	1584.65	10	4	**1507.91**	8	2
RC206	**1149.22**	8	4	1175.81	4	2
RC208	687.92	4	4	**671.76**	4	2

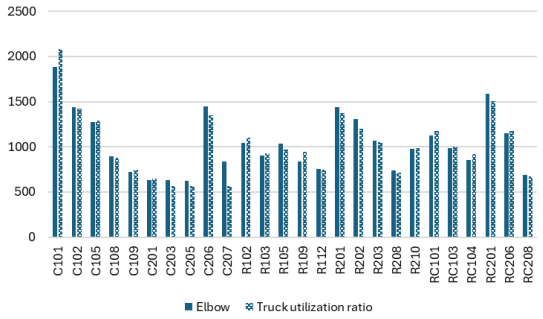

Fig. 9. Comparison results of methods for determining the number of groups

TABLE II
PAIRED T-TEST RESULTS

Dependent Variable	Mean		t-statistic	p-value
	Group 1 (Elbow Method)	Group 2 (Truck Utilization Ratio)		
Distance	1033.97	1019.16	.991	.331
Car	10.08	13.46	-1.47	.152

The results from the t-test indicate that there is no statistically significant difference between the two methods for either variable. The paired sample t-test showed no significant difference between the Elbow Method and the Truck Utilization Ratio for both distance (Elbow Method: Mean = 1033.97, Truck Utilization Ratio: Mean = 1019.16; t = 0.991, p = 0.331) and the number of trucks (Elbow Method: Mean = 10.08, Truck Utilization Ratio: Mean = 13.46; t = -1.47, p = 0.152). These findings indicate that both methods yield statistically comparable outcomes, suggesting that either approach can be applied without compromising routing efficiency or fleet utilization, as shown in Table II.

Establish the answer by the elbow method. For the example instance of C101 and C203. Start by dividing the data to determine the number of groups, which shows the results as shown in Figs. 10 and 11. After that, considering the characteristics of the points that form the elbow angle, which indicates that there should be how many groups (*k*) from the result, a total of five groups are divided based on the characteristics of the data in this problem. Next, divide the groups, which shows the results as shown in Figs. 12 and 13. Finally, work on finding the route sequence for each group using the OR tool by the local search method, which displays the results as shown in Tables III and IV.

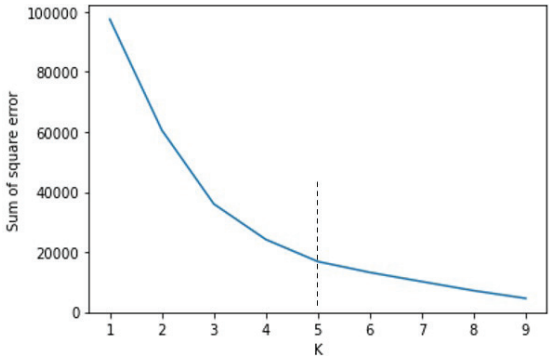

Fig.10. The result of determining *k*, for instance, C101, by the elbow method

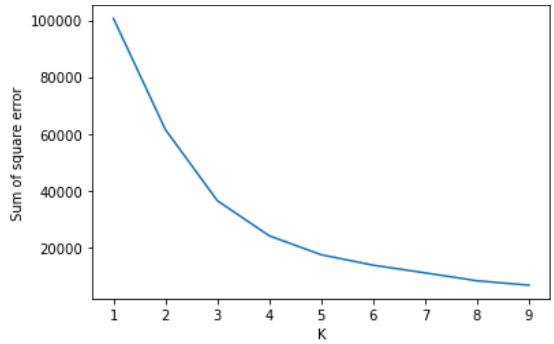

Fig. 11. The result of determining *k*, for instance, C203, by the elbow method

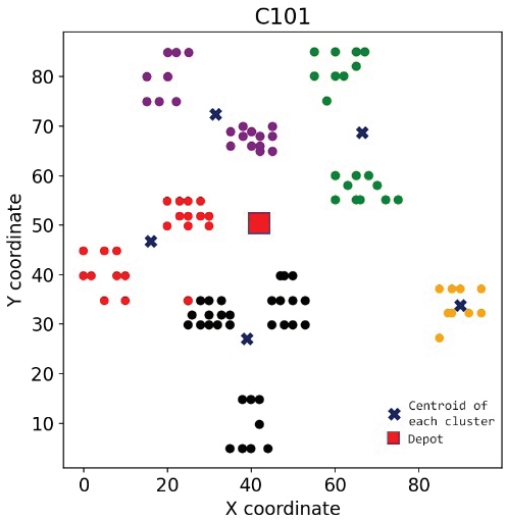

Fig. 12. Clustering by the elbow method result for instance C101

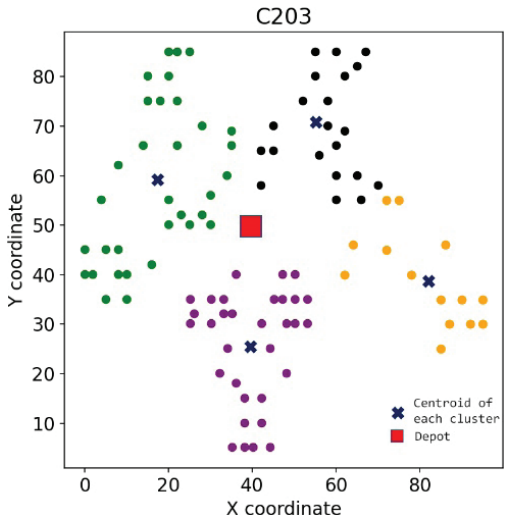

Fig. 13. Clustering by the elbow method result for instance C203

TABLE III
FEASIBLE SOLUTION OF C101 BY THE ELBOW METHOD

Number of Clusters	Route	Sequencing Order	Demand	Distance
$k = 1$	1	0-90-98-96-87-86-95-83-94-92-82-0	160	187.41
	2	0-84-93-85-97-100-88-89-99-91-0	200	188.73
$k = 2$	3	0-61-64-59-68-51-50-66-0	70	102.39
	4	0-69-0	10	15.81
	5	0-67-43-42-57-55-65-0	100	76.17
	6	0-49-47-0	20	21.21
	7	0-41-40-62-44-56-72-46-58-60-45-48-0	190	191.35
	8	0-63-54-53-74-0	160	81.90
$k = 3$	9	0-20-24-32-33-25-31-27-35-29-37-0	200	166.47
	10	0-30-38-28-39-26-36-23-34-22-52-21-0	180	251.06
$k = 4$	11	0-70-73-0	40	61.52
	12	0-76-71-0	30	57.20
	13	0-80-0	10	51.48
	14	0-77-79-0	20	53.00
	15	0-81-78-0	50	50.43
$k = 5$	16	0-18-19-8-0	50	66.30
	17	0-5-3-13-17-7-0	90	65.83
	18	0-2-0	30	20.62
	19	0-10-15-11-16-9-14-12-6-4-0	170	150.34
	20	0-1-75-0	30	21.60

TABLE IV
FESIBLE SOLUTION OF C203 BY THE ELBOW METHOD

Number of clusters	Route	Sequencing order	Demand	Distance
$k = 1$	1	0-50-51-52-0	30	30.04
	2	0-21-0	20	11.66
	3	0-20-22-24-27-30-29-6-32-33-31-35-37-38-39-36-34-28-0	310	87.76
$k = 2$	4	0-83-82-85-76-71-70-73-80-79-81-78-77-87-96-0	240	124.47
$k = 3$	5	0-26-23-18-19-16-14-12-15-17-13-25-9-11-10-8-0	300	116.34
$k = 4$	6	0-90-0	10	20.62
	7	0-93-5-75-2-1-99-100-97-92-94-95-98-7-3-4-89-91-88-84-86-0	370	106.55
$k = 5$	8	0-67-63-62-74-72-61-64-66-69-68-65-49-55-54-53-56-58-60-59-57-40-44-46-45-47-43-42-41-48-0	530	136.89

When applying the by-truck utilization ratio technique to solve sample instances C101 and C103, the number of groups (k) is determined by dividing the problem's overall demand by the total number of vehicles available. Fig. 14, which is the solution to instance C101, then shows how members of each group are found using clustering. Instance C203 has an answer in Fig.15. Then, using OR Tools and the local search method, the routes are determined. Tables IV and V, respectively, display the results.

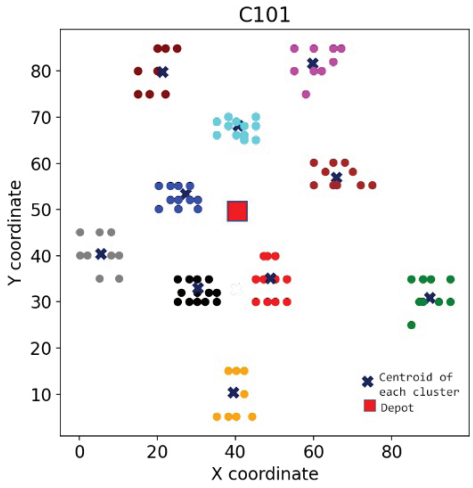

Fig. 14. Clustering by truck utilization ratio result for instance C101

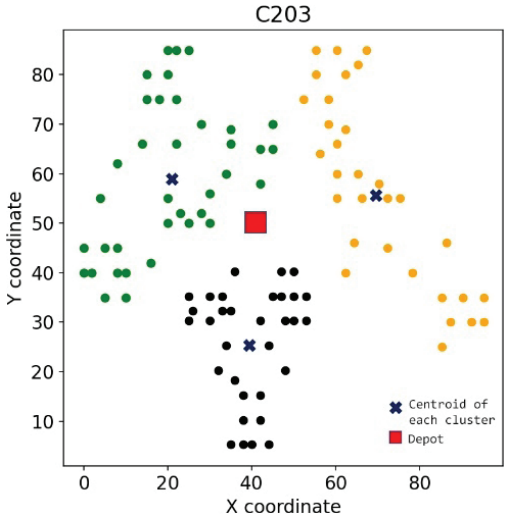

Fig. 15. Clustering by truck utilization ratio result for instance C203

TABLE V
FESIBLE SOLUTION OF C101 BY TRUCK UTILIZATION RATIO

Number of Clusters	Route	Sequencing Order	Demand	Distance
$k = 1$	1	0-42-43-0	30	22.31
	2	0-49-47-0	20	21.21
	3	0-50-52-0	20	25.96
	4	0-48-51-0	20	26.32
	5	0-46-45-0	40	22.59
	6	0-41-40-0	20	20.68
	7	0-44-0	10	21.54
$k = 2$	8	0-70-73-0	40	61.52
	9	0-76-71-0	30	57.20
	10	0-80-0	10	51.48
	11	0-77-79-0	20	53.00
	12	0-81-78-0	50	50.43
$k = 3$	13	0-30-0	10	20.62
	14	0-29-0	10	20.00
	15	0-27-0	10	17.12
	16	0-28-26-0	30	19.72
	17	0-24-25-0	50	17.00
	18	0-23-0	10	13.00
	19	0-22-21-0	40	14.17
	20	0-20-0	10	10.00
$k = 4$	21	0-83-82-0	30	35.39
	22	0-84-85-0	50	33.88
	23	0-87-86-0	30	26.50
	26	0-90-0	10	20.62
$k = 5$	27	0-58-60-0	50	48.04
	28	0-56-0	30	45.00
	29	0-54-53-0	60	45.44
	30	0-59-0	10	35.06
	31	0-57-55-0	50	37.00
$k = 6$	32	0-93-0	40	43.01
	33	0-94-92-0	30	44.22
	34	0-97-100-0	50	45.31
	35	0-95-0	30	37.20
	36	0-99-0	10	33.54
	37	0-98-96-0	30	36.20
$k = 7$	38	0-38-0	30	41.23
	39	0-39-0	20	40.31
	40	0-37-0	20	39.29
	41	0-35-0	10	38.08
	42	0-36-0	10	35.36
	43	0-31-0	20	33.54
	44	0-34-0	20	32.39
	45	0-32-33-0	70	33.62
$k = 8$	46	0-72-61-0	20	26.85
	47	0-64-0	10	21.54
	48	0-68-0	10	20.62
	49	0-74-0	50	19.85
	50	0-62-0	20	18.03
	51	0-66-0	10	16.55
	52	0-69-0	10	15.81
	53	0-63-0	50	14.14
	54	0-67-65-0	20	13.21
$k = 9$	55	0-16-0	40	40.31
	56	0-14-12-0	30	42.36
	57	0-15-0	40	36.06
	58	0-18-19-0	30	40.36
	59	0-13-17-0	50	34.81

TABLE V
FESIBLE SOLUTION OF C101 BY TRUCK UTILIZATION RATIO (CON.)

Number of Clusters	Route	Sequencing Order	Demand	Distance
$k = 10$	60	0-2-0	30	20.62
	61	0-11-9-0	20	22.81
	62	0-6-4-0	30	21.24
	63	0-10-0	10	16.76
	64	0-7-8-0	40	18.83
	65	0-1-75-0	30	21.68
	66	0-5-3-0	20	16.13

TABLE VI
FESIBLE SOLUTION OF C203 BY TRUCK UTILIZATION RATIO

Number of Clusters	Route	Sequencing Order	Demand	Distance
$k = 1$	1	0-93-75-2-5-0	100	26.70
	2	0-20-22-24-27-30-29-6-32-33-31-35-37-38-39-36-34-28-26-23-18-19-16-14-12-15-17-13-25-9-11-10-8-21-0	630	183.64
$k = 2$	3	0-67-63-62-74-72-61-64-66-69-68-65-49-55-54-53-56-58-60-59-57-40-44-46-45-51-50-52-47-42-41-43-48-0	560	146.91
$k = 3$	4	0-1-99-100-97-92-94-95-98-7-3-4-89-91-88-86-84-83-82-85-76-71-70-73-80-79-81-78-77-96-87-90-0	520	210.80

The C1 and C2 categories include customers clustered in groups, where C1 has narrow time windows and low vehicle capacity. Results from C1-type problems are arranged using the elbow method at a smaller distance. Regarding C2, wide time windows and large vehicle capacity, along with the vehicle routing by truck utilization ratio [1], provide better results.

The RC1 and RC2 categories blend randomly distributed and clustered customers, with RC1 having narrow time windows and low vehicle capacity. Although RC1 has low vehicle capacity and short windows, it performs better when implemented with the elbow method. RC2 has broad time frames and a high vehicle capacity. The truck utilization ratio [13] was used to improve the results.

The sensitivity analysis was carried out by comparing the distance outputs obtained from the Elbow Method and the Truck Utilization Ratio across multiple vehicle routing instances. For each instance, the absolute difference was calculated as the absolute deviation between the two methods, while the percentage difference was derived by normalizing the deviation against the Elbow Method baseline. These measures allowed for both direct and relative comparisons of the two approaches. Subsequently, summary statistics, including mean deviations and the identification of maximum and minimum discrepancies, were computed to assess overall trends. To further illustrate the findings, bar charts and scatter plots were employed, with the percentage differences specifically presented in Fig. 16, providing visual insights into the degree of sensitivity across all instances.

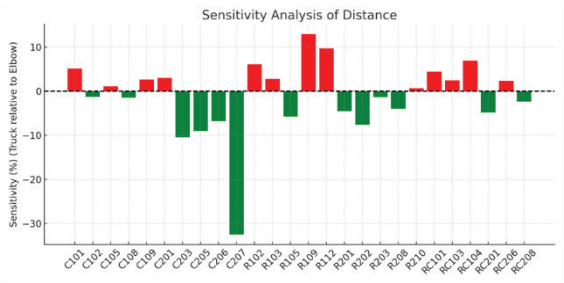

Fig. 16. Percentage differences between the Elbow Method and the Truck Utilization Ratio across all instances

The experimental results demonstrate comparative performance between the Elbow Method and the Truck Utilization Ratio across 26 benchmark instances. In terms of routing distance, the Elbow Method produced shorter routes in approximately 60% of the cases, whereas the Truck Utilization Ratio outperformed in the remaining 40% of the instances. The average sensitivity, defined as the relative percentage change in total distance, was +1.2%, suggesting a slight overall advantage for the Elbow Method. However, the variability was substantial, ranging from –33% (favoring Truck Utilization Ratio) to +13% (favoring Elbow Method).

The graphical comparison (Fig. 9) shows that while most instances present only minor differences, certain cases reveal significant improvements when applying the Truck Utilization Ratio. Fig. 16 highlights these differences by illustrating sensitivity values for each instance, clearly indicating which method yields shorter routes. These findings highlight that the reliability of either method is not uniform across all instances. The sensitivity appears to be influenced by spatial and demand heterogeneity within the dataset. Consequently, practitioners should interpret results with caution, particularly when applying these methods to diverse or irregular problem instances.

V. Conclusion

The location of the logistics center is a significant strategic consideration for logistics system optimization. The purpose of this work was to implement a method for data analysis that optimizes the vehicle routing process by applying ensemble approaches and a two-phase algorithm. Two different approaches were set up to accomplish this goal, each of which used a clustering model to organize delivery points (customers) into clusters. Effective customer grouping was made possible using the elbow method and truck utilization ratio for clustering, which supplied essential information for the development of routing techniques. The adaptability of the suggested methodology was shown by the application of two different methods, each focused on a particular clustering model.

In summary, while both approaches can be applied effectively to vehicle routing problems, the Elbow Method provides a more stable baseline, whereas the Truck Utilization Ratio represents a practical alternative that should be validated against specific dataset characteristics. Further investigation into the underlying factors contributing to high-sensitivity cases is recommended to enhance methodological reliability and improve decision-making accuracy in logistics planning.

According to the results of the experiments, the K-means and truck utilization ratio are used in the strategies. The truck utilization ratio outperforms the elbow method for the K-means algorithm in terms of overall results, and the strategy performs satisfactorily in the total distance driven by trucks while maintaining a balanced distribution of the distance traveled. This study addresses existing issues and suggests future research areas by offering useful information on fleet routing through heuristic approaches in routing and data analysis in clustering. This effort will make a significant impact on the area of logistics and transportation operations.

References

[1] P. Toth and D. Vigo, *Vehicle Routing: Problems, Methods, and Applications*, 2nd ed, Philadelphia, PA: SIAM, 2014, pp. 1-8.

[2] M. Haonan, Y. C. He, M. Huang, Y. Wen, Y. Cheng, and Y. Jin, "Application of K-means clustering algorithms in optimizing logistics distribution routes," in *Proc. 6th Int. Conf. Systems and Informatics (ICSAI)*, 2019, pp. 1466-1470.

[3] R. G. Dondo and J. Cerda, "A cluster-based optimization approach for the multi-depot heterogeneous fleet vehicle routing problem with time windows," *Eur. J. Oper. Res.*, vol. 176, no. 3, pp. 1478-1507, Feb. 2007, https://doi.org/10.1016/J.EJOR.2004.07.077

[4] C. Ren, "Research on VRPTW optimizing based on k-means clustering and IGA for electronic commerce," in *Proc. 3rd IEEE Conf. Ind. Electron. Appl.*, 2008, pp. 61-66.

[5] M. Schneider, A. Stenger, and D. Goeke, "The electric vehicle-routing problem with time windows and recharging stations," *Transp. Sci.*, vol. 48, no. 4, pp. 500-520, Mar. 2014, https://doi.org/10.1287/trsc.2013.0490

[6] A. F. L. Villalba and E. C. G. L. Rotta, "Clustering and heuristics algorithm for the vehicle routing problem with time windows," *Int. J. Ind. Eng. Comput.*, vol. 13, no. 2, pp. 165-184, 2022, https://doi.org/10.5267/j.ijiec.2021.12.002

[7] G. D. Konstantakopoulos, S. P. Gayialis, and E. P. Kechagias, "Vehicle routing problem and related algorithms for logistics distribution: A literature review and classification," *Oper. Res. (Lond.)*, vol. 22, no. 3, pp. 2033-2062, Sep. 2020, https://doi.org/10.1007/s12351-020-00600-7

[8] L. Moccia, J.-F. Cordeau, and G. Laporte, "An incremental tabu search heuristic for the generalized vehicle routing problem with time windows," *J. Oper. Res. Soc.*, vol. 63, no. 2, pp. 232-244, Feb. 2012, https://doi.org/10.1057/jors.2011.25

[9] Y. Wang, L. Wang, G. Chen, Z. Cai, Y. Zhou, and L. Xing, "An improved ant colony optimization algorithm to the periodic vehicle routing problem with time window and service choice," *Swarm Evol. Comput.*, vol. 55, p. 100675, Jun. 2020, https://doi.org/10.1016/j.swevo.2020.100675

[10] S. S. Khan and A. Ahmad, "Cluster center initialization algorithm for K-means clustering," *Pattern Recognit. Lett.,* vol. 25, no. 11, pp. 1293-1302, Aug. 2004, https://doi.org/10.1016/j.patrec.2004.04.007

[11] R. Chunyu and W. Xiaobo, "Research on VRP optimizing based on hierarchy clustering and IGA under common distribution," in *Proc. 2006 Int. Conf. Comput. Intell. Secur.*, 2006, pp. 143-146. https://doi.org/10.1109/ICCIAS.2006.294108

[12] K. C. Tan, L. H. Lee, Q. L. Zhu, and K. Ou, "Heuristic methods for vehicle routing problem with time windows," *Artif. Intell. Eng.*, vol. 15, no. 3, pp. 281-295, Jul. 2001, https://doi.org/10.1016/s0954-1810(01)00005-x

[13] S. E. Comert, H. R. Yazgan, S. Kır, and F. Yener, "A cluster first-route second approach for a capacitated vehicle routing problem: A case study," *Int. J. Procurement Manage.*, vol. 11, no. 4, p. 399, Jan. 2018, https://doi.org/10.1504/ijpm.2018.092766

[14] R. L. Thorndike, "Who Belongs in the Family?," *Psychometrika*, vol. 18, no. 4, pp. 267-276, Dec. 1953, https://doi.org/10.1007/bf02289263

[15] N. Bertagnolli, "Elbow method and finding the right number of clusters." *Nicolas Bertagnolli*, 2015. [Online]. Available: https://www.nbertagnolli.com/jekyll/update/2015/12/10/Elbow.html [Accessed: Apr. 2, 2025].

[16] M. M. Solomon, "Algorithms for the vehicle routing and scheduling problems with time window constraints," *Operations Research*, vol. 35, no. 2, pp. 254-265, Apr. 1987, https://doi.org/10.1287/opre.35.2.254

[17] E. Queiroga, "CVRPLIB: Capacitated vehicle routing problem library," *Pontifical Catholic University of Rio de Janeiro*, 2025. [Online]. Available: https://vrp.galgos.inf.puc-rio.br/index.php/en/ [Accessed: Sep 20, 2025].

Kanokporn Boonjubut is a lecturer in the Department of Engineering Management at Nakhon Rachasima Rajabhat University, Thailand. She received her Ph.D. degree in Functional Control Systems from Shibaura Institute of Technology (SIT), Japan. Her research interests include optimization, logistics, and supply chain management.

Prat Boonsam is an Assistant Professor of the Department of Engineering Management at Nakhon Rachasima Rajabhat University, Thailand. He received his Ph.D. in Logistics from the University of the Thai Chamber of Commerce, Thailand. His interests include truck distribution planning and industrial productivity improvement.

Sirichai Yodwangjai is an Assistant Professor in the Department of Industrial Engineering Technology, College of Industrial Technology, King Mongkut's University of Technology North Bangkok, Thailand. He received a Ph.D. from Naresuan University, Phitsanulok, Thailand. His research interests are optimization, metaheuristics, logistics, and supply chain.

Intelligent Mobile-Based Detection of Shrimp Weight Anomalies Using Random Forest Regression

Kanjana Eiamsaard[1], Kathawach Satianpakiranakorn[2], Anan Banharnsakun[3], and Jirawat Jitprasutwit[4*]

[1,2,3,4]Department of Computer Engineering, Faculty of Engineering at Sriracha, Kasetsart University Sriracha Campus, Thailand

Email: kanjana@eng.src.ku.ac.th, kathawach@eng.src.ku.ac.th, ananb@ieee.org, jirawat@eng.src.ku.ac.th[*]

Received: December 11, 2024 / Revised: July 28, 2025 / Accepted: August 13, 2025

***Abstract*—Shrimp is one of the most widely consumed seafood items globally, yet consumers frequently encounter fraud, such as weight manipulation through adulteration injections, which poses significant health and economic risks. This research presents a practical system for detecting anomalies in shrimp weight. A cross-platform mobile application has been developed to classify shrimp as either normal or abnormal in weight. The application integrates a shrimp segmentation model, developed using Mask R-CNN, and a weight prediction model based on the random forest algorithm, utilizing features such as area, perimeter, length, and width of the shrimp image. The weight prediction model achieves a value of 0.821 and a Mean Absolute Error (MAE) of 1.786 grams, which is less than 10% of the average shrimp weight in the dataset. Final classification is performed by comparing the predicted weight with the actual weight, measured using a 7-segment digit recognition module. The developed mobile application represents a novel integration of machine learning with mobile technology to address both non-adulterated and adulterated shrimp scenarios. It offers a reliable, accessible tool for consumers to detect weight-based adulteration, thereby helping to mitigate health risks and economic losses in the seafood supply chain.**

***Index Terms*—Anomaly Detection, Weight Prediction, Shrimp Fraud, Authentic Food, Food Engineering, Random Forest**

I. Introduction

Authentic food plays a vital role in human well-being. Today, various efforts, both digital and non-digital [1]-[3], are being employed to enhance the seafood supply chain. These efforts encompass improvements in farming [4]-[7], classification [8]-[10], and most importantly, the elimination of fraud utilizing both technology [11]-[14] and policy [15]-[17]. There are nine recognized types of fraud, commonly referred to as the 'nine sins of seafood'. Such fraudulent practices undermine food integrity, pose risks to public health, and have adverse economic impacts.

Undeclared product extension is a type of fraud that involves using technology to increase the perceived weight of seafood. For example, injecting gelatin-like substances, derived from animal skins and bones, into shrimp can increase their weight by 20-30% [18] and also make them appear larger. This practice poses a serious threat to international standards by endangering consumer health through various side effects.

Shrimp is the most-consumed seafood product in the United States. U.S. citizens face the problem of shrimp fraud, which led to the founding of the Southern Shrimp Alliance, an organization that works to protect millions of U.S. shrimp consumers from such fraud. This problem is not limited to the U.S. but also occurs in Japan and many other countries. Since ASEAN is one of the biggest shrimp exporters, its member nations have been experiencing incidents of fraud and adulteration for the past 20 years [19]-[21].

Detecting adulteration that increases shrimp weight is challenging without scientific laboratory tools. This issue could potentially be addressed through shrimp weight prediction or estimation research. In studies [22], [23], a specialized setup was utilized to capture the shadow of the shrimp area, with weight predictions made using power and forced power equations. Another study [24] proposed a method for predicting the weight of shelled shrimp using machine vision. This approach involved predicting weight through a polynomial equation based on the shrimp's area and perimeter pixel features, which were extracted using image processing methods. However, this system is not user-friendly due to the prerequisite hardware and the software being developed for personal computers. In study [25],

a computer program was proposed for estimating the weight of Vannamei shrimp. The program utilized the number of pixels in conjunction with a non-linear regression equation for weight estimation. However, the system has limitations, as shrimp with the same number of pixels can have significantly different weights. While previous studies contribute valuable techniques, they are often constrained by limited accuracy in adulterated cases, reliance on specialized equipment, and lack of real-time, mobile-ready deployment. Most existing systems are designed for desktop platforms, which limits their usability for smartphone consumers. Currently, few solutions fully provide an integrated, consumer-accessible system capable of detecting shrimp weight anomalies in practical environments.

To provide a solution tailored for real-life conditions, it is essential to have convenient tools for detecting anomalies in shrimp weight, especially tools that are easy to use. The primary benefit of such a system is its accessibility, as it eliminates the need for specialized laboratory equipment, making it suitable for both shrimp consumers and businesses. By accurately detecting weight-based adulteration in shrimp, the system mitigates the risks associated with consuming products injected with gelatin-like substances, thereby protecting public health. Additionally, it promotes economic integrity by preventing fraudulent practices in the seafood supply chain, which can lead to financial losses for consumers and businesses alike. The adoption of this tool enhances consumer trust and promotes adherence to international food safety standards, contributing to a healthier and more transparent seafood industry.

Given these advantages, this research proposes a real-time system for detecting shrimp weight anomalies, thereby bridging the gap between research innovations and practical consumer needs. The developed system enables users to determine whether a shrimp's weight is normal or abnormal by capturing an image of the shrimp placed on a digital weighing scale, with the output simply indicating either 'Normal' or 'Abnormal'. The system consists of a cross-platform mobile application that integrates shrimp detection, morphological feature extraction, 7-segment digit recognition, and weight prediction.

II. Objective

This study aims to develop an intelligent and practical mobile application for shrimp consumers that can detect weight-based adulteration in shrimp.

III. Materials and Methods

The proposed system consists of a cross-platform mobile application, Shrimp, a digital weighing scale, and an Application Programming Interface (API) server. The process begins with the user capturing a top-view photograph of a shrimp placed on the digital weighing scale using the developed mobile application. This image is then transmitted to the API server over a wireless network. Upon receiving the image, the API server processes it to classify the result of shrimp weight anomaly detection, as illustrated in Fig. 1.

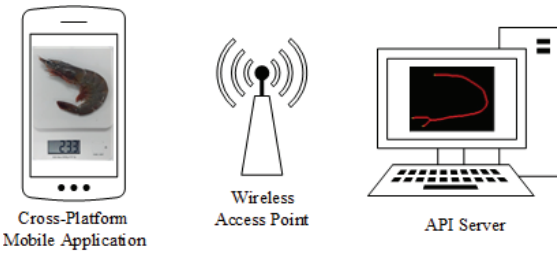

Fig. 1. Proposed system overview

The system workflow starts with the user capturing a photo of the shrimp placed on a digital weighing scale using the mobile application. The system then separates the shrimp image from the scale display to recognize the digits on the 7-segment display. Simultaneously, it generates a shrimp mask to extract the necessary features. The shrimp weight is predicted using a machine learning model. These two results—the actual weight from the scale and the predicted weight—are then compared to classify the shrimp as either 'normal' or 'abnormal'. Finally, all input and output data are stored in a cloud database, and relevant information is presented to the user via the mobile application, as shown in Fig. 2. The proposed system was developed across seven modules, which are described in the following subsections.

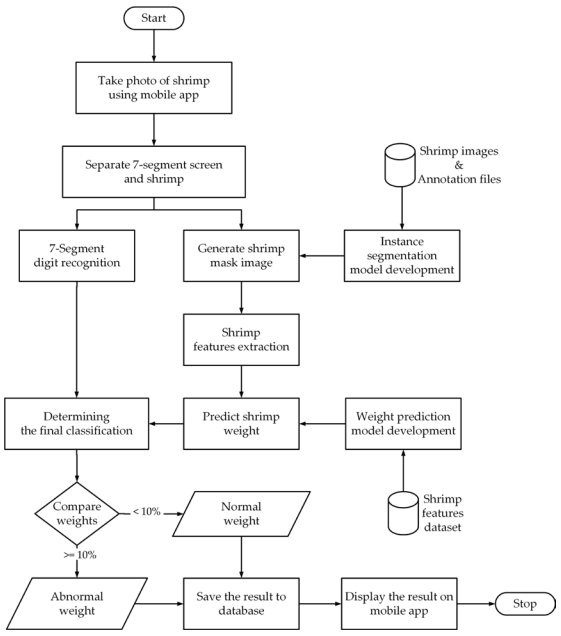

Fig. 2. The proposed system workflow

1) Cross-Platform Mobile Application Development

The mobile application was developed in two parts: the frontend and the backend. Flutter was chosen as the frontend framework due to its ability to build mobile, web, and desktop applications from a single codebase. In this research, which aims to provide a practical approach for identifying anomalies affecting shrimp weight, the mobile application serves multiple functions: Capturing images of shrimp on a digital weighing scale, detecting the 7-segment display, and providing the user interface for interacting with the instance segmentation and weight prediction model.

As illustrated in Fig. 1, the proposed system utilizes an API server to handle high-computation tasks, a common approach in research within this field [26]. FastAPI was chosen as the backend development framework due to its high performance in API management [27]. By employing this technique, the system avoids the challenges of deploying machine learning models directly on mobile devices [28].

Two API endpoints were implemented: the first utilizes the HTTP POST method for preprocessing and uploading shrimp images to cloud storage, along with storing related data in a cloud database. The second endpoint employs the HTTP GET method to return shrimp weight predictions, incorporating both feature extraction and the execution of a shrimp weight prediction model.

The authentication system, including sign-in and sign-up modules, seamlessly integrates with cloud-based authentication services. Additionally, data such as shrimp images, user locations, and prediction results are securely stored in a NoSQL database, leveraging appropriate cloud infrastructure.

2) 7-Segment Digit Recognition

In this research, digit recognition from 7-segment displays was facilitated using a point-by-point color comparison method. This technique analyzes the color at seven key points of the 7-segment display, converting this data into digital values, as shown in Fig. 3. This method ensures accurate and rapid digit recognition under varied lighting conditions, outperforming traditional OCR methods, which often struggle with segmented displays [29]. As shown in Fig. 4 (a-c), this process involves converting the original image to binary and setting the reading points of the 7 segments.

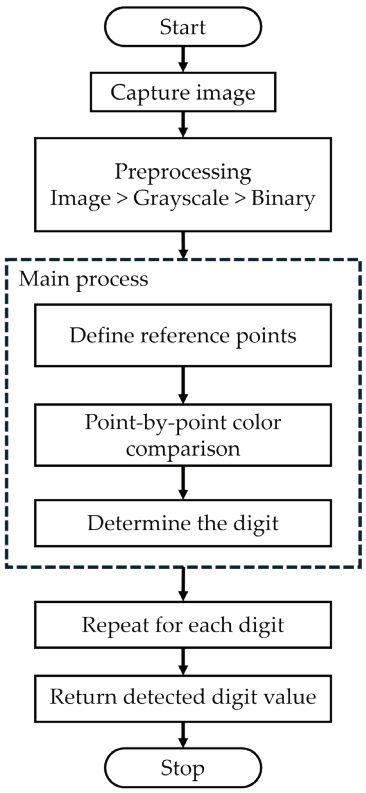

Fig. 3. The 7-Segment digit recognition workflow

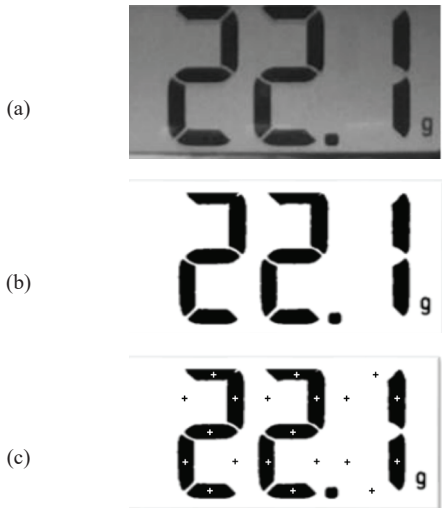

Fig. 4. The 7-Segment digit recognition process: (a) Original image of numbers from a digital scale, (b) Image converted to binary, (c) Setting the reading points of the 7 segments

A notable limitation of this method is the need to define a precise frame for capturing images, which can be challenging and lead to errors if not done correctly. Ensuring that the picture frame matches the reference in the application can be difficult, potentially affecting the accuracy of digit recognition. To address this, integrating LiDAR technology in smartphones was considered. LiDAR can dynamically adjust the focus and framing based on distance, facilitating optimal image capture. However, the limited availability of LiDAR in high-end models restricts widespread use, indicating a need for future research on more accessible solutions [29].

3) Shrimp Dataset Collection

The shrimp dataset used in this research was gathered using four different mobile devices. Each captured image showed a shrimp placed on a digital weighing scale. As shown in Fig. 5, the dataset included variations in the digital weighing scale, the shrimp's pose, and the mobile device used for image capture. The dataset contained a total of 1,286 images.

Fig. 5. Examples of images in the dataset

4) Instance Segmentation Model Development

A shrimp instance segmentation model was developed using the Mask R-CNN, utilizing MMDetection, a comprehensive toolbox for object detection and instance segmentation. Built on PyTorch and distributed under an open-source license, MMDetection supports numerous well-known models such as Mask R-CNN, YOLO, and Cascade R-CNN. It has been benchmarked using standard datasets, including COCO, PASCAL VOC, and Cityscapes, and is optimized for both speed and memory efficiency during training and inference. Additionally, MMDetection's modular architecture allows developers to easily modify the toolbox to suit specific requirements [31].

This process involved both dataset annotation and model development. The VGG Image Annotator was used to annotate the dataset and establish ground truth. Model development focused on tuning dataset-specific, model-specific, and training-specific hyperparameters.

During annotation, each shrimp image was marked with a polygon outlining the shrimp's edges, and the entire shrimp was labeled as 'white_shrimp'. The annotated dataset was then formatted according to the COCO standard.

The developed model was evaluated using the CocoMetric class, which supports various standard metrics, including Average Precision and Average Recall at different Intersection over Union (IoU) thresholds. These metrics assess both bounding box and instance segmentation performance. Once the desired metrics were achieved, the final model produced a mask image as output. In this mask image, black pixels represent the shrimp, and white pixels represent the background.

5) Shrimp Features Extraction

Regression analysis is the primary method for developing shrimp weight prediction models [32], [33]. While various imagery techniques can extract predictive features, including statistical, textural, and color-based features [34], [35] morphological features have shown the strongest correlation with shrimp weight. This is because shrimp have a distinctive morphology, with curved bodies exhibiting a weight directly proportional to their size. Four key morphological features are extracted from shrimp images: Total area, perimeter, head-to-tail length, and maximum width. These measurements are expressed in pixels and derived using pixel counting, contour analysis, skeletonization, and circular base measurement, respectively [36].

This investigation employed a four-step feature extraction process to derive these morphological traits from shrimp images, which are crucial for accurate weight prediction. Each step is detailed below.

First, the shrimp's area was quantified. This was achieved by counting the black pixels within the mask image, with each pixel representing a part of the shrimp to provide a total area. Fig. 6 (a) shows the area inside the shrimp.

Second, the perimeter was calculated. The shrimp's contour was detected in the mask image, and the number of pixels along the contour was counted. Fig. 6 (b) shows the perimeter of the shrimp.

Third, the shrimp's length was determined. The mask image was skeletonized, as depicted in Fig. 7 (a), and endpoints were identified on the resulting structure, as shown in Fig. 7 (b). Distances between all pairs of endpoints were calculated. The endpoints with the maximum distance were used to denote the shrimp's head-to-tail length, as illustrated in Fig. 7 (c).

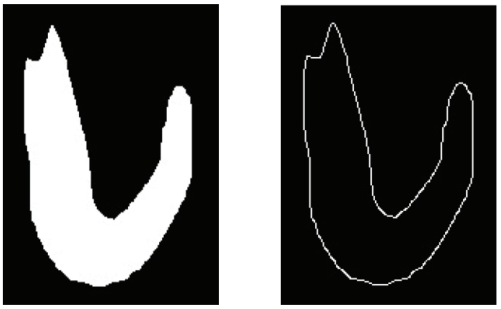

(a) (b)

Fig. 6. The process of determining shrimp area and perimeter: (a) The area of the shrimp, (b) The perimeter of the shrimp

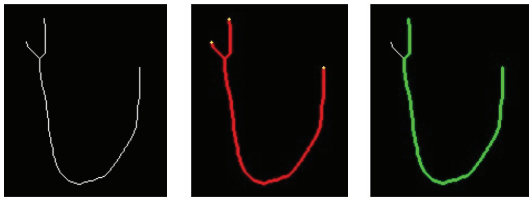

(a) (b) (c)

Fig. 7. The process of determining shrimp length: (a) Skeleton from the mask image, (b) Endpoints on the skeleton, (c) Calculated length between endpoints

Finally, the shrimp's width was measured. This was achieved by iteratively placing increasingly larger circles over the mask image until the shrimp region was fully encompassed. The diameter of the encompassing circle represents the shrimp's width. To enhance efficiency, the Multiscale Approximation (MSA) technique was employed, downscaling the image to quickly identify the optimal placement for this circle. Fig. 8 shows the width determination results, which were verified using 16 points by checking the number of white pixels within the circle.

The extracted features and their corresponding weights in grams were compiled into a structured dataset. This dataset was used for the development of the weight prediction model, facilitating further analysis and model training.

6) Weight Prediction Model Development

The weight prediction model developed in this research is a supervised learning model, implemented using both linear and non-linear regression algorithms. For non-linear regression, the Random Forest algorithm, which leverages the bagging ensemble learning method, was designed and utilized. A Random Forest consists of multiple base learners, denoted as decision trees, each trained using a sample from feature randomness. Once each learner has produced a continuous value, all values are averaged to produce the final output, as shown in Fig. 9.

By using the bagging ensemble algorithm, Random Forests address the high variance of decision tree models without increasing bias. Moreover, bagging requires less computation time than most machine learning algorithms when training on large datasets [37], and it has been utilized across several research domains [38], [39].

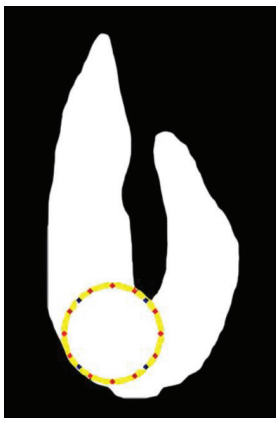

Fig. 8. The shrimp's width is measured by iteratively placing a 16-point circle entirely encompassing the shrimp region

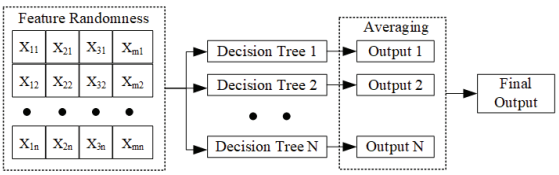

Fig. 9. Bagging ensemble algorithm in random forest regression.

The developed model utilizes features extracted from the shrimp feature extraction process. Specifically, the features denoted as area, perimeter, length, and width are considered as independent variables, while the weight is treated as the dependent variable. Before model development, the entire dataset was visualized to identify and eliminate outliers. The dataset was then randomly split into training and testing sets. All features in the dataset were standardized as in (1), where z represents the standardized samples, is the original sample, x is the mean of the sample, μ and is the standard deviation of the training samples.

$$z = \frac{x-\mu}{s} \quad (1)$$

The model and dataset-specific hyperparameters were tuned during the development of the random forest model. This included the number of trees in the forest, the maximum depth of the trees, the minimum number of samples required at a leaf node and to split an internal node, and the number of features to consider when determining the best split.

To evaluate the model's performance and robustness, the coefficient of determination (R^2) and the Mean Absolute Error (MAE) were used. A higher indicates a better fit between the model and the data, while a lower MAE indicates a smaller difference between the predicted and actual values. Additionally, the model evaluation was repeated 30 times, and the average and MAE were recorded as the results.

7) Determining the Final Classification

The proposed system produces two possible classifications: 'Normal' and 'Abnormal'. 'Normal' indicates that the shrimp is not subject to weight-increasing fraud, while 'Abnormal' signals the detection of an anomaly in the shrimp's weight.

To determine the final classification, the system integrates recognized digits from the 7-segment digit recognition module with the predicted shrimp weight generated by the weight prediction model. If the variation between these two numbers does not exceed 10% of the average weight in the dataset (1.816 grams), the system classifies the shrimp as 'Normal'. Conversely, if the variation exceeds 10%, the shrimp is classified as 'Abnormal'.

IV. Experiment Setup

Three experiments were set up to align with the proposed method described in the previous section. These experiments are detailed in the following subsections.

1) Generate a Shrimp Mask Image

The shrimp mask images, as illustrated in Fig. 10 (a), were generated using the instance segmentation model proposed in subsection 2. 4. The corresponding shrimp dataset, depicted in Fig. 10 (b), was then divided into training, validation, and testing sets with a ratio of 70:20:10. To further enhance the diversity of the training set, data augmentation was applied using the random flip technique.

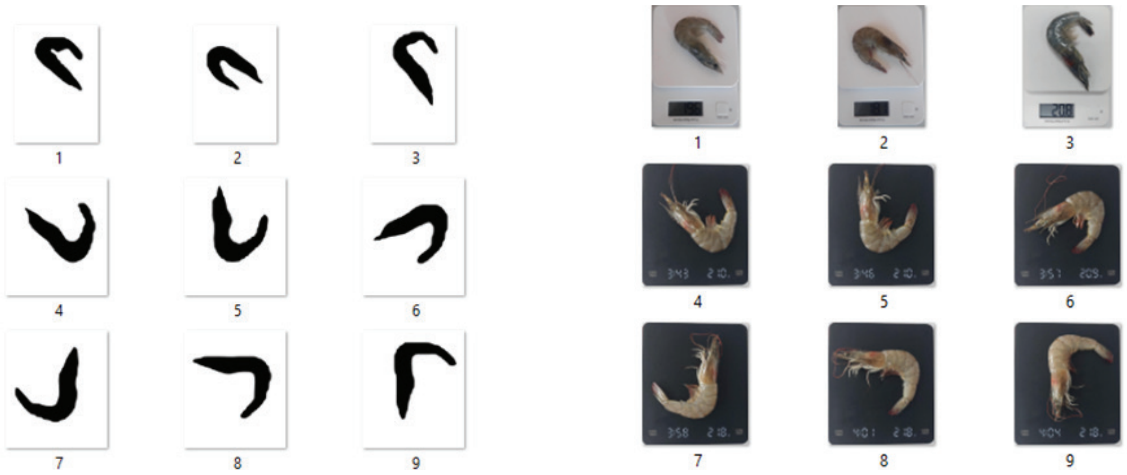

Fig. 10. The comparison of: (a) shrimp mask images obtained from the instance segmentation model, (b) shrimp images captured from a mobile application

A pre-trained ResNet-50 model was utilized as the backbone for development. The model was trained for 12 epochs using the SGD optimizer, with a learning rate of 0.0025, a momentum of 0.9, and a weight decay factor of 0.0001. The evaluation results, reported using CocoMetric, include a segmentation mean Average Precision (mAP) of 0.601 at IoU thresholds ranging from 0.5 to 0.95 in increments of 0.05, and a segmentation mean Average Recall (mAR) of 0.648 at the same IoU thresholds.

2) Feature Analysis And Visualization

The extracted features from the proposed method were analyzed using descriptive statistics, as shown in Table I, to summarize the dataset. This analysis provides insights into the central tendency and variability of each variable. Due to differences in units between the dependent variable (weight), measured in grams, and the independent variables, measured in pixels, a log scale transformation was applied to all variables. The results were visualized using a box-and-whisker plot, as shown in Fig. 11, to better illustrate variability. The plot reveals that "Weight" exhibits high variance, with "Area" displaying the highest variance among the independent variables. Additionally, the other independent variables also demonstrate significant variability.

TABLE I
DESCRIPTIVE STATISTICS OF THE COLLECTED DATASET

Variable (Unit)	Range (max-min)	Mean	S.D.
Area (pixels)	2220	1864.872	426.384
Perimeter (pixels)	177	287.461	33.311
Length (pixels)	72	115.739	13.323
Width (pixels)	24	19.076	3.122
Weight (grams)	25.5	18.160	5.357

This analysis suggests that the selected variables are well-suited for regression model development, as high variance in both independent and dependent variables improves the model's ability to effectively capture diverse patterns and relationships within the data [40], [41].

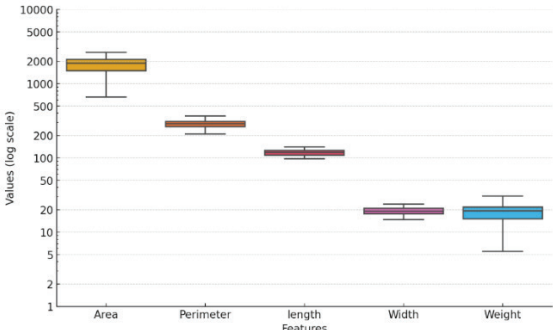

Fig. 11. Log-scaled box-and-whisker plot of variables in the dataset

Additionally, the scatterplot matrix and correlation coefficients, as illustrated in Fig. 12 and Fig. 13, were visualized to understand the strength of the relationships between the independent variables and the dependent variable. This analysis aids in the model and feature selection process by identifying which variables are most relevant for predicting the target outcome.

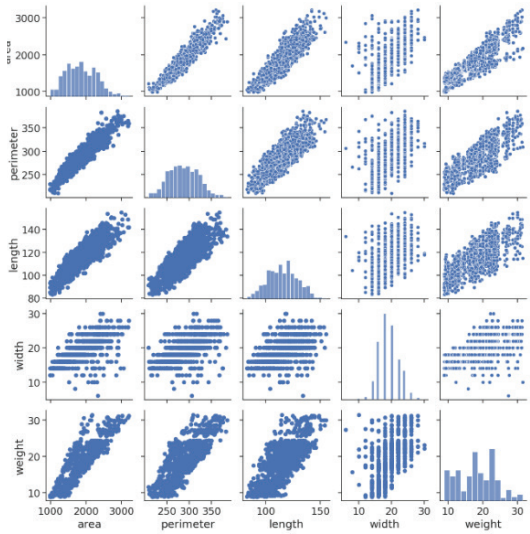

Fig. 12. Scatterplot matrix of variables in the shrimp dataset

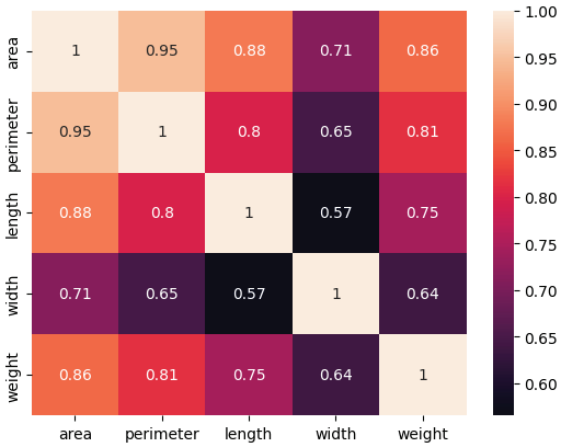

Fig. 13. Correlation coefficient heat map of the extracted shrimp features

3) Weight Prediction Model Training

This experiment focuses on the model and feature selection process. Both linear and non-linear algorithms were explored based on the patterns observed between the independent and dependent variables. Initially, a linear regression algorithm was employed to develop a weight prediction model using shrimp area, as this feature exhibited the highest correlation coefficient with the dependent variable. The dataset was divided into training and testing sets, with 80% used for training and 20% for testing, to evaluate model performance. The experimental results showed that shrimp weight can be predicted using (2), where y denotes the predicted weight and *area* represents the number of black pixels in the shrimp mask image. The model evaluation yielded a R^2 value of 0.777 and an MAE of 2.021.

$$y = -1.9634 + 0.0108 \times area \quad (2)$$

As the performance of the initial linear model was unsatisfactory, a multiple linear regression model was developed. To avoid multicollinearity, the correlation coefficients in Fig. 13 were used for feature selection, with a correlation threshold set at 0.8 [42]. This process led to the selection of shrimp area and shrimp width as features. The resulting model is presented in (3), where y represents the predicted weight, *area* refers to the number of black pixels in the shrimp mask image, and *width* denotes the diameter of the largest circle that fits within the shrimp mask. The model evaluation yielded an R^2 value of 0.779 and an MAE of 2.01.

$$y = -2.4994 + (0.0105 \times area) + (0.0569 \times width) \quad (3)$$

The two linear models developed earlier were still unsatisfactory. Therefore, an ensemble model, specifically a Random Forest, was employed. This model was developed using GridSearchCV to perform an exhaustive search through a specified hyperparameter grid, as shown in Table II.

Additionally, 10-fold cross-validation was applied during this process to improve the model's generalization.

TABLE II
SPECIFIED HYPERPARAMETERS

Hyperparameter	Value	Purpose
n_estimators	300	To specify the number of trees in the forest, which can improve model accuracy.
max_depth	5	To specify the maximum depth of each tree, which can prevent model overfitting.
min_samples_leaf	5	To specify the minimum number of samples required to be at a leaf node, which can improve the model's generalization.
min_samples_split	1%	To specify the minimum fraction of samples required to split an internal node, which can prevent model overfitting.
max_features	Square Root	To specify the number of features considered at each split as the square root of the total number of features, which can help reduce model variance.

V. RESULTS

1) *Weight Prediction Model*

The proposed model in this study was developed using Random Forest Regression and trained on the collected shrimp dataset, with 80% of the data used for training and 20% reserved for model evaluation. The training phase included hyperparameter tuning and 10-fold cross-validation to improve generalization. To enhance the reliability of the results, the evaluation process was repeated 30 times, and the average performance metrics were recorded. The evaluation results for the weight prediction model are presented in Table III.

The results indicate that the weight prediction model developed using random forest best fits the observed data, as reflected by the value. Additionally, the average magnitude of the errors, represented by the MAE, is the lowest among the compared algorithms.

TABLE III
WEIGHT PREDICTION MODELS PERFORMANCE

Regression Model	Feature	R^2	MAE
Linear	Area	0.777	2.021
Multiple Linear	Area & Width	0.779	2.010
Random Forest	All Features	0.821	1.786

2) *Mobile Application*

Upon opening the developed application, users can create their accounts or log in using third-party authentication. On the home page, users can view summarized information, including recommendations on places to buy shrimp and a pie chart illustrating the proportion of normal and abnormal shrimp weights they have predicted. To predict shrimp weight, users can select the Camera menu from the drawer menu in the top left corner of the screen. The application will then display images of various digital weighing scales, allowing users to select the one that matches their own. Subsequently, the mobile camera is activated, and a small green square appears to manually specify the location of the 7-segment display. The mentioned features of the application are illustrated in Fig. 14 (a)-(c).

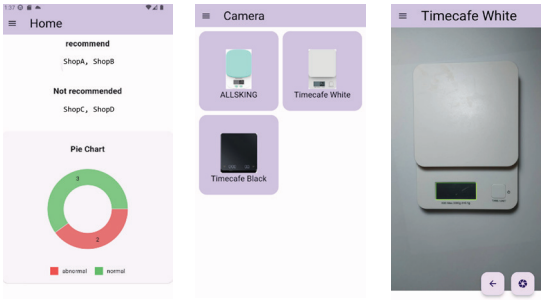

(a) (b) (c)

Fig. 14. The developed mobile application: (a) Home page, (b) Camera page, and (c) Green square on 7-segment display

To detect anomalies in shrimp weight, the user must place the suspicious shrimp on a digital weighing scale while simultaneously capturing an image. Then, they press the prediction button to send the entire image to the API server. If the predicted weight does not differ from the weight displayed on the 7-segment display by more than two grams, the system classifies the shrimp as 'Normal', and the result shown in Fig. 15 (a) will be displayed to the user. Otherwise, Fig. 15 (b) will be shown, indicating an 'Abnormal' classification. Moreover, a prediction history is provided within the developed application, as shown in Fig. 15 (c), to help users identify which stores are safe for purchasing shrimp.

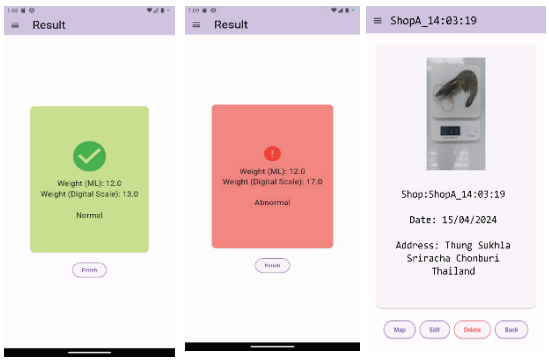

(a) (b) (c)

Fig. 15. The developed system: (a) Normal shrimp weight result, (b) Abnormal shrimp weight result, (c) Shrimp weight prediction history

To verify the developed application, both a non-adulterated shrimp detection scenario and an adulterated shrimp detection scenario were tested. In the first scenario, a non-adulterated shrimp, with an actual weight of 24.2 grams, was placed on a digital weighing scale. The developed mobile application captured an image of the shrimp, which was then sent to the API server. The server generated a shrimp mask, extracted all morphological features, predicted the weight from the obtained features, and determined the final classification. The feedback from the API server was 'Normal', indicating that the developed system successfully passed this test.

In the second scenario, an adulterant weighing 3.3 grams was injected into the same shrimp used in the first scenario, resulting in a total weight of 27.5 grams. The testing process was identical to the first scenario. However, the result from the API server was 'Abnormal', indicating that the developed system also successfully passed this test.

VI. Discussion

The experimental results show that the Random Forest Regression algorithm, utilizing all extracted features, significantly outperformed both linear and multiple linear regression models within the scope of this experiment's dataset. This superior performance comes from the ensemble approach of Random Forests, where the predicted weight is an aggregation of numerous decision trees. Each tree is constructed using feature randomness and the bagging ensemble learning technique, which enhances the model's robustness. Additionally, the diverse conditions under which the individual trees are created contribute to the model's ability to generalize effectively. The final prediction, being an average of all tree outputs, results in a more reliable and generalized weight prediction model. It's worth noting that the success of the Random Forest model is due not only to the algorithm itself but also to the careful selection of relevant features, which played a crucial role in optimizing model performance.

The mobile application for detecting anomalies in shrimp weight was developed using the Dart programming language. It interfaces with image processing and weight prediction components through APIs implemented in Python. Python was chosen for image processing because it's more efficient than Dart for those tasks. While machine learning models could be deployed directly on mobile devices, APIs were used for the weight prediction component to ensure consistent performance. This server-side approach guarantees uniform model accuracy, regardless of users' varying hardware capabilities, making the system more reliable and scalable. Furthermore, the application's features are specifically designed to detect undeclared product modifications that increase the perceived weight of shrimp. This information is valuable for consumers, helping them avoid buying from sources previously associated with adulterated shrimp.

VII. Conclusion and Future Work

This research aimed to develop a practical approach for individuals seeking to avoid shrimp weight fraud. The proposed method focuses on daily usability and feasibility. Recognizing the pervasive use of mobile devices and their synergy with AI, a mobile application was developed as the user interface for the anomaly detection module. This module ingeniously combines an instance segmentation model with a weight prediction model.

The system identifies weight anomalies through sophisticated image analysis. It starts by accurately segmenting shrimp from their background using Mask R-CNN, chosen for its excellent object segmentation capabilities. This method proved highly precise and efficient, yielding clear shrimp outlines crucial for the developed application.

After segmentation, vital morphological features, including area, perimeter, length, and width, were extracted. While area and perimeter were simple to calculate, determining length and width demanded more complex, computationally intensive methods. To address this, a shortest path algorithm and a circle-fitting method with reduced point frequency were implemented, allowing for efficient extraction of the necessary numerical data.

These extracted features are then fed into the shrimp weight prediction model. Experimental results show that the model, built with the Random Forest algorithm and leveraging all four features (area, perimeter, length, and width), significantly outperformed other models. It achieved an value of 0.821 and a Mean Absolute Error (MAE) of 1.786 grams, successfully meeting the proposed system's criteria.

However, this research could be further improved by developing an automated 7-segment screen detector. This improvement would allow the system to adapt to a wider variety of weighing scales, greatly increasing its flexibility and real-life applicability.

Acknowledgments

This research received no external funding. The original contributions presented in the study are included in the article; further inquiries can be directed to the corresponding author on reasonable request. The authors would like to thank the Faculty of Engineering at Sriracha, Kasetsart University, for providing the facilities for experimentation. The authors declare no conflicts of interest.

REFERENCES

[1] H. Zhang and F. Gui, "The application and research of new digital technology in marine aquaculture," *J. Mar. Sci. Eng.*, vol. 11, no. 2, p. 401, Feb. 2023.

[2] S. A. Jasmin, P. Ramesh, and M. Tanveer, "An intelligent framework for prediction and forecasting of dissolved oxygen level and biofloc amount in a shrimp culture system using machine learning techniques," *Expert Syst. Appl.*, vol. 199, p. 117160, Aug. 2022.

[3] A. Steinkruger et al., "Seafood traceability program design: Examination of the United States' Seafood Import Monitoring Program," *Ambio*, vol. 54, no. 2, pp. 168-174, Feb. 2025, https://doi.org/10.1007/s13280-024-02075-8

[4] L. C. Navarro, A. Azevedo, A. Matos, A. Rocha, and R. Ozório, "Predicting weight dispersion in seabass aquaculture using discrete event system simulation and machine learning modeling," *Aquac. Rep.*, vol. 38, p. 102315, Oct. 2024.

[5] L. Chen, X. Yang, C. Sun, Y. Wang, D. Xu, and C. Zhou, "Feed intake prediction model for group fish using the MEA-BP neural network in intensive aquaculture," *Inf. Process. Agric.*, vol. 7, no. 2, pp. 261-271, Jun. 2020.

[6] N. Chirdchoo, S. Mukviboonchai, and W. Cheunta, "A deep learning model for estimating body weight of live Pacific white shrimp in a clay pond shrimp aquaculture," *Intell. Syst. Appl.*, vol. 24, p. 200434, Dec. 2024.

[7] X. Chen, I. N' Doye, F. Aljehani, and T. M. Laleg-Kirati, "Fish weight prediction using empirical and data-driven models in aquaculture systems," in *Proc. 2024 IEEE Conf. Control Technol. Appl. (CCTA)*, 2024, pp. 369-374.

[8] Y. Jin, L. Meng, and T. Shi, "An effective feature learning approach using genetic programming for crab age classification," *Fish. Res.*, vol. 281, p. 107197, Jan. 2025.

[9] J. H. Qu, J. H. Cheng, D. W. Sun, H. Pu, Q. J. Wang, and J. Ma, "Discrimination of shelled shrimp (Metapenaeus ensis) among fresh, frozen-thawed and cold-stored by hyperspectral imaging technique," *LWT-Food Sci. Technol.*, vol. 62, no. 1, pp. 202-209, Jun. 2015.

[10] Z. Liu, M. Huang, Q. Zhu, J. Qin, and M. S. Kim, "Nondestructive freshness evaluation of intact prawns (Fenneropenaeus Chinensis) using line-scan spatially offset Raman spectroscopy," *Food Control*, vol. 126, p. 108054, Aug. 2021.

[11] T. Valeeprakhon, K. Orkphol, and P. Chaihuadjaroen, "Deep convolutional neural networks based on VGG-16 transfer learning for abnormalities peeled shrimp classification," *Int. Sci. J. Eng. Technol. (ISJET)*, vol. 6, no. 2, pp. 13-23, Dec. 2022.

[12] D. A. Willette, K. Andrade, B. Fitzpatrick, and K. Wilson, "Outreach & DNA-based monitoring facilitate 3-fold reduction in seafood mislabeling in Los Angeles over 10 years," *Food Control*, vol. 168, p. 110913, Feb. 2024.

[13] L. Peruzza et al., "Preventing illegal seafood trade using machine-learning assisted microbiome analysis," *BMC Biol.*, vol. 22, no. 1, p. 202, Sep. 2024, https://doi.org/10.1186/s12915-024-02005-w

[14] E. Basdeki and T. N. Tsironi, "Novel packaging technologies for shrimp and shrimp products," in *Postharvest Technologies and Quality Control of Shrimp, Amsterdam*, NL: Elsevier, 2025, pp. 295-321.

[15] S. de la Puente and V. Christensen, "Linking catch reconstructions with downstream supply chain nodes can help strengthen management actions in favour of just, sustainable and resilient futures," *Mar. Policy*, vol. 170, p. 106387, Sep. 2024.

[16] L. Lorusso et al., "Mismanagement and poor transparency in the European processed seafood supply revealed by DNA metabarcoding," *Food Res. Int.*, vol. 194, p. 114901, Oct. 2024.

[17] W. Woraprayote, C. Kongsawat, and W. Visessanguan, "Safety and regulation of different food additives for shrimp and shrimp products: Comprehensive analysis in Thailand," in *Postharvest Technologies and Quality Control of Shrimp*, Amsterdam, NL: Elsevier, 2025, ch. 12, pp. 323-346.

[18] M. Fox, M. Mitchell, M. Dean, C. Elliott, and K. Campbell, "The seafood supply chain from a fraudulent perspective," *Food Secur.*, vol. 10, no. 4, pp. 939-963, Aug. 2018, https://doi.org/10.1007/s12571-018-0826-z

[19] M. C. Rivers, A. B. Campbell, C. H. Lee, P. Kapoor, and R. S. Hellberg, "Short-weighting, species authentication, and labeling compliance of prepackaged frozen shrimp sold in grocery stores in Southern California," *Food Control*, vol. 155, p. 110101, Jan. 2024.

[20] P. Ganapathiraju, T. J. Pitcher, and G. Mantha, "Estimates of illegal and unreported seafood imports to Japan," *Mar. Policy*, vol. 108, p. 103439, Oct. 2019.

[21] I. O. Owolabi and J. A. Olayinka, "Incidence of fraud and adulterations in ASEAN food/feed exports: A 20-year analysis of RASFF's notifications," *PLoS One*, vol. 16, no. 11, p. e0259298, Nov. 2021.

[22] M. O. Balaban, S. Yeralan, and Y. Bergmann, "Determination of count and uniformity ratio of shrimp by machine vision," *J. Aquat. Food Prod. Technol.*, vol. 3, no. 3, pp. 43-58, May. 1995.

[23] D. A. Luzuriaga, M. O. Balaban, and S. Yeralan, "Analysis of visual quality attributes of white shrimp by machine vision," *J. Food Sci.*, vol. 62, no. 1, pp. 113-118, Jan. 1997, https://doi.org/10.1111/j.13652621.1997.tb04379.x

[24] P. Pan, J. Li, G. Lv, H. Yang, S. Zhu, and J. Lou, "Prediction of shelled shrimp weight by machine vision," *J. Zhejiang Univ. Sci. B*, vol. 10, pp. 589-594, Aug. 2009.

[25] H. Mubarak, Z. Zainuddin, and M. Niswar, "Pixel-based weight estimation of Vannamei shrimp using digital image processing: A solution for precise feeding management in aquaculture," in *Proc. 2023 Int. Seminar Intell. Technol. Appl. (ISITIA)*, 2023, pp. 115-118.

[26] M. Spreitzenbarth, T. Schreck, F. Echtler, D. Arp, and J. Hoffmann, "Mobile-sandbox: Combining static and dynamic analysis with machine-learning techniques," *Int. J. Inf. Secur.*, vol. 14, no. 2, pp. 141-153, Apr. 2015, https://doi.org/10.1007/s10207-014-0250-0

[27] M. Lathkar, "Getting started with FastAPI," in *High-Performance Web Apps with FastAPI, Berkeley*, CA: Apress, 2023, pp. 29-64. [Online]. Available: https://doi.org/10.1007/978-1-4842-9178-8_2

[28] Z. Chen et al., "An empirical study on deployment faults of deep learning-based mobile applications," in *Proc. 2021 IEEE/ACM 43rd Int. Conf. Softw. Eng. (ICSE)*, 2021, pp. 674-685.

[29] S. Patil et al., "Enhancing optical character recognition on images with mixed text using semantic segmentation," *J. Sens. Actuator Netw.*, vol. 11, no. 4, p. 63, Oct. 2022.

[30] A. Spreafico, F. Chiabrando, L. Teppati Losè, and F. G. Tonolo, "The iPad Pro built-in LiDAR sensor: 3D rapid mapping tests and quality assessment," *Int. Arch. Photogramm. Remote Sens. Spat. Inf. Sci.*, vol. 43, pp. 63-69, Jun. 2021.

[31] K. Chen et al., "MMDetection: Open MMLab detection toolbox and benchmark," *arXiv*, 2019. [Online]. Available: https://arxiv.org/abs/1906.07155 [Accessed: Dec. 15, 2024].

[32] X. Yu, J. Wang, S. Wen, J. Yang, and F. Zhang, "A deep learning based feature extraction method on hyperspectral images for nondestructive prediction of TVB-N content in Pacific white shrimp (Litopenaeus Vannamei)," *Biosyst. Eng.*, vol. 178, pp. 244-255, Feb. 2019.

[33] M. Sun, X. Yang, and Y. Xie, "Deep learning in aquaculture: A review," *J. Comput.*, vol. 31, no. 1, pp. 294-319, Jan. 2020, https://doi.org/10.3966/199115992020023101028

[34] W. K. Mutlag, S. K. Ali, Z. M. Aydam, and B. H. Taher, "Feature extraction methods: A review," *J. Phys. Conf. Ser.*, vol. 1591, no. 1, p. 012028, Jul. 2020, https://doi.org/10.1088/1742-6596/1591/1/012028

[35] Z. Liu, X. Jia, and X. Xu, "Study of shrimp recognition methods using smart networks," *Comput. Electron. Agric.*, vol. 165, p. 104926, 2019.
[36] A. Saleh, M. M. Hasan, H. W. Raadsma, M. S. Khatkar, D. R. Jerry, and M. R. Azghadi, "Prawn morphometrics and weight estimation from images using deep learning for landmark localization," *Aquac. Eng.*, vol. 106, p. 102391, Oct. 2024.
[37] I. D. Mienye and Y. Sun, "A survey of ensemble learning: Concepts, algorithms, applications, and prospects," *IEEE Access*, vol. 10, pp. 99129-99149, Oct. 2022.
[38] D. E. P. Moghaddam, A. Muguli, M. Razavi, and B. Aazhang, "A graph-based cardiac arrhythmia classification methodology using one-lead ECG recordings," *Intell. Syst. Appl.*, vol. 22, p. 200385, Jun. 2024.
[39] T. Khater, H. Tawfik, and B. Singh, "Explainable Artificial Intelligence for investigating the effect of lifestyle factors on obesity," *Intell. Syst. Appl.*, vol. 23, p. 200427, Sep. 2024.
[40] X. Yang, Y. Wang, W. Yan, and J. Li, "Variance estimation based on blocked 3×2 cross-validation in high-dimensional linear regression," *J. Appl. Stat.*, vol. 48, no. 11, pp. 1934-1947, Aug. 2021, https://doi.org/10.1080/02664763.2020.1780571
[41] Y. Fujikoshi and T. Sakurai, "High-dimensional consistencies of KOO methods for the selection of variables in multivariate linear regression models with covariance structures," *Mathematics*, vol. 11, no. 3, p. 671, Jan. 2023.
[42] J. H. Kim, "Multicollinearity and misleading statistical results," *Korean J. Anesthesiol.*, vol. 72, no. 6, pp. 558-569, Jul. 2019.

Kanjana Eiamsaard is an Assistant Professor in the Department of Computer Engineering, Faculty of Engineering at Sriracha, Kasetsart University Sriracha Campus, Thailand. She received an M.S. in Software Engineering from Chulalongkorn University, Thailand. Her research interests include Artificial Intelligence, machine learning, and software engineering.

Kathawach Satianpakiranakorn is a lecturer in the Department of Computer Engineering, Faculty of Engineering at Sriracha, Kasetsart University Sriracha Campus, Thailand. He received M.Eng. in Computer Applied Technology from Harbin Engineering University, P.R. Harbin, China. His research field includes Artificial Intelligence, Computer Vision, and Digital Image Processing.

Anan Banharnsakun is an Associate Professor in the Department of Computer Engineering, Faculty of Engineering at Sriracha, Kasetsart University Sriracha Campus, Thailand. He received a Ph.D. degree in Electrical and Computer Engineering from King Mongkut's University of Technology Thonburi (KMUTT),Thailand. His research interests include biologically inspired computational intelligence, robust optimization, pattern recognition, and high-performance computing.

Jirawat Jitprasutwit is a lecturer in the Department of Computer Engineering, Faculty of Engineering at Sriracha, Kasetsart University Sriracha Campus, Thailand. He received an M.Eng. in Electrical Engineering from Mahidol University, Thailand His research interests include Artificial Intelligence, Internet of Things, embedded systems , and smart intelligent systems.

Low-Cost Digitization for Monitoring Manual Processes: A Case Study of Tray Cleaning in Semiconductor Manufacturing

Pathitta Timtong[1], Pornnapat Kwanboonya[2], and Warut Pannakkong[3*]
[1,2,3]School of Manufacturing Systems and Mechanical Engineering,
Sirindhorn International Institute of Technology, Thammasat University,
Pathum Thani, Thailand
E-mail: pathitta.tim@gmail.com, pornnapatkwanboonya@gmail.com, warut@siit.tu.ac.th*

Received: April 17, 2025 / Revised: September 30, 2025 /Accepted: October 10, 2025

***Abstract*—The increasing global adoption of Industry 4.0 technologies has transformed many aspects of manufacturing through automation, data analytics, and smart systems. However, high implementation costs often prevent labor-intensive processes, particularly in developing regions and smaller enterprises, from realizing these benefits. This study addresses that gap by proposing a low-cost digitization solution focused on tray cleaning in semiconductor manufacturing, a critical yet manually executed process. In collaboration with Sony Device Technology Thailand, an Excel VBA-based application was developed to automate real-time recording of tray movements and manpower data. The system incorporates inventory tracking, productivity monitoring, and an interactive dashboard that enhances operational visibility and eliminates the need for manual checks. Quantitative evaluation revealed a 50% reduction in input processing time and a 74.07% decrease in output processing time per transaction. Qualitative improvements include increased cross-functional collaboration, more transparent workforce evaluation, and data-driven decision-making. This study contributes a scalable, practical model for affordable digitization that integrates seamlessly with existing workflows, offering an effective path toward digital transformation in labor-intensive manufacturing environments.**

***Index Terms*—Industry 4.0, Digitization, Excel VBA-based Application, Data Visualization, Semiconductor Manufacturing**

I. Introduction

The rapid evolution of the Fourth Industrial Revolution is reshaping manufacturing industries worldwide. Smart factories, intelligent inventory systems, and automated supply chains are becoming the standard, driven by advancements in artificial intelligence, machine learning, and data analytics [1]. At the core of this transformation lies digitization—the process of converting analog operations into digital formats to enhance efficiency and decision-making [2]. However, while large-scale digitization projects offer significant benefits, the high implementation costs pose a challenge.

In manufacturing, data is a fundamental requirement for process optimization. Every company needs reliable, real-time data to enhance efficiency, minimize waste, and optimize operations [3]. Despite the growing adoption of Industry 4.0, not every manufacturing step can be fully automated. Some processes, particularly those involving human operators, remain difficult to digitize using automated sensor-based tracking systems due to cost constraints. This gap highlights the need for practical, low-cost digitization solutions that can integrate with existing workflows without requiring substantial financial investment [4].

The semiconductor industry, a critical driver of modern technology, is a prime example of this challenge. Semiconductors power everything from smartphones to advanced computing systems, making their production efficiency crucial to meeting global demand [1]. In Thailand, the semiconductor sector is expanding rapidly, supported by increased investments aimed at enhancing production capacity and operational efficiency. Tray cleaning is a critical but often underappreciated process in semiconductor manufacturing, as it plays a key role in handling and protecting delicate wafers during transport and storage. Clean trays help prevent contamination, maintain yield quality, and reduce production loss, especially in high-volume production environments.

However, despite its importance, tray cleaning operations remain heavily reliant on manual labor, primarily due to the complexity of the task and the high cost of automation [2]. As a result, this process often lacks digital monitoring and is excluded from

broader Industry 4.0 initiatives, even among large manufacturers. Ensuring accurate data recording and real-time monitoring for these operations at a low cost is vital for improving efficiency without disrupting existing workflows.

This paper presents a case study on low-cost digitization in semiconductor manufacturing, focusing on tray cleaning operations. By collaborating with Sony Device Technology Thailand, this research develops an Excel VBA-based application that enables real-time data recording and visualization of manpower and inventory movement. This approach provides an affordable alternative to high-cost automation systems, allowing manufacturers to enhance process tracking and decision-making without significant infrastructure changes.

To sum up, this study highlights the potential of low-cost digitization as a practical solution for bridging the gap between manual operations and Industry 4.0. By leveraging simple yet effective digital tools, manufacturers can optimize their processes, improve inventory management, and enhance operational efficiency with minimal investment. As industries continue to evolve, accessible digitization strategies will play a crucial role in ensuring sustainable growth and competitiveness in the global market.

II. Objective

This research develops an Excel VBA-based data collection tool to track manpower, automate productivity calculations, enable real-time data monitoring for informed decision-making, and reduce redundant manual verification processes.

III. Related Work

Industry 4.0 has significantly reshaped manufacturing with automation, AI, and IoT, offering advanced solutions to optimize operations. These innovations, including smart factories and automated supply chains, have greatly enhanced operational efficiency in developed economies [1], [2]. However, the high costs of automation pose significant challenges for small enterprises and developing nations. While automation benefits large-scale operations, many industries in emerging economies, including Thailand, continue to rely on manual labor due to the prohibitive costs associated with full automation [3], [4].

In sectors like semiconductor manufacturing, tasks such as tray cleaning remain heavily manual due to the complexity and high costs of automating these processes [2]. Despite the growth of Industry 4.0, there is a notable gap in providing affordable digitization solutions for industries that still rely on manual workflows. Most existing research focuses on high-tech automation tools, leaving small-scale manual operations largely overlooked [4]. This gap underscores the need for practical, low-cost alternatives that can seamlessly integrate with existing manual processes, making digitization accessible even for companies with limited financial resources.

The importance of low-cost digitization tools is further emphasized by the need for affordable alternatives in sectors that still rely heavily on manual labor, as highlighted by studies on semiconductor industries [5] and logistics management [6]. Existing research has also indicated that high financial costs, capital-intensive spending, and lack of incentives are among the most critical barriers across multiple industries when adopting new technological or circular models [7]. In parallel, cost-effectiveness has been identified as a decisive factor in other technological domains, such as renewable energy transitions, where improving efficiency and lowering Levelized Costs is essential for widespread adoption [8]. By leveraging Excel VBA applications, this paper demonstrates how businesses can achieve significant improvements in efficiency and accuracy without requiring large capital investments typically associated with high-tech solutions [9].

In addition to optimizing manual workflows, the integration of simple digital tools plays a key role in the digital transformation of small-scale operations, particularly within Thailand's manufacturing sector, where many businesses still rely on human labor [10]. This project highlights the potential impact of affordable digital solutions that bridge the gap between manual labor and Industry 4.0, providing businesses with the chance to enhance their competitiveness on a global scale without bearing the heavy financial burden of traditional automation systems [11]. The solution developed in this project has already been applied in the real semiconductor industry, demonstrating its practical value in enhancing operational efficiency and improving tracking systems without requiring costly automation. In summary, by introducing an accessible, scalable solution to improve manual operations, this paper contributes to the broader effort of modernizing industries in developing economies. The proposed solution could significantly enhance operational efficiency in smaller, labor-intensive operations, positioning them to better compete in an increasingly digital global marketplace. Moreover, this solution has already been successfully implemented in the real semiconductor industry, demonstrating its practical value in optimizing workflows and improving operational tracking in a real-world setting.

IV. Methodology

This section comprises two main parts: the generalized concept of a proposed system and a case study.

A. Proposed System

The proposed system, illustrated in Fig. 1, is designed to achieve three key objectives: recording tray movement, tracking manpower, and providing a real-time dashboard for comprehensive monitoring. The system is intended to manage the cleaning and storage processes within a designated room, where trays undergo a series of operations, including counting, inspection, cleaning, and if necessary, repair. The movement of each tray through these stages is systematically recorded in the application, ensuring that every action is logged for accuracy and traceability. Additionally, workers are required to input their manpower details at each stage, enabling the system to track the allocation of human resources alongside the physical movement of trays. Upon completion of all tasks, a real-time dashboard is provided to offer an integrated view of both tray and worker activities, ensuring full visibility into the operational process. This dashboard enables real-time monitoring, allowing managers to oversee the status of trays and workers, and thus enhancing efficiency and accountability. The system's design is adaptable, making it applicable to various industries that require the management of assets and labor, ensuring seamless integration into different workflows. By capturing and presenting data in an accessible format, this system offers potential for broad implementation, contributing to the optimization of operational processes across various sectors.

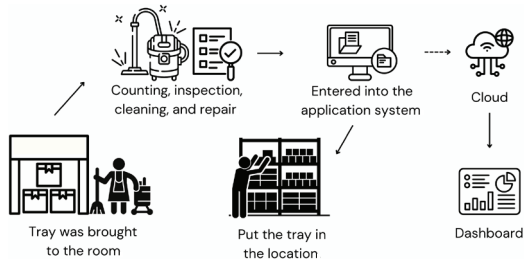

Fig. 1. Tray management process flow

B. Case Study

In this case study, the application was developed in collaboration with Sony Device Technology Thailand following interviews to identify inefficiencies in the manual tray tracking process. Through iterative prototyping and user feedback, a low-cost Excel-based system was developed and deployed in the tray cleaning area, as shown in Fig. 2. The tool integrates VBA and PivotTables to support real-time recording of manpower and inventory with minimal disruption to existing workflows.

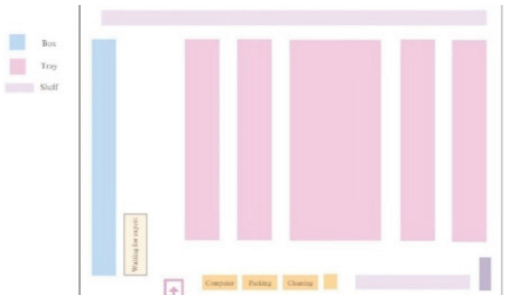

Fig. 2. Tray storage and workflow room layout example

1) Database

The database design was guided by an iterative development process rather than a technical specification. First, requirements were gathered through short interviews with operators and supervisors, which revealed frequent errors in manual logging of operator IDs and tray details. Based on these findings, two simple databases were designed: one for operator information (numeric ID and name) and another for tray information (tray ID, name, pieces per pack, business unit, and location).

Prototype versions were then tested with actual barcode scans in the workplace. User feedback highlighted the need for automatic validation and additional fields, such as tray location. These refinements were incorporated into the final design. The resulting databases thus reflect both technical considerations and user-driven adjustments, ensuring accuracy and ease of adoption.

2) Recording Tray Movement (Tray Inventory)

This feature was developed using a VBA-based user form to enable structured and consistent recording of tray quantities and related operational data. Upon entering key identifiers, such as part code and operator ID, the system performs input validation against the existing database and retrieves relevant information as shown in Fig. 3. Users then input the total quantity, after which the system automatically computes the number of packs and any remainder using the formulas: Pack Quantity = Total Quantity / Pack Size and Remainder = Total Quantity mod Pack Size. To reflect operational contexts, users can also select the appropriate transaction type. The interface and logic were refined through iterative feedback from operators, with particular attention to usability and error reduction as shown in Fig. 4.

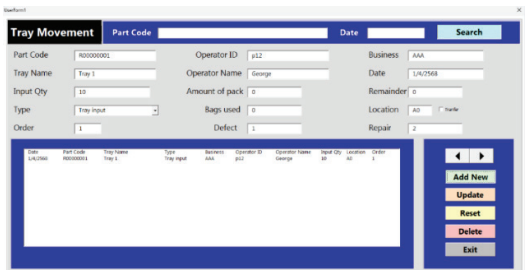

Fig. 3. The recording tray movement system

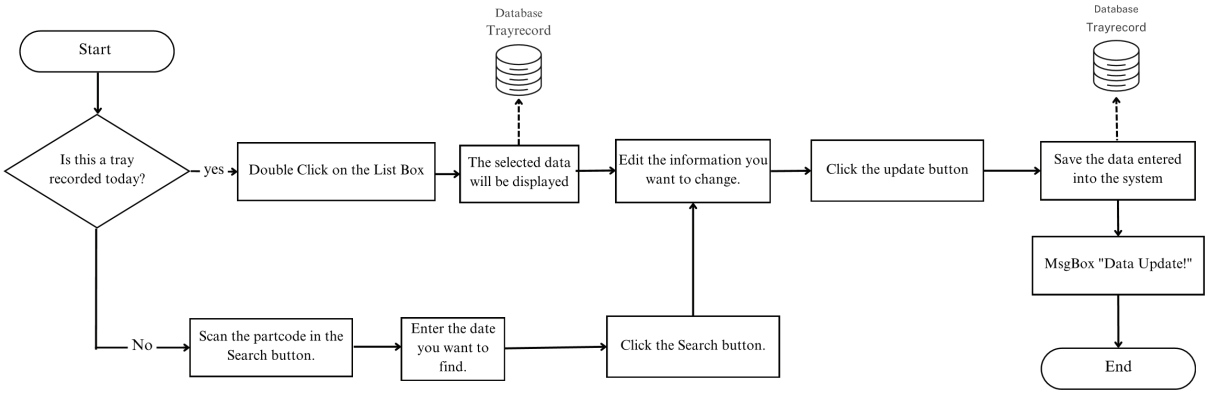

Fig. 4. The recording tray movement process chart

3) Recording Manpower

This feature, developed using Microsoft Excel VBA, offers an efficient system for tracking manpower and evaluating productivity. When the user clicks the "Manpower Record" button, a userform prompts them to input the necessary information, as shown in Fig. 5. The system then validates and processes the inputs according to the steps outlined in Fig. 6, ensuring that only accurate data—such as text, numbers, and dates—is saved to the manpower file. The application automatically records the time spent on each task. The recorded data is subsequently analyzed to monitor manpower usage, assess workloads, and improve productivity through automated task duration calculations. Productivity is determined using the formula: Productivity = units of output/ labor hours worked.

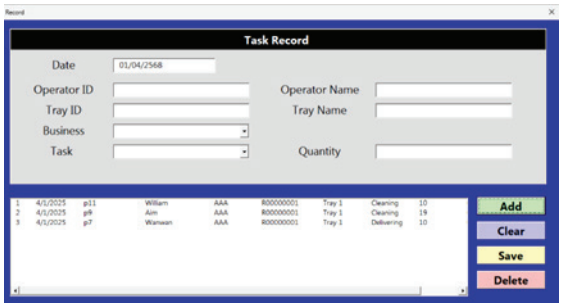

Fig. 5. The recording manpower system

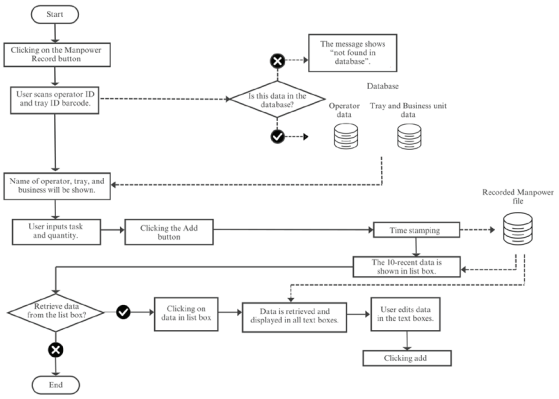

Fig. 6. Manpower record process chart

4) Dashboard Analyzation

To analyze the recorded data, the system retrieves both the manpower and tray quantity files and imports them into the main file. The command then generates an Excel PivotTable as an analysis tool to summarize productivity and inventory stock, following the process outlined in the chart, as shown in Fig. 7. To analyze available space, the system applies a weighted-average method since each pallet row does not have a fixed quantity. The analyzed data is then displayed as a percentage, making it easier to support decision-making. The results are displayed as an interactive graph with slicers, enabling managers to sort and filter the data according to their specific needs.

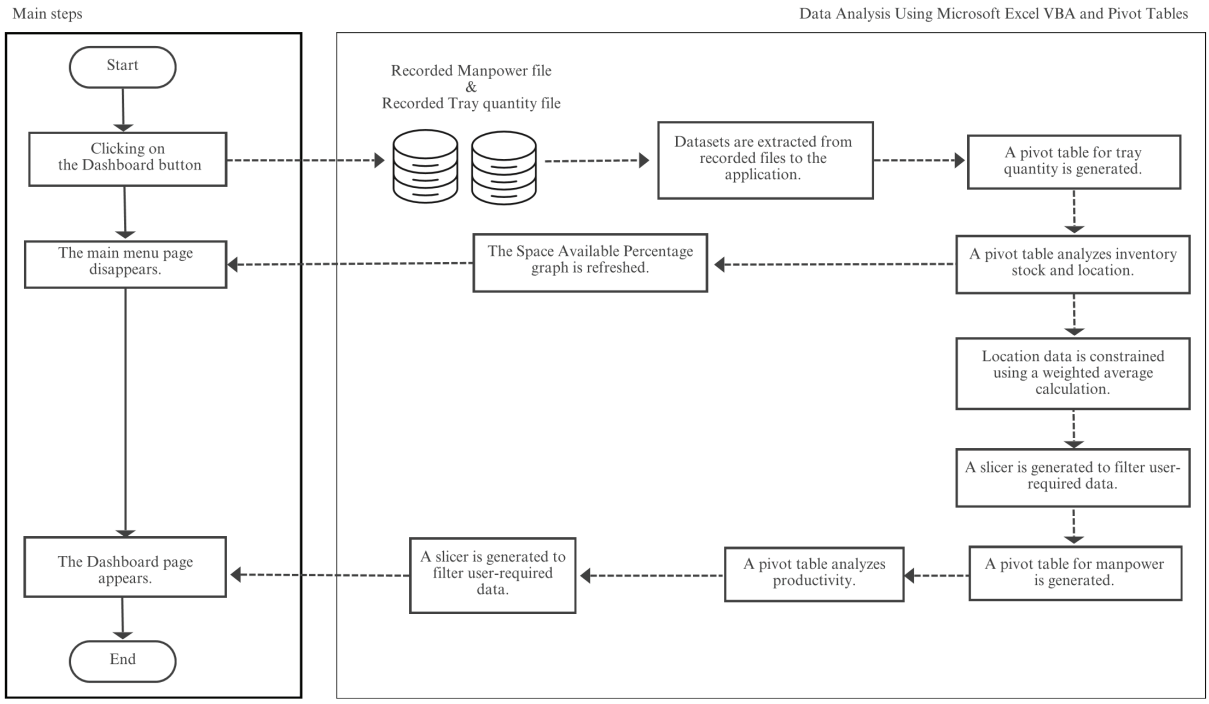

Fig. 7. Dashboard analysis process chart

V. Results and Discussion

For evaluating the performance of the demonstration set, reliability and accuracy have been tested.

A) Real-Time Interactive Monitoring Dashboard

To facilitate data visualization, an interactive dashboard with slicer functionality, as shown in Fig. 8, consolidates essential information on a single page, enabling users to make informed decisions quickly. The dashboard dynamically retrieves and presents data, eliminating the need for up to a week of manual effort previously required to summarize tray quantity and manpower productivity. Operators can now check tray inventory levels on a computer instead of performing manual counts, other departments can access the system in real time, reducing delays from phone inquiries. The dashboard enables managers to summarize tray quantities by month, date, and business unit using the left-hand slicer, and track productivity by month, date, and operator name using the right-hand slicer. The interactive graph separates data into manpower and tray quantity sections. A quick search feature and tray quantity summary further streamline inventory management by providing users with in-stock quantities based on scanned barcodes, improving efficiency in checking, and reducing time spent on counting and searching. It also enhances cross-department collaboration by making information accessible without informal inquiries. Thus, the dashboard reshapes both work habits and communication patterns.

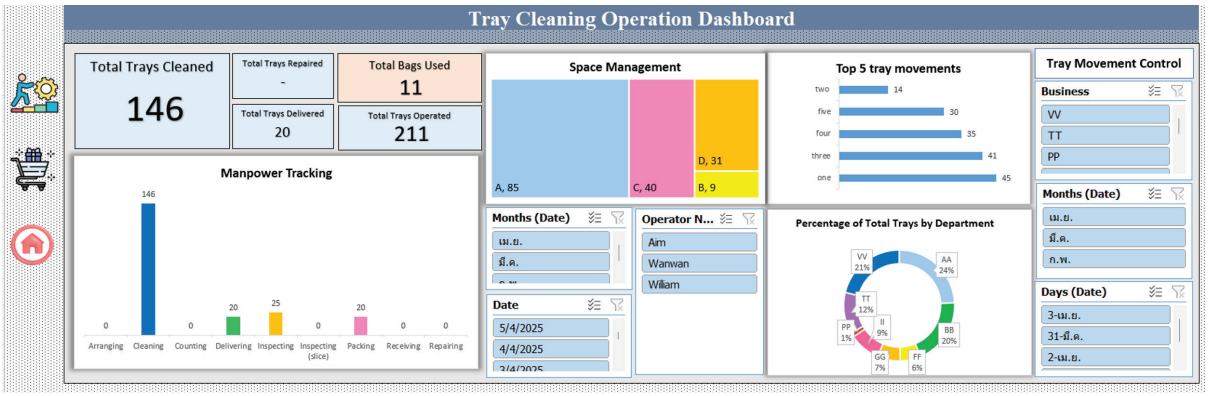

Fig. 8. The Dashboard analysis

B) Evaluation of Time Reduction in the Data Recording Process

The new application enhances efficiency by eliminating redundant tasks such as manual data entry and phone inquiries. With built-in data analysis and a real-time dashboard, it streamlines workflows, reduces errors, and enables faster, more accurate tracking of progress.

When comparing the traditional process and the newly developed process in terms of Input, as shown in Table I, and Output, as shown in Table II, the new process has significantly improved by removing unnecessary steps. In the Input section, the traditional process takes 1 minute and 40 seconds per transaction, while the new process only takes 50 seconds, reducing the time by 50 seconds or 50%. This time reduction is due to direct data entry into the application instead of manual writing and the removal of redundant steps, such as cleaning and arranging, which can now be done more efficiently. In the Output section, the traditional process takes 2 minutes and 15 seconds, whereas the new process only takes 1 minute and 4 seconds, saving 1 minute and 11 seconds or 74.07%. This reduction is achieved by eliminating phone calls for inquiries and enabling instant data entry within the application. These improvements in both sections make the overall process faster and more efficient, significantly reducing transaction time and increasing productivity.

Time savings reduce manual effort and can improve fairness and accountability, yet require employees to adapt to more structured workflows. The process redesign affects routines and staff interactions beyond mere efficiency.

C) Manpower Productivity Monitoring

This system introduces a new approach to track manpower in an area where no previous tracking or recorded data existed. The implemented system fills this gap by recording each operator's start time and task details, enabling accurate productivity assessments, as shown in Table III. Although this analysis uses data from a single operator, it originates from the cleaning data system and serves as a representative example. The system is scalable and can accommodate multiple operators based on each company's size and operational needs.

This data-driven approach replaces verbal reporting with measurable evidence, enabling managers to make informed workforce adjustments to prevent tray shortages, balance workloads, and reduce idle time. By recording detailed manpower data, the system ensures performance evaluations are objective and transparent. This not only enhances operational efficiency but also supports a structured, evidence-based method for managing workforce and inventory in previously untracked areas.

TABLE I
INPUT COMPARISON FOR 1 TRANSACTION

Input	**Present Steps for a Transaction**		
Order	**Activity**	**Action**	**Time/Transaction (avg.)**
1	Tray/Box for Delivery	Recorded Manually	0:00:29
2	Tray Cleaning	Clean, Count, Repair, and Pack	Depending on theAmount of Tray
3	Tray Placement on Shelf	Arranging	0:00:21
4	Data Entry in Traditional Application	Data Entry in Traditional Application	0:00:50
	Total		**0:01:40**

The recorded processing time is expressed in hours, minutes, and seconds (hh:mm:ss).

Input	**Proposed Steps for a Transaction**		
Order	**Activity**	**Action**	**Time/Transaction (avg.)**
1	Tray/Box for Delivery	Clean, Count, Repair, and Pack	Depending on the Amount of Tray
2	Data Entry in New Application	Input Data into the New Application	0:00:29
3	Tray Placement on Shelf	Arranging	0:00:21
	Total		**0:00:50**

The recorded processing time is expressed in hours, minutes, and seconds (hh: mm: ss).

TABLE II
OUTPUT COMPARISON FOR 1 TRANSACTION

Output	Present steps for a transaction		
Order	**Activity**	**Action**	**Time/Transaction (avg.)**
1	Call to Request/Ask	Communicate with Another Department	0:00:56
2	Save initial order data	Manually recorded	0:00:29
3	Retrieve Tray	Pick up the tray from the shelf	Depending on the amount of tray
4	Issues from the Traditional Application	Issues from the Traditional Application	0:00:50
	Total		**0:02:15**

The recorded processing time is expressed in hours, minutes, and seconds (hh: mm: ss).

Output	Proposed steps for a transaction		
Order	**Activity**	**Action**	**Time/Transaction (avg.)**
1	Receive the Report	Check if there is a tray in the Application	0:00:06
2	Retrieve Tray	Clean, Count, Repair, and Pack	Depending on the Amount of Tray
3	The Output Tray from the New Application	The Output Tray from the New Application	0:00:29
	Total		**0:00:35**

The recorded processing time is expressed in hours, minutes, and seconds (hh:mm:ss).

TABLE III
EXAMPLE OF MANPOWER PRODUCTIVITY CALCULATION

No.	Date	ID	Name	Product	Task	Quantity (Piece)	Time Record	Duration (hh: mm: ss)	Productivity (Pieces Per Hour)
1	19/2/2025	R01	Employee 1	Z	Cleaning	50	1:57:33 PM	0:07:42	390
2	19/2/2025	R01	Employee 1	Z	Inspecting	50	2:05:15 PM	0:03:50	783
3	19/2/2025	R01	Employee 1	Z	Packing	50	2:09:05 PM	0:01:29	2022
4	19/2/2025	R01	Employee 1	Z	Arranging	50	2:10:34 PM	0:03:20	900

The recorded processing time is expressed in hours, minutes, and seconds (hh:mm:ss).

VI. CONCLUSION

This study aims to develop a low-cost digitization method for semiconductor manufacturing, focusing on tracking tray movements and recording employee activities. The approach utilizes an Excel VBA-based application, offering a more affordable alternative to expensive automation systems. This method helps record and visualize data related to labor and inventory movements in real-time, without requiring significant changes to the existing infrastructure. The development of the new application reduces the time by 50% in the Input Tray process and 74.07% in the Output Tray process. The proposed system integrates seamlessly with existing processes, allowing manufacturers to track operations and make better decisions. While accuracy improvements in data accuracy are needed, the low-cost digitization approach demonstrates strong potential for enhancing operational efficiency and process monitoring.

VII. FUTURE WORK

Previously, the company relied on manual record-keeping, repeatedly entering data into a computer without the ability to export files for further analysis. With the implementation of this application, data is automatically calculated and recorded in an Excel file. Additionally, the files are retrieved and summarized in a one-page, real-time interactive dashboard. However, due to the coding limitations of Microsoft Excel VBA, the current application lacks flexibility in automatically tracking manpower and updating tray inventory. Privacy concerns within the collaborating company also pose challenges in integrating outsourced cameras. To address these limitations, future improvements should focus on leveraging computer vision and machine learning to automate quantity tracking and manpower productivity monitoring, reducing reliance on manual data entry.

ACKNOWLEDGMENTS

This research is the result of a collaborative effort between the Sirindhorn International Institute of Technology (SIIT) and Sony Device Technology (Thailand) Co., Ltd. The authors would like to express their heartfelt appreciation to Sony Device Technology Thailand for generously providing the case study and valuable industry insights throughout this research.

SSRN Electronic Journal

REFERENCES

[1] M. Ghobakhloo, "Industry 4.0, digitization, and opportunities for sustainability," *J. Clean. Prod.*, vol. 252, p. 119869, Apr. 2020, https://doi.org/10.1016/j.jclepro.2019.119869

[2] P. Jha, "Digitization and Industry 4.0 practices: An exploratory study on SMEs in India," *SSRN*, 2021. [Online]. Available: https://doi.org/10.2139/ssrm.3846755 [Access: May 17,2025].

[3] L. Han, H. Hou, Z. M. Bi, J. Yang, and X. Zheng, "Functional requirements and supply chain digitalization in Industry 4.0," *Inf. Syst. Front.*, vol. 25, no. 5, pp. 1713-1727, 2023, https://doi.org/10.1007/s10796-021-10173-1

[4] S. Yang, A. M. Riza, J. Kaminski, and H. Pepin, "Opportunities for Industry 4.0 to support remanufacturing," *Appl. Sci.*, vol. 8, no. 7, p. 1177, Jul. 2018, https://doi.org/10.3390/app8071177

[5] X. Zhang, Y. Zhang, and G. Li, "Strategic inventory in semiconductor supply chains under industrial disruption," *Int. J. Prod. Econ.*, vol. 272(c), p. 109254, Apr. 2024, https://doi.org/10.1016/j.ijpe.2024.109254

[6] C. Jiang, "Integrating the use of spreadsheet software and VBA in inventory simulation," *J. Softw.*, vol. 5, no. 5, pp. 498-505, May. 2010. https://doi.org/10.4304/jsw.5.5.498-505

[7] D. M. Utama, I. Amallynda, R. W. Wardana, T. Y. Rosiani, R. Anggriani, and D. S. Wijaya, "A new hybrid fuzzy decision model for barrier identification and strategy prioritization in circular rice supply chains: A case study in Indonesia," *Indon. J. Sci. Techol.*, vol. 11, no. 2, pp. 293-320, Sep. 2026, https://doi.org/10.17509/ijost.v11i2.89788

[8] Y. Chen, H. Bai, "Techno-Economic and technical analysis of ammonia-based hydrogen and power routes in China," *Renewable Energy*, vol. 235, pp. 112-125, Jan. 2026, https://doi.org/10.1016/j.renene.2025.124269

[9] D. Amalfitano, V. De Simone, A. R. Fasolino, and P. Tramontana, "EXACT: A tool for comprehending VBA-based Excel spreadsheet applications," *J. Softw. Evol. Process*, vol. 28, no. 6, pp. 483-505, Apr. 2016, https://doi.org/10.1002/smr.1787

[10] T.-T. Wong and Y.-J. Chen, "An association analysis of high-price inventory items for semiconductor industry," *Asia Pac. Manag. Rev.*, vol. 30, no. 2, p. 100348, Dec. 2024, https://doi.org/10.1016/j.apmrv.2024.100348

[11] P. Kanjanarut and W. Pannakkong, "A low-cost IIoT-enabled computer vision-based system for classifying defect types and severity levels in Industry 4.0," *Int. Sci. J. Eng. Technol. (ISJET)*, vol. 7, no. 2, pp. 1-10, Nov. 2023.

[12] P. Na Lamphun, P. Khogkhaluang, and A. Kheaksong, "Increasing performance through information retrieval system for design and build company," *Int. Sci. J. Eng. Technol. (ISJET)*, vol. 5, no. 1, pp. 32-40, Jun. 2021.

[13] P. Jaisue and P. Siri-O-Ran, "Time reduction in picking the product: A case study of roof tile warehouse," *Int. Sci. J. Eng. Technol. (ISJET)*, vol. 7, no. 2, pp. 53-58, Dec. 2023.

[14] V. Mingmankong, C. Jeenanunta, R. Chaysiri, and Y. Ueki, "Key success factors for implementing Industry 4.0 of Thailand manufacturing," *Int. Sci. J. Eng. Technol. (ISJET)*, vol. 7, no. 2, pp. 42-52, Dec. 2023.

Pathitta Timtong is currently a fourth-year student, pursuing a Bachelor of Engineering in Industrial Engineering and Logistics Systems at Sirindhorn International Institute of Technology (SIIT), Thammasat University, Thailand. Her research interests encompass supply chain management, data analysis, digital transformation, Industry 4.0, and Data Visualization.

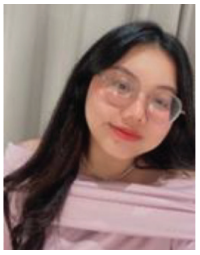

Pornnapat Kwanboonya is currently a fourth-year student, pursuing a Bachelor of Engineering in Industrial Engineering and Logistics Systems at Sirindhorn International Institute of Technology, Thammasat University, Thailand. Her research interests encompass supply chain management, data analysis, digital transformation, Industry 4.0, and Data Visualization.

Warut Pannakkong received his B.Eng. in Industrial Engineering and M.Eng. in Logistics and Supply Chain Systems Engineering, both from Sirindhorn International Institute of Technology (SIIT), Thammasat University, Thailand, in 2010 and 2014, respectively. He earned his Ph.D. in Knowledge Science from the Japan Advanced Institute of Science and Technology (JAIST) in 2017. Currently, he is an Associate Professor in the School of Manufacturing Systems and Mechanical Engineering at SIIT and serves as the Deputy Director for International Affairs and Corporate Relations at SIIT. He is also a managing editor of the International Journal of Knowledge and Systems Science. His research interests include artificial intelligence for industry, time series forecasting, sustainable supply chain management, data mining, machine learning, computer vision for industrial applications, and discrete event system simulation and optimization.

Optimizing Tricycle (Tuk-Tuk) Suspension Systems Using Mathematical Modeling

Chaiyawoot Narintharangkul[1*] and Poom Jatunitanont[2]
[1,2]Faculty of Engineering and Technology, Panyapiwat Institute of Management, Nonthaburi, Thailand
E-mail: chaiyawootnar@pim.ac.th*, poomjat@pim.ac.th

Received: February 13, 2025 / Revised: May 20, 2025 / Accepted: May 28, 2025

***Abstract*—The use of tricycles in Thailand has declined due to mechanical issues, particularly with the engine and suspension systems. This research focuses on optimizing the suspension system to improve ride comfort. The study has three main objectives: 1) to analyze the vibration of the leaf spring suspension in two-section convertible tricycles, 2) to develop a suspension model that complies with ISO 2631-1 standards for vibration comfort, and 3) to compare vibration effects between the original and new suspension models using simulation software. The goal is to reduce vibrations and enhance comfort through mathematical modeling and parameter optimization. FFT and PSD analyses identified dominant vibration frequencies in the 4 to 8 Hz range, which correspond to human body resonance. By applying a band-stop filter and optimizing spring stiffness and damping coefficient, the damping ratio was adjusted to 0.3. This led to a significant reduction in RMS acceleration from 0.985 m/s² to 0.537 m/s², and peak acceleration dropped from 1.12 m/s² to 0.582 m/s², improving comfort from fairly uncomfortable to slightly uncomfortable.**

The optimized suspension design significantly reduced vibrations in critical frequency ranges. The results from this approach can be applied to various vehicle types, offering potential for further development in the automotive industry, especially for vehicles sensitive to vibration.

***Index Terms*—Tricycle, Suspension System, Vibration, Comfort Value, Computer Program**

I. Introduction

The Tuk-Tuk, officially known as the Tricycle, was first produced in 1948 by Piaggio Ape, an Italian company also known for manufacturing Vespa. The tricycle produced at that time had a top speed of 30 miles per hour. Since then, the Tuk-Tuk has been introduced and gained popularity in many countries across Asia. It was first manufactured in Asia in 1957 when Japan began selling three-wheeled trucks.

The Daihatsu Midget DK is a two-stroke motorcycle (ZA 250cc) with a single headlight and motorcycle-like handling. Shortly thereafter, this tricycle model was imported to Thailand for the first time in 1960 to replace pedal tricycles that were banned in Bangkok. Initially, the Japanese tricycles were modified with a roof for passenger safety and to close the access on the right side. Originally, there were two access points for passengers, but later, this was changed to only one for safety reasons.

Initially, there were many brands of tricycles, but today, only a few remain. Thus, the tricycle has been a long-standing symbol of Thailand. According to the Automobile Act No. 18, 2019, tricycles can be divided into two types: personal tricycles (Ror-Yor. 4) and three-wheeled taxis (Ror-Yor. 8). A survey conducted as of July 31, 2022, found that there was a total of 20,207 three-wheeled vehicles in use across the country, including both personal tricycles and three-wheeled taxis, which is fewer than the 20,484 vehicles registered as of December 31, 2021. This decrease is attributed to the non-approval of vehicle registration due to failing inspection according to the Department of Land Transport's regulations [1].

Inside the tricycle, there are systems similar to those found in general cars, which can be divided into six categories: engine system, transmission system, steering system, braking system, electrical system, and suspension system. Currently, tricycle owners in Thailand focus on enhancing engine performance to increase speed and power. However, this focus may impact the engine's lifespan and contribute to air pollution due to black smoke from increased engine performance. Comparative studies between Thai and foreign tricycles reveal that tricycles abroad emphasize passenger comfort, focusing more on the suspension system than on other systems. The main function of the suspension system is to dampen vibrations between the road surface and the vehicle to improve road grip. If the suspension is inadequate, hitting a bump can disrupt the vehicle's balance and potentially affect passengers.

The suspension system of Thai tricycles is designed with a rigid beam and leaf springs, which

have both advantages and disadvantages. This system often faces problems, such as excessive weight under the springs, which affects vehicle control at high speeds and on rough roads. Without proper maintenance and with overloading, the leaf spring suspension is more suitable for carrying goods than passengers. This is because the force from the suspension is directly transmitted to the vehicle frame, causing passengers to feel the impact as well.

In today's rapidly advancing automotive world, every system in all types of vehicles is continuously evolving. Changes in engine systems, from internal combustion engines to electric engines, and improvements in suspension systems are significant. Analyzing and developing components or creating new ones to enhance user or passenger comfort and driving smoothness is crucial. This aligns with research by Jaisaard, research conducted a comparative study of ride quality between the EMU-A1 and EMU-B1 trains on the BTS Sukhumvit Line from stations N8 to E14. Although the study encompasses various measurements, testing was not conducted on different types of road surfaces.

This study investigates the design, analysis, and improvement of the suspension system for Thai tricycles to enhance ride comfort, vibration isolation, and load-bearing capacity. Using mathematical modeling and simulation, the research provides a robust framework for evaluating suspension performance. The findings support the development of Thai tricycles to meet international standards and competitiveness. Moreover, the insights gained apply to a wide range of vehicles such as motorcycles, trucks, and buses, offering potential benefits in both commercial and industrial applications through improved damping and vibration control.

A. Objectives of Research

- Research and analyze the vibrations of the leaf spring suspension in two-section convertible tricycles currently in use.
- To develop a model that complies with the ISO 2361-1 standard, the design and layout of the new tricycle suspension ensure standard vibration comfort.
- To compare the vibration effect of the model of the old and new undercarriage parts of the tricycle that received vibration through a computer program.

B. Research Hypothesis

- Tricycles are used by Thai citizens and international visitors in daily life for travel or transportation.
- Passenger comfort in riding in a tricycle with the original suspension is less comfortable than the new suspension.
- The vibration of the new suspension can be used better in traffic.

C. Scope of Research

- This study investigated the vibration of the plate spring suspension of the current model tricycle. This is a two-stage convertible tricycle.
- Study by modeling old and new tricycle suspensions in various ways to analyze the vibration of the suspension of tricycles currently in use according to ISO 2361-1.
- Analyze the suspension model of the currently in-use convertible tricycle in 1D and compare the effect of vibration using a computer program.

D. Benefits

- Increase the efficiency of the suspension system of the tricycle to absorb vibration better than before
- The improved suspension design can be applied to other forms of tricycles.
- Can promote and attract the use of tricycles.
- Can be used to extend the business of tricycles.

E. Definition

- Tricycle means a Tuk-Tuk or a tricycle that is hired to carry passengers with a two-part convertible.
- The suspension system refers to the components of the vehicle below all. Which is the part that supports the entire weight of the car?
- Simulation software is used to solve and analyze the data.

II. Literature Review

A. Suspension

A vehicle's suspension system is designed to absorb and minimize vibrations generated by contact with the road surface. Positioned between the car's frame, body, engine, transmission, and wheels, the suspension ensures that road irregularities do not disrupt the vehicle's smooth operation. Its primary function is to dampen the impact of vibrations from tire-road interactions, preventing excessive transmission of these vibrations into the cabin. Beyond this, the suspension system plays a crucial role in maintaining the vehicle's stability, ensuring proper body alignment, and keeping the tire tread perpendicular to the road surface, even during turns. It also helps to control excessive bouncing, reduce unwanted movements, and maintain balance, particularly when navigating uneven terrain or during rapid acceleration and braking [2].

B. Vibration

The vibration of an object relies on Newton's law of motion, as shown in (1) (Newton's law of motion), to find the differential equation of motion.

$$\sum F = m\vec{\ddot{x}}(t) \quad (1)$$

Newton's second law equation is that the sum of the applied force $\sum \vec{F}(t)$ is equal to the mass m times the acceleration, where the variable x(t) is the vibrational distance $\dot{x}(t)$. The vibration velocity, and x(t) is the acceleration of the vibration, which are variables that can change over time. Therefore, the value of the vibration distance that occurs in the system will be a value that can change over time when an external force acts. The vibration problem consists of three main components: the spring constant. The weight of the mass and the damping constant by the spring constant are used to store the potential energy of the system. The force generated by the extension or contraction of the spring can be calculated from (2) [3].

$$F_k = kx(t) \quad (2)$$

Where k is the spring constant in N⁄m and x(t) is the extension of the spring in meters, which is a time-varying value by which the force of the spring is used to pull or push the mass back. Ideally, if the system does not have a device for extracting the energy of the vibration, the mass of the system will vibrate without stopping, so the final component of the A damper is a damper that is used to extract the potential energy from the spring from the system to stop the vibration. The force generated by the damper device can be shown as (3).

$$F_c = c\dot{x}(t) \quad (3)$$

Where c is the damper constant in and $\dot{x}(t)$ is the mass vibration velocity in m/s. Used to reduce vibrations that occur in the system [4].

The vehicle suspension system, as shown in Fig. 1, is an illustration of the suspension system of one side of a wheel, which has all 3 vibration components. In mathematical modeling, the mass of the vehicle frame is given by the variable m_s, and the mass of the car wheels with tires is given by the variable m_u, which is in kg. The mass of the vehicle frame accounts for only one quarter of the total vehicle weight, as represented in the Quarter Car model. Spring component is used to simulate the elasticity of a spring at suspension, which is defined as k_s variable and used to simulate the elasticity of a tire, which uses the k_u variable to simulate the tire section, and the c_s variable is used to simulate the damper. That is in the lower area, in which to create a mathematical model, a diagram of the forces occurring in the system must be drawn (free-body diagram), where the variable x (t) is the vibration distance in the vertical mass of the vehicle frame. The variable y (t) is the vertical vibration distance of the vehicle wheels, and the variable z(t) is the level of the road the vehicle travels on. These three variables are time-varying. Forces arising in the spring and damping elements between the vibration stages x(t) and y(t) or y(t) and z(t) are due to the difference in the vibration stages of the masses. The frame and wheel mass for the spring force and the resulting difference in the velocity of the vibration of the frame and wheel mass for the damper element, respectively.

In the simulation, the car will run on a flat road or value *z(t) = 0* where z is the road level used to simulate the car on a flat road, and the value *z(t) > 0* represents the car driving on different roads. As a result, vibrations are generated at the mass of the car frame and wheels, with the suspension comprising spring elements and dampers working together to reduce the level of vibration, as shown in Fig. 1 [5].

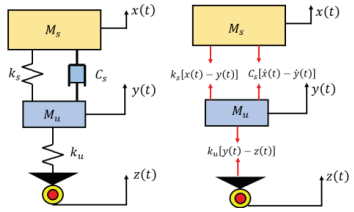

Fig. 1. Mathematical modeling of automotive suspension systems

To find a mathematical model, it relies on Newton's second law to find the equation of motion by analyzing the mass of the car frame, m_s, and the mass of the car wheel m_u, which can be calculated. The motion in terms of second-order differential equations (4) and (5) is obtained respectively from Newton's second law, which determines the direction of vibration of the mass of the frame m_s. And the mass of the wheel m_u is positive when both masses are moving upward.

$$\ddot{x} = -[(k_s/M_s)x(t)]+[(k_s/M_s)y(t)] - [(C_s/M_s)\dot{x}(t)]+[(C_s/M_s)\dot{y}(t)] \quad (4)$$

$$\ddot{y}(t) = [(k_s/M_u)x(t)]-[(k_s/M_u)y(t)]+ [(C_s/M_u)\dot{x}(t)]-[(C_s/M_u)\dot{y}(t)]- [(k_u/M_u)y(t)]+[(k_u/M_u)z(t)] \quad (5)$$

Equations (4) and (5) can be written in state-space form as (6).

$$\dot{\vec{x}}(t) = [A]\vec{x}(t)+[B]\vec{u}(t) \quad (6)$$

Where $\dot{\vec{x}}(t)$ is the velocity vector, $\dot{\vec{x}}(t)$ is the position vector, and the variable $\vec{u}(t)$ is the incoming signal vector or road level z(t), where the matrix [A] is the system matrix and matrix [B] is the input matrix, since the left side of (6) is the order derivative velocity vector. Therefore, to write (4) and (5) in terms of first derivatives as shown in (6), one of the variables to reduce the power of the derivative from second order to first order by setting the variable as shown in (7).

$$x_1(t) = x(t) \quad (7)$$

Equation (7), the variable from is the vibration distance of the vehicle frame. x(t), then defines the

variable , as shown in (8).

$$x_2(t) = \dot{x}_1(t) = \dot{x}(t) \quad (8)$$

From (8), the variable $x_2(t)$ is the vibration velocity of the car frame $\dot{x}(t)$, so $\dot{x}_2(t)$ is equal to $\ddot{x}(t)$ or the acceleration of the car frame. Set the variable $x_3(t)$ as shown in (9) and the variable $x_4(t)$ to be the first derivative of the variable $x_3(t)$ as shown in (10).

$$x_3(t) = y(t) \quad (9)$$

$$x_4(t) = \dot{x}_3(t) = \dot{y}(t) \quad (10)$$

From defining variables, it can be found that $x_3(t)$ is the vibration distance of the car wheels, and the variable $x_4(t)$ is the speed of the vibration of the car wheels. Therefore, if using the variable $x_4(t)$ to get the first derivative, Equation (11), which is equal to the acceleration of the wheels of the car.

$$\dot{x}_4(t) = \ddot{x}_3(t) = \ddot{y}(t) \quad (11)$$

By defining a new variable to reduce the order of the differential equations, (4) and (5) can be written in terms of spatial equations as shown in (6). Equation (6) is rewritten in the form of (12).

$$\begin{bmatrix} \dot{x}_1(t) \\ \dot{x}_2(t) \\ \dot{x}_3(t) \\ \dot{x}_4(t) \end{bmatrix} = \begin{bmatrix} 0 & 1 & 0 & 0 \\ -k_s/M_s & -C_s/M_s & k_s/M_s & C_s/M_s \\ 0 & 0 & 0 & 1 \\ k_s/M_u & C_s/M_u & -\left(\frac{k_s}{M_u}+\frac{k_u}{M_u}\right) & -C_s/M_u \end{bmatrix} \begin{bmatrix} x_1(t) \\ x_2(t) \\ x_3(t) \\ x_4(t) \end{bmatrix} + \begin{bmatrix} 0 \\ 0 \\ 0 \\ k_u/M_u \end{bmatrix} z(t) \quad (12)$$

when the variable

$x_1(t)$ is the vibration distance of the chassis in m.

$x_2(t)$ is the vibration velocity of the chassis in m/s.

$x_3(t)$ is the vibration distance of the wheel in m.

$x_4(t)$ is the speed of vibration of the wheels in m/s.

The spatial equation of state (12) will be used to simulate the vibration effects occurring in the vehicle suspension system as the vehicle travels across different surfaces, using the variables in matrices [A] and [B]. These variables will remain constant throughout the vibrations occurring in the car suspension system.

C. Assessment of Driving Comfort According to ISO 2631-1

Humans respond at different frequencies. Therefore, the ISO 2631-1 standard has a different value of the weighting factor at each frequency. The scope of content in ISO 2631-1 indicates methods for measuring the different types of visual vibrations entering human subjects. Whether sitting, standing, or lying down, this is found in driving vehicles. Mechanization or in a residential area, and tell them to calculate the indicator, indicating the level of vibration that can be tolerated. In terms of health, comfort, perception, or nausea, humans could perceive each frequency differently. Therefore, there is a weight to be calculated for each frequency as well. This value is called frequency weightings, which consists of W_k, W_d, W_f, W_c, W_e, W_j, which are used depending on the axis of the vibration according to ISO 2631-1, which is used to assess the acceleration of the passenger. In a sitting position, in case the force is exerted from under the seat, for example, the relationship between the weighting factor *(W)* and the frequency in the case of a passenger's sitting position will be used to weigh the acceleration of the support spring mass after converting to a signal in the frequency domain [6]. The effectiveness of the total acceleration can be expressed as the following equation.

$$A_w = [\sum (W_i A_i)^2]^{1/2}$$

The total effective acceleration values can be used to assess driving comfort according to the recommended criteria as follows.

1. When less than 0.315 m/s^2 is not an uncomfortable level.
2. When between 0.315 m/s^2 - 0.63 m/s^2, it feels a bit uncomfortable.
3. When between 0.5 m/s^2 - 1 m/s^2, it feels fairly uncomfortable.
4. When between 0.8 m/s^2 - 1.6 m/s^2, it feels uncomfortable.
5. When between 1.25 m/s^2 - 2.5 m/s^2, it feels very uncomfortable.
6. When more than 2 m/s^2 is at an extremely uncomfortable level.

D. Vibration Measuring Device

- Arduino Board

Arduino is a small AVR microcontroller board that serves as a processor and controller, making this device ideal for studying and learning about microcontroller systems. The board can control a wide range of input/output devices, either independently or in conjunction with other devices, such as PCs. This is possible because Arduino supports connection to various digital and analog input/output devices, including receiving data from switches or sensors and controlling output devices like LEDs, motors, relays, and more. An Arduino hardware system can be created and assembled by the user, who should have some basic knowledge of electronics, or pre-made circuit boards can be purchased, available at affordable prices [7].

- Vibration Sensor

A vibration sensor is an instrument designed to measure the magnitude and frequency of vibrations within a system, machine, or piece of equipment. These measurements are utilized to identify imbalances or other potential issues within the asset, aiding in the prediction of future failures. A vibration sensor can be directly connected to the asset or monitored wirelessly. Once installed, the sensor detects vibrations from the

asset through various methods, depending on the type of sensor employed. Over time, the device generates two types of data: frequency and intensity [8].

In the research, the basic system variables will be determined. Variable values can be determined as shown in Table I. The values of the variables are based on research of Ceyhanli [9] for being the default variable value in simulating the vibration of the car suspension. The characteristics of the leaf spring car suspension determine the durability and stretch of the leaf springs.

TABLE I
VALUES OF THE TRICYCLE SUSPENSION MODEL

Variable	Result	Unit
k_1	479.92	N/m
k_2	509.6	N/m
J_0	140.073	Kg-m^2
d_1	0.64	m
d_2	0.64	m
M	350	kg

The K value of the spring (Spring Rate) is the softness of the spring that will collapse in proportion to the weight of the vehicle pressed down onto the spring coil. The value has been measured using a measuring tool to find out the value. The tool used is a spring stiffness meter. The values that can be measured are k_1 = 479.92 N/m and k_2 = 509.6 N/m, as mentioned in the table above.

Fig. 2. Shock Spring hardness measuring tool

The Shock Spring Hardness Measuring Tool is specialized equipment engineered and manufactured in accordance with national standards for spring tension and compression testing machines. It is designed for testing various properties of springs, including tensile strength, pressure, displacement, deformation, hardness, and free height. In the context of experimental methodology, research experiments are conducted using a system of mathematical equations to derive the results. The experimental process is divided into three distinct phases by the researcher.

III. METHODOLOGY

A. Mathematical Calculation

The researcher has developed a Free Body Diagram (FBD) illustrating the forces acting on the suspension system of the tricycle, comprehensively depicting all the forces involved. This diagram was then compared with the tricycle used as a sample in the study. Furthermore, the researcher employed an engineering drawing program to create a detailed design, thereby enhancing the visualization of the three-wheeled suspension system's components. This method also contributes to a more precise and clearer understanding of the operational principles of the suspension system.

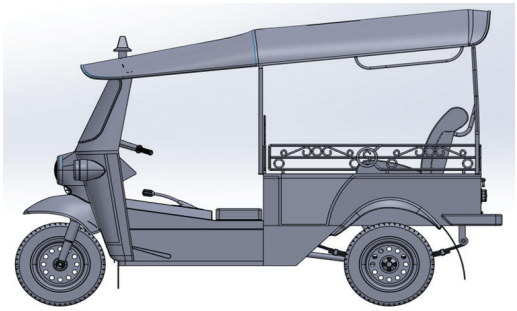

Fig. 3. Model of a tricycle through an engineering drawing program

Free Body Diagram of a tricycle can be categorized into two types: one depicting the tricycle's vibration up and down, and another representing the tricycle's motion while turning right or left. The researcher identified a problem during turning and focused on developing a free-body diagram for the tricycle while it was turning. This scenario can also be compared to the effect of a vehicle falling into a hole.

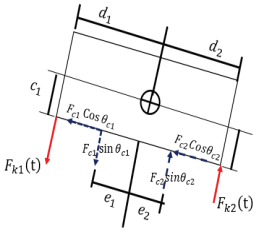

Fig. 4. Free-body diagram occurs while the tricycle makes a turn.

The equations of motion of a two-degree-of-freedom (Equation of Motion) system can be written as a system of equations using knowledge of algebra. Matrices and vectors can help with writing equations as follows [10].

$$[m]\ddot{\vec{x}}(t)+[c]\dot{\vec{x}}(t)+[k]\vec{x}(t)=\vec{F}(t) \quad (13)$$

Therefore, the final matrix equation used to calculate this mathematical equation of the tricycle will be as follows.

$$\begin{pmatrix} -m\omega^2+k_1+k_2 & -k_1d_1+k_2d_2 \\ -k_1d_1+k_2d_2 & -J_0\omega^2+k_1d_1^2+k_2d_2^2 \end{pmatrix} \begin{Bmatrix} X \\ \Theta \end{Bmatrix} = \begin{Bmatrix} 0 \\ 0 \end{Bmatrix} \quad (14)$$

By the method of finding the value of the matrix equation after substituting the values X and $\Theta \neq 0$, the equation can be found using the Determinant method. This method is a function that gives the result as a scalar quantity. Which depends on the value of n in the n×n dimension of the square matrix. From the Determinant method, the equation will be obtained ω^4 and ω^2 in the form of an equation with the values of and in the equation. Arrange the form ω^2 of the equation so that, in the form ω^2 of the equation, both the equation and when reformatting it stay in the equation. The entire equation must then be assigned the variable $\lambda=\omega^2$ to the equation, and the roots of the equation that has been specified can be found. Obtained by using the Quadratic Formula equation.

$$a\lambda^2+b\lambda+c=0 \rightarrow -b\pm\sqrt{b^2+4ac}/2a \quad (15)$$

After knowing the values of ω_1 and ω_2, find the values of $X^{(1)}$ and $\Theta^{(1)}$ by substituting ω_1 into the equation and find the values of $X^{(2)}$ and $\Theta^{(2)}$ by substituting ω_2 into the equation as well. When the results of the variable values are obtained, determine the ratio of the maximum amplitudes of ω_1 and ω_2 as follows

$$r_1 = \Theta^{(1)} / X^{(1)} \quad (16)$$

$$r_2 = \Theta^{(2)} / X^{(2)} \quad (17)$$

After that, solve the equation using the Mode Shapes Vector principle to find the values $\vec{x}^{(1)}$ and $\vec{x}^{(2)}$ by substituting the values in the equation from the values r_1 and r_2 using the following equation.

$$\vec{X}^{(1)} = \begin{Bmatrix} 1 \\ r_1 \end{Bmatrix} X^{(1)} \quad (18)$$

$$\vec{X}^{(2)} = \begin{Bmatrix} 1 \\ r_2 \end{Bmatrix} X^{(2)} \quad (19)$$

Therefore, to substitute the equation to find a vibration diagram of the suspension system, it must occur at a certain time. The equation used must, therefore, be as follows.

$$\vec{X}^{(1)}(t) = \begin{Bmatrix} X^{(1)}(t) \\ \theta^{(1)}(t) \end{Bmatrix} = \begin{Bmatrix} 1 \\ r_1 \end{Bmatrix} X^{(1)} \cos(\omega_1 t+\emptyset_1) \quad (20)$$

$$\vec{X}^{(2)}(t) = \begin{Bmatrix} X^{(2)}(t) \\ \theta^{(2)}(t) \end{Bmatrix} = \begin{Bmatrix} 1 \\ r_2 \end{Bmatrix} X^{(2)} \cos(\omega_2 t+\emptyset_2) \quad (21)$$

Equations (20) and (21) mentioned above are First Mode and Second Mode equations, respectively, as mentioned above. After that, substitute the obtained equation with the solution equation into (3) [11]. The solution equation can be written as

$$X_1(t) = X_1 \cos(\omega t+\emptyset) \quad (22)$$

$$\dot{X}_1(t) = -X_1 \sin(\omega t+\emptyset)d/dt(\omega t+\emptyset) \quad (23)$$

$$\ddot{X}_1(t) = -X_1 \omega\cos(\omega t+\emptyset)d/dt(\omega t+\emptyset) \quad (24)$$

$$X_2(t) = X_2 \cos(\omega t+\emptyset) \quad (25)$$

$$\dot{X}_2(t) = -X_2 \sin(\omega t+\emptyset)d/dt(\omega t+\emptyset) \quad (26)$$

$$\ddot{X}_2(t) = -X_2 \omega\cos(\omega t+\emptyset)d/dt(\omega t+\emptyset) \quad (27)$$

When the solution equation has been successfully substituted into variables $X(t)$, $\dot{X}(t)$ and $\ddot{X}(t)$ in the mathematical model. The solution of the equation will be found in (22) and (25), also be found that in term $\cos(\omega t+\emptyset)$, it cannot be equal to 0 because it will not be possible to find the solution of the equation, and from (22) and (25), must be arranged in the form of a matrix equation. to proceed to the next step. After getting the matrix equation, the variables X_1 and X_2 will be found, that is, X_1 will have a value equal to the Maximum amplitudes of $X_1(t)$ and $X_2(t)$ it cannot be equal to zero because if it is equal to 0, it indicates no vibration, which is not possible. The next step will be to use the Modal principle to find the values $X_1^{(1)}$ and $X_1^{(2)}$ by finding those values with the following equation.

$$\vec{X}(0) = [X]^t[M]\vec{X}(0) \quad (28)$$

In the final step, the natural frequency (Natural Frequency) or values 1 and 2 have been obtained by solving the equations mentioned above, including the values 3 and 4 from calculations through the Modal principle from Mode Shape. Vector, therefore, can be used to find the value of the Modal Matrix by finding from the equation as follows

$$[X] = [\vec{X}^{(1)} \quad \vec{X}^{(2)}] \quad (29)$$

When the value [X] is obtained at a certain time, it must find the coordinates q by assigning it 180° = πrad. To find the coordinates, use the equation to find the coordinates as follows.

$$\vec{q}(0) = [X]^t[M]\vec{X}(0) \quad (30)$$

Use the solution equation of the method to find coordinates when i=1 and i=2, then the solution equation will be used as follows.

$$q_i(t) = q_i(0) \cos \omega_i t + (q_i(0)/\omega_i)\sin \omega_i t \quad (31)$$

When solving the equation, the values $q_i(t) = q_i(0) \cos \omega_i t$ and $q_i(t)$ will be obtained as follows.

$$q_1(t) = q_1(0) \cos \omega_1 t \quad (32)$$

$$q_2(t) = q_2(0) \cos \omega_2 t \quad (33)$$

When the value q is obtained, it will be put into the equation to find the value $\vec{X}(t)$ by specifying the equation for finding the value as follows.

$$\vec{X}(t) = [X]\vec{q}(t) \quad (34)$$

B. Transfer function matrix: Two degrees of freedom suspension model

A transfer function matrix is a fundamental concept in control systems and systems engineering, especially when dealing with Multiple-Input Multiple-Output (MIMO) systems. It extends the idea of a single transfer function, which relates one input to one output, to systems with multiple inputs and outputs. This matrix-based approach allows for the analysis and design of complex systems where multiple variables interact simultaneously. The details of this method are explained in the following section [12].

- Transfer function model of suspension system

For a tricycle vehicle suspension system modeled as a 2 Degrees of Freedom (DOF) mass-spring-damper system, the system consists of the sprung mass (vehicle body) and the unsprung mass (wheel assembly). The inputs to the system are typically road profiles, which can be considered as external forces or displacements applied to the system. Consider Fig. 6 for a vehicle suspension system. When m_s is sprung mass or vehicle body mass, m_u is unsprung mass or wheel assembly mass, k_s is spring constant of the suspension spring, k_t is spring constant of the tire, C_s is damping coefficient of the suspension damper, $x_s(t)$ is displacement of the sprung mass from its equilibrium position, $x_u(t)$ is displacement of the unsprung mass from its equilibrium position and r(t) is road profile input or displacement of the road.

The transfer function matrix G(s) encapsulates the dynamic relationship between the road profile input R(s) and the displacements $X_u(s)$ and $X_s(s)$ of the unsprung and sprung masses, respectively, in the 2 DOF mass-spring-damper system of the vehicle. This transfer function is crucial for analyzing the response of the vehicle suspension system to road disturbances and for designing system parameter values to improve ride comfort and handling.

$$G(s)=\frac{X_s(s)}{R(s)}=\frac{k_t}{(m_s s^2+C_s s+k_s)(m_u s^2+C_s s+k_s+k_t)-(C_s s+k_s)^2} \quad (35)$$

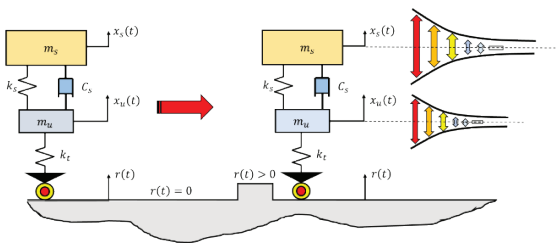

Fig. 5. A vehicle suspension system

- The system parameters of the transfer function model in the suspension system

The system parameters, such as, k_s, is spring constant of the suspension spring, k_t the spring constant of the tire, C_s is damping coefficient of the suspension damper have been measured by shock and spring measurement tool as shown in Fig. 6. The spring constant of two leaf springs and the damping coefficient of two shock absorbers are determined using a shock and spring measurement tool. Load cell sensors are used to measure the applied force from an external source. The value of applied force and displacement of the leaf spring from the origin are used to determine the spring constant value. The damping coefficient is determined by using the applied force and the rate of displacement. The transfer function matrix G(s) is used to draw the Bode plot, which is a graphical representation that shows how the system responds to different frequencies of road disturbance input. The Bode plot is a powerful tool for understanding how the suspension responds to road disturbances at different frequencies. It helps in designing and tuning the suspension to improve ride comfort and vehicle handling.

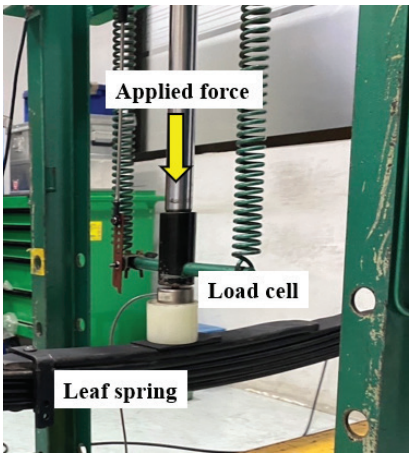

Fig. 6. A shock and spring measurement tool

C. Natural Frequency of the Vehicle Suspension System

The natural frequency of a two-degree-of-freedom (2DOF) vehicle suspension system refers to the frequency at which each mass (sprung and unsprung) tends to oscillate when not subjected to any external force (e.g., road input or damping). These frequencies are crucial in the design of vehicle suspension systems as they directly affect ride comfort and handling. The steps to find the natural frequencies are explained in the following section.

- Solve the characteristic equation

The natural frequencies are found by solving the characteristic equation derived from the determinant of the matrix equation of free vibration of the vehicle suspension system.

$$\det([K]-\omega^2[M])=0 \quad (36)$$

Where ω is the natural frequency? The determinant of the characteristic equation is used to determine ω^2 in the polynomial equation. The roots of ω^2 are ω_1, and when ω_1 and ω_2 are the natural

frequencies of vehicle body mass and wheel mass, respectively. The natural frequencies of a vehicle suspension system are essential parameters in vehicle dynamics, affecting both ride comfort and vehicle handling. These frequencies can be determined by modeling the system with equations of motion, forming the mass and stiffness matrices, solving the characteristic equation, and then computing the frequencies from the eigenvalues obtained [13].

- Vibration Data Collection

Two MPU-6050 sensors were utilized to measure the acceleration of a vehicle's body mass and two-wheel masses, respectively. The wiring diagram for the two MPU-6050 sensors is shown on Fig. 7. To measure the vibration data, an Arduino UNO connected to a 5 VDC power supply, two MPU-6050 sensors, and an HC-05 Bluetooth module were used to record the experimental data. The Bluetooth module sent the measured data signal to the computer via Bluetooth signal. The first MPU-6050 sensor was attracted to passenger seat of tricycle for measuring the acceleration of a vehicle's body mass and the second MPU-6050 sensor was attracted at differential gear for measuring the acceleration of wheel mass as shown in Fig. 7. The responds of the displacement at a vehicle's body mass and wheel mass have been used to identify two natural frequencies mode by the Fast Fourier transform method. When the tricycle was operated at a speed of 40 km per hour for the duration of 1,200 seconds in a straight line. Some limitations of this experiment include the potential drift and noise of MPU-6050 sensors, limited sampling rate, and possible data loss during Bluetooth transmission and environmental effects such as temperature and vibration. Additionally, the sensor placement may not perfectly represent the actual mass centers, and motion was assumed to occur mainly in one direction without cross-axis compensation.

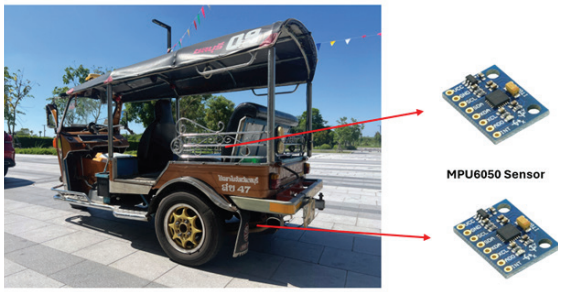

Fig. 7. The location of two MPU-6050 sensors in tricycle vehicles

- Determine natural frequency using the Fast Fourier Transform

Before performing calculations through the program, a real experiment must first be conducted to obtain experimental values. These values are used to verify that the calculated values, derived from the formulas, do not deviate by more than 10% from the values obtained through the actual experiment with the tricycle used as the test subject. This experiment was carried out using a two-section convertible three-wheeled vehicle. The tricycle was tested at three different speed ranges: 20, 30, and 40 kilometers per hour (km/h). The distance used for each test lap was 700 meters, with a total of two test runs conducted at each speed, equivalent to one test lap. Thus, each test run covered a distance of 1.4 kilometers (1,400 meters). The route used in the test will be the route of the road within the Panyapiwat Institute of Management, EEC Campus. The route will include 4 left curves, 1 right curve, and 3 uphill turns. Another method to determine the natural frequency is to measure the time-domain response of the vehicle suspension system using accelerometer sensors. The data should capture the displacement, velocity, or acceleration of the sprung and unsprung masses over time. This data is typically collected after the system is subjected to an impulse or step input, which excites the system's natural frequencies. The Fast Fourier transform is a computational algorithm used to convert the time-domain signal into the frequency domain. It will give you a spectrum showing the amplitude or power of each frequency component present in your signal. The Fast Fourier Transform is an efficient algorithm to compute the Discrete Fourier Transform of a sequence. The DFT converts a finite sequence of equally spaced samples of a function in the time domain into a sequence of coefficients of a finite combination of complex sinusoids [14]. The DFT equation can be shown as

$$X[k]=\sum_{n=0}^{N-1} x[n]\cdot e^{-j\cdot 2\pi\cdot k\cdot n/N}$$

$$\text{for } k=0,1,2,\cdots, N-1 \qquad (37)$$

Where X[k] is the DFT coefficient for the frequency component, x[n] is the input sequence in time-domain data, is the total number of samples, and the term $e^{-j\cdot 2\pi\cdot k\cdot n/N}$ is the complex exponential representing the frequency component. The natural frequencies correspond to the peaks in the FFT spectrum. The peaks can be identified from the plot of the DFT. Typically, the first peak corresponds to the natural frequency of the sprung mass, and the second significant peak corresponds to the unsprung mass.

D. Comparison with Driving Comfort Standard According to ISO 2631-1

The content area of ISO 2631-1 describes methods for measuring vibrations in various images entering the human body. Whether it's the posture of sitting, standing, or lying down, which is found in driving vehicles. Use of machinery or living in a residence, and the calculation of indicators indicating acceptable levels of vibration. In terms of health, Comfort, and awareness are the main ones.

The total effective acceleration value obtained can be used to evaluate driving comfort according to the recommended criteria as follows.

1. When less than 0.315 m/s^2 is not an uncomfortable level.
2. When between 0.315 m/s^2 - 0.63 m/s^2, it feels a bit uncomfortable.
3. When between 0.5 m/s^2 - 1 m/s^2, it feels fairly uncomfortable.
4. When between 0.8 m/s^2 - 1.6 m/s^2, it feels uncomfortable.
5. When between 1.25 m/s^2 - 2.5 m/s^2, it feels very uncomfortable.
6. When more than 2 m/s^2 is at an extremely uncomfortable level.

E. Optimum System Parameter Values with Driving Comfort Standard

From mathematical models, the simulation results of vehicle vibration in various system parameter values are used to set up a function of system parameter values due to the maximum acceleration of the vehicle's body mass and wheel mass. The variations of system parameter values in simulation results are set to ± 10% and ± 20% from the tested spring and damper values. Therefore, the function of maximum acceleration of the vehicle' body mass and wheel mass can be written as a polynomial model [15].

$$f(k_s, C_s)=a_1k_s^2+a_2C_s^2+a_3k_sC_s+b \quad (38)$$

The polynomial equation can be expanded into matrix form as

$$\underbrace{\begin{matrix} f(k_{s1}, C_{s1}) \\ f(k_{s2}, C_{s2}) \\ f(k_{s3}, C_{s3}) \\ \vdots \\ f(k_{sN}, C_{sN}) \end{matrix}}_{Y} = \underbrace{\begin{bmatrix} k_{s1}^2 & C_{s1}^2 & k_{s1}C_{s1} & 1 \\ k_{s2}^2 & C_{s2}^2 & k_{s2}C_{s2} & 1 \\ k_{s3}^2 & C_{s3}^2 & k_{s3}C_{s3} & 1 \\ \vdots & \vdots & \vdots & 1 \\ k_{sN}^2 & C_{sN}^2 & k_{sN}C_{sN} & 1 \end{bmatrix}}_{X} \underbrace{\begin{bmatrix} a_1 \\ a_2 \\ a_3 \\ b \end{bmatrix}}_{\beta} \quad (39)$$

The minimum values of k_s and C_s result in simpler manufacturing processes due to fewer leaf spring plates and reduced density in the damper. The minimum values of k_s and C_s must still ensure that the vibration of the vehicle's body mass and wheel mass meets the driving comfort standards. The critical values of k_s and C_s can be determined by the first derivative of the function representing maximum displacement as.

$$\partial f(k_s, C_s)/\partial k_s=0 \quad (40)$$

$$\partial f(k_s, C_s)/\partial C_s=0 \quad (41)$$

To check the minimum fixed points, the second derivative of the functions is certainly positive, which is enough to guarantee minimum fixed points.

$$\partial^2 f(k_s, C_s)/\partial k_s^2>0 \quad (42)$$

$$\partial^2 f(k_s, C_s)/\partial c_s^2>0 \quad (43)$$

From the polynomial equation, the equation can be rewritten as a regression equation.

$$Y = X\beta+ \varepsilon \quad (44)$$

ε is the error between the measurement signal and the model output from the polynomial equation. For the identification of β column vector, the least square method has been used by summing of squares of error.

$$SSE=(Y-X\beta)T(Y-X\beta) \quad (45)$$

Taking the partial derivative of with parameter β to minimize the square of error, the equation is set to zero.

$$\partial(SSE)/\partial\beta=0 \quad (46)$$

Therefore, the column vector β can be calculated by.

$$\beta=(X^TX)^{-1}X^TY \quad (47)$$

The column vector β contains model system parameters of the tricycle vehicle in the form of a polynomial equation.

F. Improved Suspension System with Frequency Response Analysis and Damping Ratio

From FFT analysis, Peaks in the FFT plot indicate frequencies where there is a significant amount of power in the signal, which could correspond to natural frequencies or dominant oscillation modes in a system. In general, the first peak corresponds to the natural frequency of the sprung mass, and the second significant peak corresponds to the unsprung mass. However, the ISO 2631-1 standard highlights that the human body is most sensitive in the range of 4 to 8 Hz for vertical vibration. Vibrations in this range can cause discomfort, fatigue, or motion sickness as they resonate with the human body's internal organs. To reduce amplitude in the 4 to 8 Hz range, frequency response analysis, or Bode plot, is utilized to attenuate vibrations within this frequency band. This approach is known as a band-stop filter, which effectively rejects frequencies between 4 and 8 Hz while permitting frequencies outside this range to pass through. The mathematical formulation for a standard band-stop filter is expressed as

$$H(s)=s^2+\omega_0^2/s^2+\omega_c s+\omega_0^2 \quad (48)$$

Where ω_0 represents the central frequency of rejection and ω_c denotes the width of the rejected bandwidth. The Bode plot of the band-stop filter is depicted in Fig. 8. To attenuate vibrations in the 4 to 8 Hz range, the suspension parameters can be adjusted to mitigate resonance within the critical frequency range, which is associated with the characteristic equation of the transfer function H(s) G(s) [16].

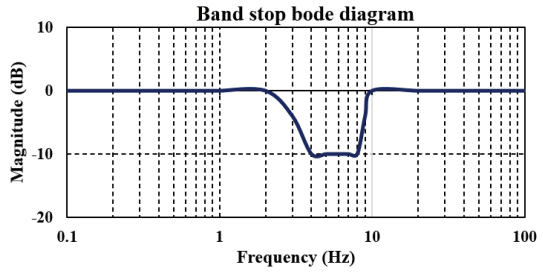

Fig. 8. The Bode plot of the band-stop filter, implemented to attenuate vibrations within the 4 to 8 Hz frequency range, is designed in compliance with the ISO 2631-1 standards.

Another criterion for riding comfort is to minimize the root mean square acceleration to below 0.315 m/s^2 or between 0.315 and 0.63 m/s^2. These vibration levels are categorized as comfortable and slightly uncomfortable, respectively. A damping ratio (ξ) of 0.3 is considered optimal for ride comfort in a vehicle suspension system, according to the ISO 2631-1 standard. At this damping ratio, the vehicle suspension system ensures that oscillations decay quickly after disturbances like bumps, potholes, or uneven road surfaces. If the damping ratio is too low, the suspension system is categorized as an underdamped system. In this case, the system will oscillate at the natural frequency, making the ride uncomfortable. If the damp ratio is too high, the suspension system is categorized as an overdamped system. In this case, the system will lead to a sluggish response, reduced ability to absorb shocks, and poor road-holding capability. The stiffness of a leaf spring can be adjusted to suit various requirements, such as riding comfort and durability. A common and straightforward method to decrease spring stiffness is to remove individual leaves from the pack, reduce the thickness of the leaves, or minimize the clamping force and friction between the leaves. Reducing the clamping or friction allows for more independent movement, which effectively reduces stiffness. The benefit of reducing spring stiffness is improved ride comfort performance. The damping coefficient of a damper, also known as a shock absorber, determines how effectively it dissipates energy and controls oscillations in a vehicle suspension system. Adjusting the damping coefficient can help achieve a balance between ride comforts and handling performance. Modifying the damping coefficient involves changing the fluid viscosity, orifice size, valve design, or gas pressure. The choice of damping coefficient depends on the specific requirements for ride comfort, stability, and handling. Reducing the damping coefficient provides a smoother ride and allows greater compliance over rough surfaces.

IV. Research Results

As for the experimental method, the researcher experimented using a system of mathematical equations to obtain the results of the experiment. The researcher divided the experimental method into three steps as follows:

A. Mathematical Calculation

After obtaining the equations of motion of the mathematical model, we then substitute the values of the variables in the equation to obtain the results of the variables whose values are not yet known. The calculation will have the following results.

$$\begin{bmatrix} -350\omega^2+479.92+509.6 & -(479.92+509.6)(0.64) \\ (-479.92+509.6)(0.64) & -140.07\omega^2+(479.92+509.6)(0.64^2) \end{bmatrix}$$

$$\begin{bmatrix} -350\omega^2+989.52 & 18.9952 \\ 18.9952 & -140.07\omega^2+405.44 \end{bmatrix}=0 \quad (49)$$

When calculating using the matrix method, the following calculation results will be obtained.

$$-350\omega^2(-140.07\omega^2+405.44)+989.52 \quad (50)$$
$$(140.07\omega^2+405.44)+ (18.9952\times18.9952)=0$$

$$49024.5\omega^4-280506\omega^2+400830=0 \quad (51)$$

By the method of finding the value of the matrix equation after substituting the values and $\Theta \neq 0$, the equation can be found using the Determinant method. This method is a function that gives the result as a scalar quantity. Which depends on the value of n in the n×n dimension of the square matrix. From the Determinant method, the equation will be obtained ω^4 and ω^2 in the form of an equation with the values of and in the equation. Arrange the form ω^2 of the equation so that, in the form ω^2 of an equation, both the equation and, when reformatting it to stay in the equation, the entire equation must then be assigned the variable $\lambda=\omega^2$ to the equation, and the roots of the equation that has been specified can be found. Obtained by using the Quadratic Formula equation. The variable values from all of the equations are $\lambda=\omega^2$, a = 49,024.5, b = -280,506, c = 400,830.

The calculation will have the following results is ω_1=1.7184 rad/s and ω_2=1.66394 rad/s. After using the Quadratic Formula equation, the natural frequencies will be obtained from the equations, all 2 natural frequencies, all of which will be in the value of and ω^2 the values that will not be negative and when obtained Once the value has been extracted, take that value and take the square root to get the angular velocity value, where the value of is the first natural frequency of the system and It is the second natural frequency of the system. After knowing the values of ω_1 and

ω_2, find the values of $X^{(1)}$ and $\theta^{(1)}$ by substituting ω_1 into the equation, and find the values of $X^{(2)}$ and $\theta^{(2)}$ by substituting ω_2 into the equation as well. When calculating using the matrix method, the following calculation results will be obtained.

(1)
$$-43.994X^{(1)}+18.9952\theta^{(1)}=0$$
$$18.9952\theta^{(1)}=43.994X^{(1)}$$

(2)
$$18.9952X^{(1)}-8.1725\theta^{(1)}=0$$
$$18.9952X^{(1)}=8.1725\theta^{(1)}$$

Find $X^{(2)}$, $\theta^{(2)}$ by plugging the result of y into the equation

$$\begin{bmatrix}20.4763 & 18.9952\\ 18.9952 & 17.6473\end{bmatrix}\begin{Bmatrix}X^{(2)}\\ \theta^{(2)}\end{Bmatrix}=\begin{Bmatrix}0\\ 0\end{Bmatrix} \quad (52)$$

When calculating using the matrix method, the following calculation results will be obtained.

(1)
$$20.4763X^{(2)}+18.9952\theta^{(2)}=0$$
$$18.9952\theta^{(2)}=20.4763X^{(2)}$$

(2)
$$18.9952X^{(2)}+17.6473\theta^{(2)}=0$$
$$17.6473\theta^{(2)}=18.9952X^{(2)}$$

When the results of the variable values are obtained, determine the ratio of the maximum amplitudes of r_1 and r_2 as follows

Find r_1 by plugging the result of y into the equation

(1)
$$r1=\theta^{(1)}/X^{(1)}=18.9952/8.1725=2.316$$

(2)
$$r1=\theta^{(1)}/X^{(1)}=43.994/18.9952=2.316$$

Find r_2 by plugging the result of y into the equation

(1)
$$r_2=\theta^{(2)}/X^{(2)}=-20.4763/18.9952=-1.078$$

(2)
$$r_2=\theta^{(2)}/X^{(2)}=-18.9952/17.6475=-1.078$$

Therefore, in order to substitute the equation to find a vibration diagram of the suspension system, it must occur at a certain time. The calculation will have the following results.

$$\vec{X}^{(1)}=\begin{Bmatrix}1\\ 2.316\end{Bmatrix}X^{(1)} \quad (53)$$

$$\vec{X}^{(2)}=\begin{Bmatrix}1\\ -1.078\end{Bmatrix}X^{(2)} \quad (54)$$

Therefore, in order to substitute the equation to find a vibration diagram of the suspension system, it must occur at a certain time. The calculation will have the following results.

[First Mode]
$$\vec{X}^{(1)}(t)=\begin{Bmatrix}X^{(1)}(t)\\ \theta^{(1)}(t)\end{Bmatrix}=\begin{Bmatrix}1\\ r_1\end{Bmatrix}X^{(1)}\cos(\omega_1 t+\emptyset_1)$$

[Second Mode]
$$\vec{X}^{(2)}(t)=\begin{Bmatrix}X^{(2)}(t)\\ \theta^{(2)}(t)\end{Bmatrix}=\begin{Bmatrix}1\\ r_2\end{Bmatrix}X^{(2)}\cos(\omega_2 t+\emptyset_2)$$

Then, solve the dynamical equation of motion (EOM) to be used in the Modal equation solving process to find the values of $X_1^{(1)}$ and $X_1^{(2)}$.

$$m\ddot{x}(t)+k_1x(t)-k_1l_1\theta(t)+k_2x(t)+k_2l_2(t)=0 \quad (55)$$

$$J_0\ddot{\theta}(t)-k_1l_1x(t)+k_1l_1^2\theta(t)+k_2l_2x(t)+k_2l_2^2\theta(t)=0 \quad (56)$$

Taking both equations and organizing them into the form of a matrix equation will be as follows:

$$\begin{bmatrix}m & 0\\ 0 & J_0\end{bmatrix}\begin{Bmatrix}\ddot{x}(t)\\ \ddot{\theta}(t)\end{Bmatrix}+\begin{bmatrix}k_1+k_2 & -k_1l_1+k_2l_2\\ -k_1l_1+k_2l_2 & k_1l_1^2+k_2l_2^2\end{bmatrix}=0 \quad (57)$$

Find the values $X_1^{(1)}$ and $X_1^{(2)}$ using the Modal method, using symbols to represent each value obtained with the symbols mentioned in (57).

The first step is to find the value of $X_1^{(1)}$ from $\vec{X}^{(i)^t}[M]\vec{X}^{(i)}=1$

$$i=1;\ \vec{X}^{(1)^t}[M]\vec{X}^{(1)}=1 \quad (58)$$

$$(X_1^{(1)})^2\{1 \quad 2.316\}\begin{bmatrix}350 & 0\\ 0 & 140.07\end{bmatrix}\begin{Bmatrix}1\\ 2.316\end{Bmatrix}=1 \quad (59)$$

$$(X_1^{(1)})^2[350 \quad 324.402]\begin{bmatrix}1\\ 2.316\end{bmatrix}=1 \quad (60)$$

$$X_1^{(1)}=1/33.186 \quad (61)$$

Therefore, then

$$\vec{X}^{(1)}=\begin{Bmatrix}1/33.186\\ 2/33.186\end{Bmatrix} \quad (62)$$

The second step is to find the value of $X_1^{(2)}$ from $\vec{X}^{(i)^t}[M]\vec{X}^{(i)}=1$

$$i=1;\ \vec{X}^{(2)^t}[M]\vec{X}^{(2)}=1 \quad (63)$$

$$(X_1^{(2)})^2\{1 \quad -1.078\}\begin{bmatrix}350 & 0\\ 0 & 140.07\end{bmatrix}\begin{Bmatrix}1\\ -1.078\end{Bmatrix}=1 \quad (64)$$

$$(X_1^{(2)})^2[350 \quad -150.99]\begin{bmatrix}1\\ -1.078\end{bmatrix}=1 \quad (65)$$

$$X_1^{(2)}=1/22.644 \quad (66)$$

Therefore, then

$$\vec{X}^{(2)}=\begin{Bmatrix}1/22.644\\ -1.078/33.186\end{Bmatrix} \quad (67)$$

In the final step, the natural frequency (Natural Frequency) or values 1 and 2 have been obtained by solving the equations mentioned above, including the values 3 and 4 from calculations through the Modal principle from Mode Shape. Vector, therefore, can be used to find the value of the Modal Matrix. When substituting the values in the equation, we will get the following:

$$[X]=\begin{bmatrix}1/33.186 & 1/22.644\\ 2/33.186 & -1.078/22.644\end{bmatrix} \quad (68)$$

$$[X]=\begin{bmatrix} 1/33.186 & 2/33.186 \\ 1/22.644 & -1.078/22.644 \end{bmatrix} \quad (69)$$

When the value [X] is obtained at a certain time, it must find the coordinates q by assigning it 180°=πrad. The calculation will have the following results.

$$\vec{q}(0)=\begin{Bmatrix} q_1(0) \\ q_2(0) \end{Bmatrix} \quad (70)$$

$$\vec{q}(0)=\begin{bmatrix} 1/33.186 & 2/33.186 \\ 1/22.644 & -1.078/22.644 \end{bmatrix}\begin{bmatrix} 350 & 0 \\ 0 & 140.07 \end{bmatrix}\begin{bmatrix} 0 \\ 0.2617 \end{bmatrix} \quad (71)$$

$$\begin{Bmatrix} q_1(0) \\ q_2(0) \end{Bmatrix}=\begin{bmatrix} 2.2091 \\ -1.7447 \end{bmatrix} \quad (72)$$

Use the solution equation of the method to find coordinates when i=1 and i=2. Use the solution equation of the method to find coordinates when i=1

$$q_i(t) = q_i(0)\cos \omega_i t+(q_i(0)/\omega_i)\sin \omega_i t \quad (73)$$

$$q_1(t) = 2.2091 \cos(1.7184)t \quad (74)$$

Use the solution equation of the method to find coordinates when i=2

$$q_i(t) = q_i(0) \cos \omega_i t+(q_i(0)/\omega_i) \sin \omega_i t \quad (75)$$

$$q_2(t) = -1.7447 \cos(1.66394)t \quad (76)$$

When the value q is obtained, it will be put into the equation to find the value $\vec{X}(t)$ by specifying the equation for finding the value. The calculation will have the following results.

$$\vec{X}(t)=\begin{bmatrix} 1/33.186 & 2/33.186 \\ 1/22.644 & -1.078/22.644 \end{bmatrix}\begin{Bmatrix} 2.2091\cos(1.7184)t \\ -1.7447\cos(1.66394)t \end{Bmatrix} \quad (77)$$

$$\vec{X}(t)=\begin{Bmatrix} 0.6657\cos 1.7184t-0.077\cos 1.66394t \\ 0.1331\cos 1.7184t+0.083\cos 1.66394t \end{Bmatrix} \quad (78)$$

B. Analysis of Results by Using Computer Programs and Comparison of Analysis Results with Comfort Standard Values

In this test, this measuring device will be assembled at various points on the tricycle. The points used in the assembly for testing are the Passenger seat and the Tricycle shaft, which will be located at the back of the tricycle. Since the researcher will only measure the vibration values for passengers.

In this section, numerous experimental results will be shown. The first experimental result is the data sets of system parameters, such as k_s is the spring constant of the suspension spring k_t is spring constant of the tire, C_s is damping coefficient of the suspension damper, in numerous conditions from the testing machine, and ξs , ξu are the damping ratios of the sprung mass and the unsprung mass, respectively. The system parameters are shown in Table II.

TABLE II
THE SYSTEM PARAMETERS OF THE TRICYCLE IN NUMEROUS CONDITIONS

Suspension Condition	System Parameters						
	k_s	k_t	C_s	m_s	m_u	ξ_s	ξ_u
Unit	N/m	N/m	$N\text{-}s/$	kg	kg	-	-
Soft	450	2710	485	350	35	0.61	0.78
Normal	510	3075	520	350	35	0.62	0.79
Hard	560	3370	614	350	35	0.69	0.89

The design and evaluation of the tricycle's body acceleration under three suspension settings—normal, hard, and soft—are illustrated in Fig. 9. Among these, the soft suspension configuration exhibits the highest variability in body acceleration. The maximum acceleration recorded under the soft suspension condition is 2.25 m/s² in the downward direction. In comparison, the maximum accelerations for the normal and hard suspension settings are 1.12 m/s² and 2.13 m/s², respectively, also in the downward direction. The Root Mean Square (RMS) values of body acceleration range from 0.985 m/s² to 1.085 m/s² across the configurations. According to ISO 2631-1, these RMS acceleration levels fall within the classification of fairly uncomfortable. Fig. 10 presents the Power Spectral Density (PSD) for each suspension condition, which represents the distribution of vibration power over frequency, computed via the Fast Fourier Transform (FFT). The primary peaks in the PSD indicate the system's natural frequencies. The first peak typically corresponds to the natural frequency of the sprung mass (vehicle body), while the second peak represents the natural frequency of the unsprung mass (wheel assembly). The observed trend shows that the natural frequency increases as the suspension stiffness is increased from soft to hard. Specifically, the natural frequency of the vehicle body ranges from 1.058 Hz to 1.181 Hz, while the natural frequency of the wheel mass varies from 9.428 Hz to 10.517 Hz, depending on the suspension setting. To attenuate vibrations within the frequency range of 4 to 8 Hz—as identified by ISO 2631-1 as critical for human comfort—a modified suspension system was designed. This design involves adjusting the damping coefficient and spring stiffness, which are directly related to the characteristic equation of the combined transfer function $H(s) \cdot G(s)$, where $H(s)$ is a band-stop filter designed to reject vibrations in the 4 to 8 Hz range, and $G(s)$ is the transfer function of the vehicle suspension system. The modified suspension parameters include a spring constant of k_s = 485 N/m, a tire stiffness of k_t = 2,214 N/m, and a damping coefficient of C_s = 253 Ns/m, achieving a damping ratio of 0.3 for improved ride comfort. Fig. 11 compares the PSD results of the normal and modified suspension systems. The modified configuration demonstrates

a significant reduction in spectral amplitudes within the 4 to 8 Hz range, indicating effective vibration rejection. The RMS acceleration for the modified suspension system is reduced to 0.537 m/s², which, according to ISO 2631-1, corresponds to a comfort level categorized as slightly uncomfortable. This marks an improvement in ride quality from the previously classified fairly uncomfortable level. Fig. 12 illustrates the time-domain acceleration response of the tricycle body under normal and modified suspension conditions. The maximum body acceleration under the normal suspension is 1.12 m/s² in the downward direction, whereas the modified suspension reduces this peak to 0.582 m/s². These findings confirm that the modified suspension configuration enhances ride comfort by mitigating both the amplitude and variability of vibrations experienced by the vehicle body.

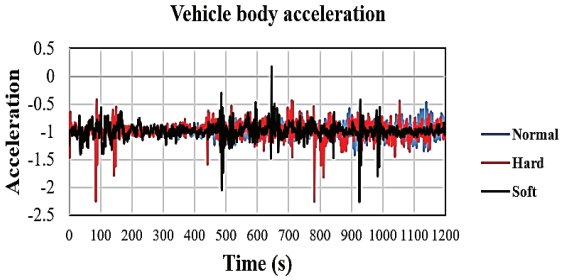

Fig. 9. Vehicle body acceleration in normal, hard, and soft conditions of the suspension system

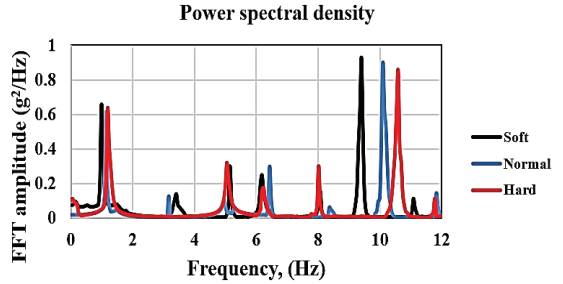

Fig. 10. Power spectral density in normal, hard, and soft conditions of the suspension system

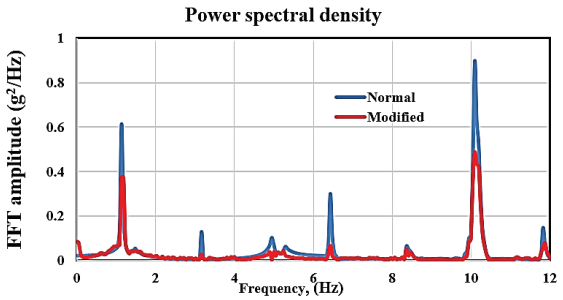

Fig. 11. Power spectral density in normal and modified conditions of the suspension system

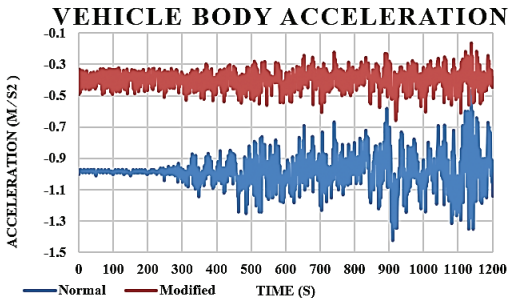

Fig. 12. The tricycle vehicle body acceleration when the suspension systems have been adjusted to normal and modified conditions

V. Discussion

The experimental results demonstrate the significant influence of suspension settings on ride comfort and the dynamic response of a tricycle structure. Among the tested conditions, soft, normal, and hard suspension, the soft suspension setting resulted in the highest variation in vehicle body acceleration, with a maximum downward acceleration of 2.25 m/s². This indicates that the damping in this condition is insufficient, allowing a considerable amount of road-induced vibration to be transmitted into the vehicle structure. In contrast, the normal and hard suspension setups provided greater stability, with reduced maximum accelerations of 1.12 m/s² and 2.13 m/s², respectively. However, while the hard suspension reduced overall body movement, it increased discomfort due to higher-frequency vibrations. The Root Mean Square (RMS) acceleration values ranged from 0.985 to 1.085 m/s², which, according to ISO 2631-1, is categorized as Fairly Uncomfortable. This suggests that none of the tested suspension configurations provided truly satisfactory ride comfort. The analysis of the Power Spectral Density (PSD) supports these findings, revealing spectral peaks corresponding to the system's natural frequencies, which vary depending on the suspension condition. The vehicle body's natural frequency increased from 1.058 Hz (soft) to 1.181 Hz (hard), while the wheel mass frequency rose from 9.428 Hz to 10.517 Hz. These results confirm that suspension stiffness has a direct effect on vibration behavior. To improve ride comfort, a modified suspension system was developed by adjusting the damping coefficient (Cs = 253 N·s/m) and spring constants (k_s = 485 N/m, k_t = 2,214 N/m). The goal was to reduce vibrations in the 4-8 Hz range—a frequency range to which the human body is particularly sensitive. This was achieved using a band-stop transfer function H(s) in combination with the vehicle suspension transfer function G(s) to reject vibrations in this range. After modification, the RMS acceleration

was reduced to 0.537 m/s², which falls under the category of Slightly Uncomfortable per ISO 2631-1. This indicates a clear improvement in ride comfort. The maximum downward acceleration of the vehicle body decreased from 1.12 m/s² (normal suspension) to only 0.582 m/s² (modified suspension). From these results, it can be concluded that targeted tuning of the suspension system, guided by vibration analysis and ISO 2631-1 standards, can effectively enhance ride comfort—both by reducing overall acceleration levels and minimizing vibration energy within sensitive frequency bands. For future studies, the use of adaptive or semi-active suspension systems may be considered to better accommodate various road conditions and further improve comfort.

VI. Conclusions

This study confirms that suspension tuning plays a critical role in enhancing ride comfort for tricycle vehicles. Among the tested configurations, the modified suspension system designed to attenuate vibrations within the sensitive frequency range of 4 to 8 Hz provided the most favorable results. It significantly reduced both peak acceleration and Root Mean Square (RMS) values, improving the ride comfort classification from fairly uncomfortable to slightly uncomfortable based on ISO 2631-1 standards. These findings underscore the importance of systematic suspension design based on vibration analysis and standard-based performance criteria. The proposed approach demonstrates that targeted adjustment of damping and stiffness parameters can effectively mitigate uncomfortable vibrations. Furthermore, the combined use of mathematical modeling, simulation, and experimental validation offers a robust framework for optimizing suspension systems. This methodology may be extended to other vehicle types, and future research could explore the implementation of adaptive or semi-active suspension systems to enhance performance under varying road conditions.

References

[1] Department of Land Transport, "Annual report 2021," *Dept. Land Transp.*, 2022. [Online]. Available: https://rapi.mot.go.th/uploads/2564_e0ce69451d.pdf [Accessed: Dec. 18, 2024].

[2] S. Isarnawe, S. Chattharupracha, and S. Khetprathum, "Design and development of suspension parts for in-wheel TMAC Formula," Ph.D. dissertation, Naresuan Univ., Phitsanulok, Thailand, 2017.

[3] S. S. Rao, *Mechanical Vibrations*, 5th ed. Upper Saddle River, NJ, USA: Pearson, 2010, pp. 129-130.

[4] S. S. Rao, *Mechanical Vibrations*, 5th ed. Upper Saddle River, NJ, USA: Pearson, 2010, p. 159.

[5] R. Darus and Y. M. Sam, "Modeling and control active suspension system for a full car model," in *Proc. 5th Int. Colloq. Signal Process. Appl. (CSPA)*, 2009, pp. 13-18.

[6] K. Jaisaard and W. Santipach, "A comparative study of ride comfort between EMU-A1 and EMU-B1 trains of BTS on Sukhumvit line from N8 to E14 stations," Ph.D. dissertation, Kasetsart Univ., Bangkok, Thailand, 2021.

[7] Arduino LLC, "Arduino," *Arduino off Website*, 2015. [Online]. Available: https://www.arduino.cc/ [Accessed: Dec. 18, 2024].

[8] A. Guo, "Vibration sensor design research," *Sens. Transducers*, vol. 169, no. 4, pp. 228-232, Apr. 2014.

[9] U. T. Ceyhanli and M. Bozca, "Experimental and numerical analysis of the static strength and fatigue life reliability of parabolic leaf springs in heavy commercial trucks," *Mech. Eng.*, vol. 12, no. 7, pp. 1-17, Jul. 2020.

[10] S. S. Rao, *Mechanical Vibrations*, 5th ed. Upper Saddle River, NJ, USA: Pearson, 2010, pp. 472-480.

[11] A. Shirahatti, P. S. S. Prasad, P. Panzade, and M. M. Kulkarni, "Optimal design of passenger car suspension for ride and road holding," *J. Braz. Soc. Mech. Sci. Eng.*, vol. 30, pp. 66-76, 2008.

[12] S. S. Rao, *Mechanical Vibrations*, 5th ed. Upper Saddle River, NJ, USA: Pearson, 2010, p. 502.

[13] S. S. Rao, *Mechanical Vibrations*, 5th ed. Upper Saddle River, NJ, USA: Pearson, 2010, pp. 654-698.

[14] D. Hanafi, "PID controller design for semi-active car suspension based on model from intelligent system identification," in *Proc. 2nd Int. Conf. Comput. Eng. Appl. (ICCEA)*, 2010, pp. 60-63.

[15] A. Anandan and A. Kandavel, "Investigation and performance comparison of ride comfort on the created human–vehicle–road integrated model adopting genetic algorithm optimized proportional–integral–derivative control technique," *Inst. Mech. Eng., Part K: J. Multi-body Dyn.*, vol. 234, no. 2, pp. 288-305, Feb. 2020.

[16] V. Popovic, D. Jankovic, and B. Vasic, "Design and simulation of active suspension system by using MATLAB," *SAE Tech. Paper*, no. 2000-05-0180, 2000. [Online]. Available: https://doi.org/10.4271/2000-05-0180 [Accessed: Jan. 10, 2025].

[17] S. Chow, P. Eisen, H. Johnson, and P. C. van Oorschot, "White-box cryptography and an AES implementation," in *Proc. 9th Annu. Int. Workshop Sel. Areas Cryptogr. (SAC)*, 2002, pp. 250-270.

[18] J. Lu, H. Sibai, and E. Fabry, "Adversarial examples that fool detectors," *arXiv*, 2017. [Online]. Available: https://arxiv.org/abs/1712.02494 [Accessed: Apr. 14, 2024].

[19] S. Nidhra and J. Dondeti, "Black box and white box testing techniques—a literature review," *Int. J. Eng. Sci. Adv. Technol. (IJESA)*, vol. 2, no. 2, pp. 29-50, Jun. 2012.

[20] W. Hui, "Physical adversarial attack meets computer vision: A decade survey," *arXiv*, 2022. [Online]. Available: https://arxiv.org/abs/2209.15179 [Accessed: Jan. 20, 2024].

[21] C. Sitawarin, A. N. Bhagoji, A. Mosenia, and P. Mettal, "Rogue signs: Deceiving traffic sign recognition with malicious ads and logos," *arXiv*, 2018. [Online]. Available: https://arxiv.org/abs/1801.02780 [Accessed: Apr. 15, 2024].

[22] I. Evtimov et al., "Robust physical-world attacks on machine learning models," *arXiv*, 2017. [Online]. Available: https://arxiv.org/abs/1707.08945 [Accessed: Jan. 20, 2024].

[23] Z. Zhang and M. Sabuncu, "Generalized cross entropy loss for training deep neural networks with noisy labels," *arXiv*, 2018. [Online]. Available: https://arxiv.org/abs/1805.07836 [Accessed: Jan. 20, 2024].

Chaiyawoot Narintharangkul graduated with a degree in Automotive Manufacturing Engineering from Panyapiwat Institute of Management, Thailand, in March 2020, and is currently pursuing a master's degree in the Faculty of Engineering and Technology. Used to work as an Inspection Engineer trainee at Keisokukensa Company in 2020. Currently, a job as a Senior Officer in the Engineering and Technology Faculty at Panyapiwat Institute of Management, Nonthaburi, Thailand.

Poom Jatunitanon received a Doctor of Engineering in Mechanical Engineering from Kasetsart University, Thailand, in 2017. Used to be a professor in automotive manufacturing engineering, from 2019 to 2025 at the Faculty of Engineering and Technology at Panyapiwat Institute of Management, Thailand, and current job as Head of automotive manufacturing engineering at the Faculty of Engineering and Technology at Panyapiwat Institute of Management, Nonthaburi, Thailand.

Physical Interference Attacks on Autonomous Driving

Chuanxiang Bi[1] and Jian Qu[2*]
[1,2]Faculty of Engineering and Technology, Panyapiwat Institute of Management, Nonthaburi, Thailand
E-mail: 6572100057@stu.pim.ac.th, jianqu@pim.ac.th

Received: February 1, 2024 / Revised: April 4, 2024 / Accepted: June 25, 2024

***Abstract*—Recent studies have revealed that there are serious security risks to autonomous driving, despite the notable advancements made by deep neural networks in this field. Simple sticker jamming has little experimental validation, despite recent proposals for physical attacks successfully implementing jamming in the real world and misleading autonomous driving recognition. This study focuses on the practicality of various sticker-based physical jammers, such as background noise, colorful stickers, smiley face stickers, and QR code stickers. To boost the study's actual impartiality, we replace the genuine self-driving car in this work with a smart car that performs similar activities. We then utilize three models to train our dataset and carry out five sets of tests. Based on the results, it can be concluded that the QR code sticker has the most potential to interfere with the smart car. This interference causes the smart car's accuracy in recognizing road signs to be between 30% and 40%, whereas the accuracy of the other interferences is over 50%. Furthermore, it demonstrated that, out of the three models, Resnet18 had the best anti-interference capability.**

***Index Terms*—Deep Neural Networks, Autonomous Driving, Physical Attacks, Smart Car, Stickers, Resnet18**

I. Introduction

Deep Neural Networks (DNNs) [1] have achieved amazing success in many fields, such as natural language processing [2] and autonomous driving [3]-[7]. However, new research shows that DNNs are vulnerable to adversarial attacks, which can pose significant security risks. Deliberate manipulation of DNN inputs can lead to misbehavior, making adversarial attacks a popular area of academic research with practical implications for real-world applications. In the field of computer vision, adversarial attacks [8]-[10] are now divided into two categories, digital and physical, with the main difference being their different forms. The digital form, where the attacker can feed the input digital image directly into the DNN classifier, also suggests that most digital attacks are white-box attacks, where the attacker needs to know the full details of the model. Digital attacks [11], [12], although they perform well in modeling, are widespread and difficult to identify; they are susceptible to their surroundings, making it difficult to migrate the digital attacks to the physical world. However, physical attacks [13], [14] are carried out in real environments and are therefore more practical and valuable for research and development compared to digital attacks, so more people have gone into physical attacks. But so far, physical attacks on computer vision systems are still very challenging. Physical attacks must be robust enough to withstand variations in illumination, viewing distance, and angle, and image distortion due to camera limitations. There is a limit to the area that can be disturbed by an attacking target. Any background image behind a road sign in a captured image is an example of a disturbance that an algorithm can introduce into a digital image. However, since there is no stable background in the real world, it is not possible to perturb the background there. As a result, only the attacked party itself can be attacked. Furthermore, there are already several available attack techniques; some of them produce complex patterns, while others produce microscopic attacks that are imperceptible to the human eye. A technique for misclassifying printed hostile instances when viewed through a smartphone camera has been demonstrated by Kurakin *et al.* [15]. Alternatively, it is more challenging to apply these techniques in the real world. Others have gone on to attack real stop signs so that self-driving cars do not recognize them correctly and make poor decisions. If the attacker can physically robustly manipulate the road sign, the deep neural network may misclassify it as some other action, which could lead to serious consequences. For example, ShapeShifter [16] uses formula execution to create adversarial stop signs with complex designs, but implementation in real traffic signs is challenging and prone to suspicion.

So, in response to the above problem, this paper focuses on physical attacks that are effective in the physical world, but we are different from most of the research nowadays, which uses physical attacks that are generated in code with targeted attacks, such that the attacks have precision, some of them are so tiny

that they may print out with missing pixel dots and lose their effectiveness. Some attacks are large and require the attacker to cover the entire road sign, but such attacks are often too noticeable and cumbersome to implement. The research in this paper is to find physical attacks-physical stickers-which already exist in the real world, and to experiment on traffic road signs with physical stickers through an established autonomous driving platform, and based on the experimental results, to come up with physical sticker attacks that are more threatening to the recognition of the road signs by the self-driving cars.

The contributions of this paper are:

1. This paper proposes that QR code stickers have the strongest ability to interfere with the recognition of road signs by self-driving cars; however, background noise has essentially no influence on the recognition of road signs by self-driving cars.

2. This paper uses the same dataset to train three kinds of deep network models resnet18, mobile net, and Alex net, through the test with physical stickers on the interference of road signs on the self-driving car, the experimental results show that the Resnet18 in the three kinds of models in the strongest anti-jamming ability.

II. Literature Review

A. Adversarial Attack

Adversarial Attacks are purposefully designed input samples that allow machine learning models to misclassify or misjudge. Such attacks may result in a decrease in model performance or may fail. A common application of adversarial attacks is in image classification tasks, where the original image is modified in such a way that the model outputs incorrect classification results by making modifications to the original image that are smart and imperceptible to the human eye. x is the original input. x' in the adversarial sample $x' = x + \delta$, which is obtained by adding a smart perturbation δ. $f(x)$ is the model's output for the original input x. The goal of an adversarial attack is to cause the model to misclassify or miscategorize the original image, but the model's performance may be degraded. The goal of the adversarial attack is to make the output of the adversarial sample x' from the model different from the original input x, so that $\arg\max f(x') \neq \arg\max f(x)$.

Attacks against traffic signs were typically conducted in a white box [17] setting in the early days. Lu et al. [18] attacked the traffic sign detection algorithm. But for the method to work, there had to be significant perturbations because it was not stable enough. Generative Adversarial Networks (GANs) can also generate adversarial instances; however, controlling the generation process of GANs makes it challenging to employ them for focused attacks on certain targets. White-box environments can yield high success rates since they give complete access to the machine-learning model. Nevertheless, the attack method's efficacy sharply declines when it is applied to a black-box model. Black-box [19] assaults are significantly more useful in the real world and have received more practical research than white-box attacks. Black-box attacks, such as generic disturbances, are untargeted assaults that can be employed on any image. The attack strategy presented in this research is also under the category of black-box attacks, which can create an assault that can spoof a target model without the need for previous knowledge of the target model's structure and algorithms.

B. Physical-Realizability of Adversarial Perturbations

The success of adversarial attacks in the real world has been the subject of extensive academic research in recent years. An overview and comparative analysis of recent physical attacks are presented by Wei *et al.* [20]. Physical adversarial samples must be adjusted to varied camera processing and maintain their effectiveness at varying distances, shooting angles, and lighting conditions. Sittawarin *et al.* [21] suggested a technique in a similar study for concealing antagonistic samples on billboards next to traffic signs. Through the categorization attack, they altered the billboard image to make the model's output appear to be a traffic sign. This assault is hard to detect since it tricks not just the machine-learning model but also the human observer. Furthermore, by printing actual-sized road signs on paper and superimposing them over preexisting signs, the RP2 [22] approach can similarly fool DNN classifiers. In this work, we examine practical and successful physical attacks, like those reported in the previous investigations.

III. Methodology

In physical adversarial attacks, to maximize the performance of the model with the stickers on the sample targets and wrong classification results, the cross-entropy loss of the adversarial samples is generally minimized, and the loss function can be generally defined as:

$$J(x') = CrossEntropy(f(x'), y_{target}) + \lambda * Regularization(\delta)$$

x is the original input, $x' = Sticker(x)$ is the adversarial sample, and $f(x)$ is the adversarial sample model output. $CrossEntropy(f(x'), y_{target})$ denotes the cross-entropy loss [14] of the adversarial sample, and y_{target} is the target category set by the attacker. λ is the hyper-parameter used to balance the adversarial loss and the regularization term. $Regularization(\delta)$ is the regularization of the perturbation term, which can be either an L1 or L2 paradigm, to limit the size of the perturbation and prevent over-modification. Minimization of this loss

function will cause the model to produce incorrect classification results on adversarial samples, as it takes into account both classification error and a penalty on the size of the perturbation.

The paper focuses on attacking traffic signs, and this use case is chosen because self-driving cars have a larger security problem for adversarial attacks, and the response is obvious: in general, the real STOP road sign is captured by the camera, and then recognized by the DNN, predicted to be a STOP, and performs the STOP action. However, putting a physical sticker on the real STOP road sign will make the DNN recognize it incorrectly, predict it as another road sign, and execute the wrong action, which indicates that the physical sticker poses a threat to the security of autonomous driving. The adversarial physical attack studied in this paper is not to intentionally generate a targeted pattern in the digital world and then print it to cover the original road sign; that way, on the one hand, some tiny attacks will lose pixel points when printed out, which may weaken the effect of the attack. On the other hand, those with a lot of interference would feel unrealistic. However, the physical adversarial attacks studied in this paper adopt those that can appear in the usual world, which are closer to the real world and do not make people suspicious. In this paper, we print and paste some patterns that will not confuse people when they see them, but will be recognized incorrectly by self-driving cars when they see them. As in Fig. 1, QR codes are very common in the real world. Usually, there may be some unqualified individuals placing advertisements on road signs with recognizable QR codes. The purpose is to test whether the DNN identifies the error generated. A smiley face is a sticker that children like. The purpose is to test whether this type of sticker will disrupt the pattern of the road sign and cause the DNN to identify the error. The colored bar is the interference of multiple colors that occur in the real world. The purpose is to test whether DNNs are interfered with by multiple colors, and background noise is the cluttered background that may occur on road signs in the real world, and this purpose explores whether the attention of DNNs is interfered with Overall, this paper aims to explore the physical adversarial attacks that may occur in the real world and to gain further understanding by comparing the effects of these attacks on autonomous driving.

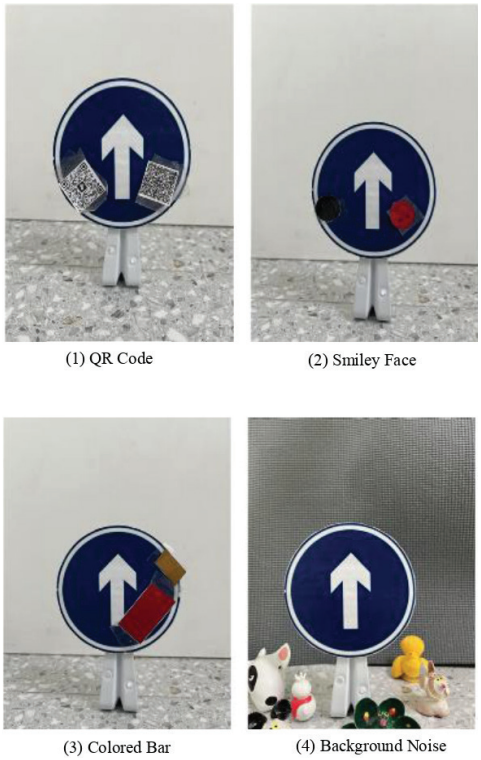

Fig. 1. Four types of physical stickers

IV. Experimental Setup

A. Experimental Environment

Due to the expensive and safety issues of self-driving cars, this paper selects scale model cars that can be used for self-driving research that simulate self-driving in real scenarios, and uses a Jetson Nano motherboard to make the car an independent agent. The smart car uses a 2,200 mAh battery pack as a power source, and, to approximate the most primitive self-driving car, uses only a camera as an input source to transmit data to the Jetson Nano for processing. The framework of the smart car is shown in Fig. 2. The Jetson Nano is equipped with a driver board that transmits the processing signals from the Jetson Nano to the motor to control the smart car, and incorporates a deep neural network classifier that allows the road sign recognition process to be observed in a more realistic context, thus allowing for a more accurate assessment of the model performance. In terms of the experimental environment, we experiment indoors,

and since we want to test whether the physical stickers have an effect on the smart car's recognition of road signs, we have to maintain stable environmental conditions. We used curtains to block the outside light, kept the surroundings unchanged, minimized other noises that could create interference, and kept the indoor lighting stable to create consistent lighting conditions.

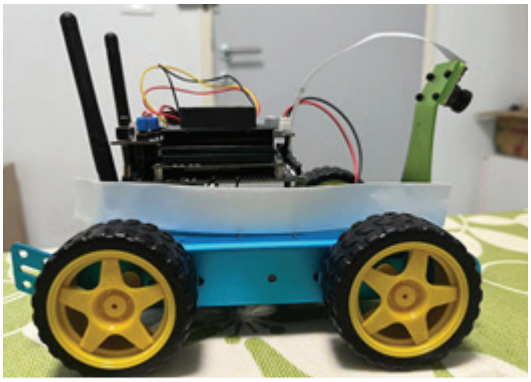

Fig. 2. Frame with Jetson Nano motherboard, and smart car with only one camera as input source

B. Dataset

In order to prevent experimentation by chance, this paper uses 12 road signs, all with the same base and material, to reduce the likelihood that the model will be able to recognize a road sign by observing differences in other aspects of the sign. Diversity is also increased by having different shapes and colors for each category of road signs, making the four categories much less different. With this design, this paper can conduct an effective autonomous driving study in a more realistic environment and improve the robustness of the model for road signs.

Next, in this paper, we use the smart car to collect pictures of the road signs made ourselves, we open the Jupyter and run our code to collect the data, as shown in Fig. 3, as we have four types of road signs about forward, left, right, stop, so the dataset we collect a four-category dataset with forward, left, RIGHT, STOP four categories and the size of the data images is 224*224. We collected 300 images for each of these road signs in the respective category they belong to as shown in Fig. 4. Specifically, we also collected 100 images of no road sign in front in the forward category, to make the cart move forward without road sign in front, in summary, this dataset, there are 3700 images in total, in order to be the model training is better.

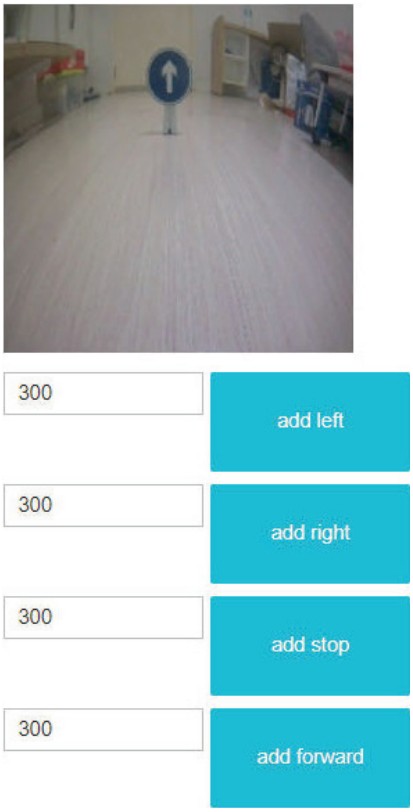

Fig. 3. Collecting images about four types of road signs: Forward, left, right, and stop, using the Jupyter platform

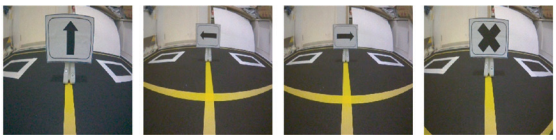

Fig. 4. One of the 4 road signs in the dataset is used as an example

C. Modele Training

In this study, we use Google Colab for training. The collated dataset was uploaded to Google Drive for model training. We adopted the PyTorch framework, specifically using torch 1.11.0, torch vision 0.12.0, Python 3.11, and CUDA 12.1 versions. By training in Colab, we expect to obtain models with good performance.

We also used three deep neural network models for training in our experiments to generate new deep learning models with different performances. These models are resnet18, mobile net, and AlexNet three models, ResNet18 has the advantage of depth and residual connectivity, the model can learn constant mapping, avoiding the loss of information, and maybe more effective in dealing with complex image scenes;

Mobile Net, due to its lightweight design, may be more suitable in resource-constrained environments and So it is more suitable to be used for smart cars in this paper; while AlexNet, as a classical model, has a wide range of applications in tasks such as image classification, target detection, and object recognition, and has better performance in various scenarios, which can be used as a reference benchmark. We chose these three different CNN methods for our experiments, which can evaluate their performance in road sign recognition tasks from different perspectives. Finally, we deploy the trained models to Jetson Nano for model testing and performance evaluation.

D. Experiment

We deployed the three trained models to the Jetson Nano in sequence, after which we tested the following five experiments with a smart car on road signs with different physical stickers, as shown in Fig. 5:

• 12 original road signs without any interference stickers; each road sign is tested ten times.

• 12 road signs with QR code stickers, each road sign is tested ten times.

• 12 road signs with smiley face stickers, each road sign tested ten times.

• 12 road signs with colored stickers; each road sign was tested ten times.

• 12 road signs without any interference stickers, but with ambient noise (background is changing), tested ten times per road sign.

The flow chart is shown in Fig. 6, Each road sign is tested 10 times, each time at a different angle and distance, and As can be seen in Fig. 7, the intelligent model car displays the probability distribution of the actions predicted in real time on our visualization interface when recognizing a road sign while making actions with high probability, and statistically counting the results based on this probability.

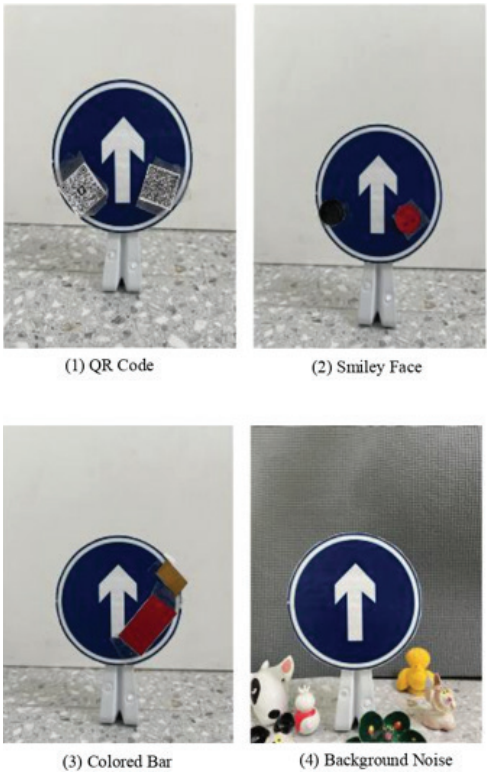

Fig. 5. As an example, one of the forward road signs was sequentially labeled with different physical stickers and placed with background noise

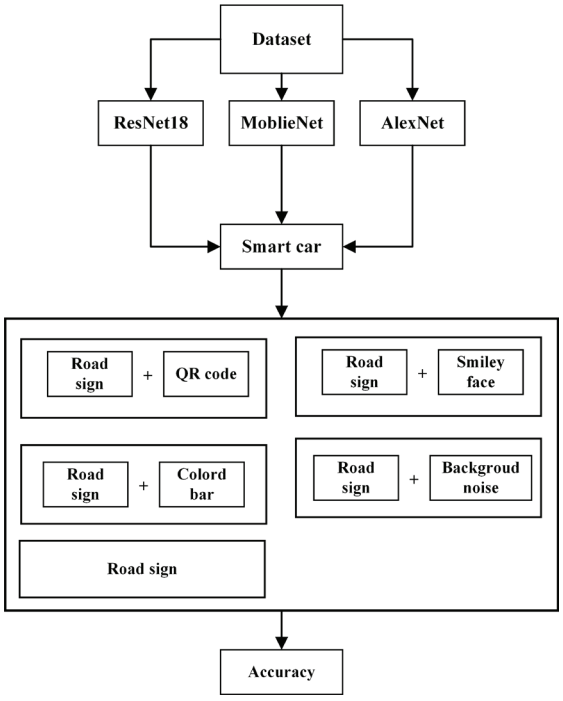

Fig. 6. Experimental framework diagram: the three trained models resnet18, MobileNet, and AlexNet, were deployed to the smart car in turn to test the road sign without interference, the road sign with QR code sticker, the road sign with smiley face sticker, the road sign with colorful sticker, and the road sign with background noise, respectively

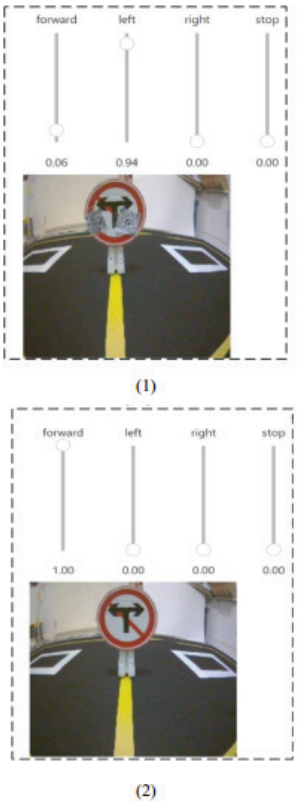

Fig. 7. The probability distribution of actions displayed on the visualization interface when the intelligent model car recognizes a road sign is plotted: When there is a physical sticker, the forward road sign is predicted to be left with a probability of 0. 94, and when there is no physical sticker, the forward road sign is predicted to be forward with a probability of 1

V. Result

A. Evaluation Methodology

Rather than utilizing the conventional mean calculation method, the experimental evaluation method presented in this study uses a four-category confusion matrix. We have the results from earlier experiments, but there is too much data for a direct comparison. As a result, we decided to combine and condense this fact using a scientific evaluation process. We employed three evaluation measures, which are as follows: precision, recall, F1, and accuracy.

$$\text{Precision} = \frac{TP}{TP + FP}$$

$$\text{Recall} = \frac{TP}{TP + FN}$$

$$F1 = \frac{2 \times \text{Precision} \times \text{Recall}}{\text{Precision} + \text{Recall}}$$

$$Accuracy = \frac{Number\ of\ correctly\ classified\ samples}{Total\ number\ of\ samples}$$

Here, we present two metrics—P (Positive) and N (Negative)—for assessing the model vehicle's capacity to perceive its surroundings. First, we designate the remaining classifications as Negative and present one as Positive. Here, P stands for a road sign that is favorably categorized, and N for a road sign that is negatively categorized. The smart car's predictions are shown by the letters T (True) and F (False), respectively, indicating correct and incorrect predictions. For instance, we utilize the other categories as the negative categorization and the LEFT category as the positive categorization to compute the correlation metrics for the LEFT category. When a road sign is correctly classified as positively categorized, the model automobile is said to be in the True Positive (TP) state; when wrongly classed as negatively categorized, it is shown to be in the False Positive (FP) state. The indicators TN (True Negative) and FN (False Negative), respectively, show that the model automobile accurately predicts negatively classified road signs as negatively categorized and incorrectly predicts negatively categorized road signs as favorably categorized. The category to be calculated is the reference for the associated calculation if the pertinent metrics for other categories need to be calculated.

B. Discussions

We performed the statistics by the evaluation methods mentioned above, and as can be seen from Table I, for the original road signs, the accuracy of the smart car recognition is high, as high as 100%, which indicates that the model is well fitted. Then we test several kinds of road signs with physical stickers. The results indicate that the QR code has the greatest interference for the smart car, with the lowest accuracy rate of 40%, and the ambient noise has the least interference for the smart car to recognize the road sign, with the highest accuracy rate of 98%. Smeily Face and Colored bars also have little interference for the smart car to acknowledge the road sign, but they also have a certain degree of interference with an accuracy rate of 89% and 75%.

From Table II and Table III, it can be seen that the same to Table I is that the QR code has the highest interference for the smart car, then Colored bar, Smiley face, and Background noise in that order, where Background noise has the lowest interference, which further indicates that the QR code has the highest interference for the smart car. Moreover, according to the provided experimental results, ResNet18 shows 100% accuracy in the recognition of original road signs, which indicates that ResNet18 has very good fitting ability in the face of simple, undisturbed situations. When confronted with road signs with physical stickers, ResNet18 showed higher accuracy relative to the other models. Even though the QR code caused the most interference for all the models, ResNet18 was able to maintain a relatively high accuracy (40%) in this case, whereas the other models showed a lower accuracy. This leads to the conclusion that ResNet18 is the most resistant to interference, and AlexNet is the least resistant.

TABLE I
EXPERIMENTAL RESULTS OF RESNET18 RECOGNIZING ORIGINAL ROAD SIGNS AND ROAD SIGNS AFFIXED WITH DIFFERENT DISTURBANCES

List	Class	Original	QR	Smiley Face	Colored Bar	Background Noise
Precision	Forward	1	0.44	0.93	0.72	0.96
	Left	1	0.42	0.86	0.81	1
	Right	1	0.61	1	1	0.96
	Stop	1	0.30	0.79	0.61	1
Recall	Forward	1	0.33	0.93	0.96	1
	Left	1	0.40	0.86	0.73	0.96
	Right	1	0.43	0.86	0.63	1
	Stop	1	0.46	0.90	0.70	096
F1	Forward	1	0.36	0.93	0.85	0.97
	Left	1	0.40	0.86	0.76	0.97
	Right	1	0.50	0.92	0.77	0.97
	Stop	1	0.36	0.84	0.65	0.97
Accuracy		**100%**	**40%**	**89%**	**75%**	**98%**

TABLE II
EXPERIMENTAL RESULTS OF MOBLIENET RECOGNIZING ORIGINAL ROAD SIGNS AND ROAD SIGNS AFFIXED WITH DIFFERENT DISTURBANCES

List	Class	Original	QR	Smiley Face	Colored Bar	Background Noise
Precision	Forward	0.85	0.33	0.74	0.51	0.82
	Left	0.87	0.36	0.73	0.58	0.81
	Right	0.89	0.54	0.80	1	0.89
	Stop	0.85	0.23	0.65	0.45	0.84
Recall	Forward	0.96	0.30	0.86	0.70	0.93
	Left	0.90	0.30	0.73	0.56	0.86
	Right	0.83	0.40	0.70	0.56	0.83
	Stop	0.76	0.36	0.63	0.50	0.73
F1	Forward	0.90	0.31	0.79	0.59	0.87
	Left	0.88	0.32	0.73	0.56	0.83
	Right	0.85	0.45	0.74	0.71	0.85
	Stop	0.80	0.28	0.63	0.47	0.78
Accuracy		**86%**	**34%**	**73%**	**58%**	**84%**

TABLE III
EXPERIMENTAL RESULTS OF ALEXNET RECOGNIZING ORIGINAL ROAD SIGNS AND ROAD SIGNS AFFIXED WITH DIFFERENT DISTURBANCES

List	Class	Original	QR	Smiley Face	Colored Bar	Background Noise
Precision	Forward	0.83	0.40	0.77	0.48	0.81
	Left	0.82	0.30	0.68	0.53	0.76
	Right	0.96	0.50	0.76	0.87	0.96
	Stop	0.78	0.18	0.61	0.36	0.78
Recall	Forward	0.86	0.40	0.80	0.56	0.86
	Left	0.80	0.30	0.66	0.50	0.76
	Right	0.86	0.26	0.66	0.46	0.83
	Stop	0.86	0.26	0.70	0.50	0.83
F1	Forward	0.84	0.40	0.78	0.51	0.83
	Left	0.80	0.30	0.66	0.51	0.76
	Right	0.90	0.34	0.70	0.60	0.89
	Stop	0.81	0.21	0.65	0.41	0.80
Accuracy		**85%**	**30%**	**70%**	**50%**	**82%**

VI. Conclusion

With the development of automated driving technology, road sign recognition as one of the key tasks in the automated driving system, so there are many researches to create interference for road sign recognition, but there are some digital attacks that cannot be migrated to the real world, which leads to failure, and there are also some physical attacks that create a larger interference, which is easy to be detected. We have done this by finding out that there are various physical interferences in the real world, such as QR codes affixed and graffiti painted, which may negatively affect the accuracy of road sign recognition. In this paper, we test the interference of QR code stickers, smiley face stickers, colored stickers, and background noise on the recognition of road signs by using a smart car, and the experimental results show that the physical interference of QR code stickers has the most significant impact on the accuracy of road sign recognition by the smart car, and the recognition accuracy is only 30% to 40%, which is much lower than that of the smart car. 30% to 40%, much lower than other types of interference. This suggests that QR code interference may cause serious safety hazards to the autonomous driving system and requires special attention and targeted solutions. In addition, the impact of other types of physical interference on road sign recognition is relatively small, and the recognition accuracy is kept above 50%, but there is still a certain degree of influence. And, in the in-depth comparison of the performance of the three different models, we further confirm the excellent performance of the ResNet18 model in resisting interference. This indicates that ResNet18 performs well in coping with physical interference in the street sign recognition task in the face of different types of physical interference.

In summary, the results of this study highlight the important impact of physical interference on the performance of road sign recognition in automated driving systems, especially the severity of QR code interference. Future research can further explore the mechanism of different types of physical interference on road sign recognition, as well as the future development towards physical defense that can be made to cope with the impact of physical interference on the road sign recognition performance of an automated driving system. All these will help to improve the robustness and safety of the system, and promote the development of automatic driving technology towards a more mature and reliable.

Acknowledgment

Conceptualization, CX. B. and J. Q.; methodology, CX. B. and J. Q.; software, CX. B. and J. Q.; validation, CX. B. and J. Q.; formal analysis, CX. B. and J.Q.; investigation, CX. B. and J. Q.; data curation, CX. B. and J. Q.; writing—original draft preparation, CX. B. and J. Q.; writing—review and editing, CX. B. and J. Q.; visualization, CX. B. and J. Q.; supervision, J. Q.; All authors have read and agreed to the published version of the manuscript. J. Q. is the corresponding author.

The first author received scholarship support from CPALL for conducting this research in PIM.

References

[1] A. Aldahdooh, W. Hamidouche, S. A. Fezza, and O. Deforges, "Adversarial example detection for DNN models: A review and experimental comparison," *Artif Intell Rev*., vol. 55, no. 6, pp. 4403-4462, May 2022.

[2] J. Li, X. Chen, E. Hovy, and D. Jurafsky, "Visualizing and understanding neural models in NLP," *arXiv*, 2015. [Online]. Available: https://arxiv.org/abs/1506.01066 [Accessed: Jan. 14, 2024].

[3] J. Qu and S. Shi, "Multi-Task in autonomous driving through RDNet18-CA with LiSHTL-S loss function," *ECTI-CIT*, vol. 18, no. 2, pp. 158-173, Apr. 2024.

[4] Y. Li and J. Qu, "A novel neural network architecture and cross-model transfer learning for multi-task autonomous driving," *Data Technologies and Applications*, vol. 58, no. 5, pp. 693-717, Jan. 2024, https://doi.org/10.1108/DTA-08-2022-0307

[5] S. Ding and J. Qu, "Automatic driving for road tracking and traffic sign recognition," *STA*, vol. 27, no. 4, pp. 343-362, Dec. 2022.

[6] Y. Li and J. Qu, "Intelligent road tracking and real-time acceleration-deceleration for autonomous driving using modified convolutional neural networks," *Curr. Appl. Sci. Technol.*, vol. 22, no. 6, pp. 1-26, Mar. 2022..

[7] S. Ding and J. Qu, "Research on multi-tasking smart cars based on autonomous driving systems," *SN Computer Science*, vol. 4, no. 3, p. 292, Mar. 2023.

[8] T. B. Brown, D. Mané, A. Roy, M. Abadi, and J. Gilmer, "Adversarial patch," *arXiv*, 2017. [Online]. Available: https://arxiv.org/abs/1712.09665 [Accessed: Jan. 14, 2024].

[9] Y. Dong, F. Liao, T. Pang et al., "Boosting adversarial attacks with momentum," in *Proc. IEEE Conf. Comput. Vis. Pattern Recognit.*, 2018, pp. 9185-9193.

[10] A. Madry, A. Makelov, L. Schmidt et al., "Towards deep learning models resistant to adversarial attacks," *arXiv*, 2017. [Online]. Available: https://arxiv.org/abs/1706.06083 [Accessed: Jan. 14, 2024].

[11] N. Carlini and D. Wagner, "Towards evaluating the robustness of neural networks," in *Proc. IEEE Symp. Secur. Priv. (SP)*, 2017, pp. 39-57.

[12] S. -M. Moosavi-Dezfooli, A. Fawzi, and P. Frossard, "DeepFool: A simple and accurate method to fool deep neural networks," in *Proc. IEEE Conf. Comput. Vis. Pattern Recognit.*, 2016, pp. 2574-2582.

[13] R. Duan, X. Ma, Y. Wang et al., "Adversarial camouflage: Hiding physical-world attacks with natural styles," in *Proc. IEEE/CVF Conf. Comput. Vis. Pattern Recognit*., 2020, pp. 1000-1008.
[14] N. Akhtar and A. Mian, "Threat of adversarial attacks on deep learning in computer vision: A survey," *IEEE Access*, vol. 6, pp. 14410-14430, Jan. 2018.
[15] A. Kurakin, I. J. Goodfellow, and S. Bengio, "Adversarial examples in the physical world," in *Proc. Artif. Intell. Safety Security*, 2018, pp. 99-112.
[16] S. T. Chen, C. Cornelius, J. Martin, and D. Horng Chau, "Shapeshifter: Robust physical adversarial attack on Faster R-CNN object detector," in *Proc. Mach. Learn. Knowl. Discovery Databases: European Conf.*, 2019, pp. 52-68.
[17] S. Chow, P. Eisen, H. Johnson, and P. C. van Oorschot, "White-box cryptography and an AES implementation," in *Proc. 9th Annu. Workshop Sel. Areas Cryptogr. (SAC)*, 2002, pp. 250-270.
[18] J. Lu, H. Sibai, and E. Fabry, "Adversarial examples that fool detectors," *arXiv*, 2017. [Online]. Available: https://arxiv.org/abs/1712.02494 [Accessed: Apr. 14, 2024].
[19] S. Nidhra and J. Dondeti, "Black box and white box testing techniques-A literature review," *Int. J. Eng. Sci. Appl*., vol. 2, no. 2, pp. 29-50, Jun. 2012.
[20] W. Hui, "Physical adversarial attack meets computer vision: A decade survey," *arXiv*, 2022. [Online]. Available: https://arxiv.org/abs/2209.15179 [Accessed: Jan. 20, 2024].
[21] C. Sitawarin, A. N. Bhagoji, A. Mosenia, and P. Mettal, "Rogue signs: Deceiving traffic sign recognition with malicious ads and logos," *arXiv*, 2018. [Online]. Available: https://arxiv.org/abs/1801.02780 [Accessed: Apr. 15, 2024].
[22] I. Evtimov, K. Eykholt, E. Fernandes et al., "Robust physical-world attacks on machine learning models," *arXiv* , 2017. [Online]. Available: https://arxiv.org/abs/1707.08945 [Accessed: Jan. 20, 2024].
[23] Z. Zhang and M. Sabuncu, "Generalized cross entropy loss for training deep neural networks with noisy labels," *arXiv*, 2018. [Online]. Available: https://arxiv.org/abs/1805.07836 [Accessed: Jan. 20, 2024].

Chuanxiang Bi is currently studying for the Master of Engineering Technology, Faculty of Engineering and Technology, Panyapiwat Institute of Management, Thailand. He received B.B.A from Nanjing Tech University Pujiang Institute, China, in 2022. His research interests are Research direction is artificial intelligence, image processing, and autonomous driving.

Jian Qu is an Assistant Professor at the Faculty of Engineering and Technology, Panyapiwat Institute of Management. He received a Ph.D. with an Outstanding Performance award from Japan Advanced Institute of Science and Technology, in 2013. He received a B.B.A with Summa Cum Laude honors from the Institute of International Studies of Ramkhamhaeng University, Thailand, in 2006, and M.S.I.T from Sirindhorn International Institute of Technology, Thammasat University, Thailand, in 2010. He has been serving on a house committee for the Thai Superai project since 2020. His research interests are natural language processing, intelligent algorithms, machine learning, machine translation, information retrieval, image processing, and autonomous driving.

PAPER FORMAT (IEEE Style)

I. Format

- Your paper must use a paper size corresponding to A 4 which is 210 mm (8.27 inch) Wide and 297 mm (11.69 inch)
- Your paper must be in two column format
- Articles not more than 15 pages in length, single-sided A4 paper, margins (top, bottom, left, right) are 1 inch (2.54 cm)
- Abstract and References and content set to double columns,
- English font is Times New Roman, as follows:

TABLE I
Font Sizes for Papers

Content	Font Size	Labelling
Title (Single column)	18 (CT)	bold
Authors (Single column)	11 (CT)	bold
Authors Information (Single column)	10 (CT)	regular
Abstract	10 (LRJ)	bold
Index Terms (Keywords)	10 (LRJ)	bold
Content	10 (LRJ))	regular
Heading1	10 (CT)	regular (Capitalization)
Heading 2	10 (LJ)	regular
Table Title (Place above the Table)	8 (CT)	regular
Table content	8 (CT)	regular
Figure caption (Place below the figure)	8 (LJ)	regular
Reference Head	10 (CT)	regular (Capitalization)
Reference	8 (LJ)	regular
Author Profiles	10 (LRJ)	bold author name/ profile regular

CT=Centre Text, LJ=Left Justified, RJ=Right Justified, LRJ=Left & Right Justified

II. Composition of the Article

A. Article title

B. Authors information, Write (all) the author's name, affiliation, department, city, country and E-mail (set to Single Column) all.

C. Abstract, Must be under 200 words and not include subheadings or citations. Define all symbols used in the abstract. Do not delete the blank line immediately above the abstract.

D. Index Terms, Enter key words or phrases in alphabetical order, separated by commas.

E. Content

1) Academic article, should include: Introduction, Content, and Conclusion.

2) Research article, should include: introduction, literature review, Materials methods, Results, Discussion, and conclusion.

Clearly summarize the important findings of the paper. It should contain such as objectives, methods and major results.

F. Introduction

The Introduction section of reference text expands on the background of the work (some overlap with the Abstract is acceptable). The introduction should not include subheadings.

G. Pictures, table, etc., Must be use in numerical order in the article, provided the source correctly, cannot use other people' copyright.

Chart should be colored contrastingly or in black and white.

H. Reference

1) Cited in the main text. Indicate the number in the [ ] mark at the end of the text or the name of the referring person. Let the numbers be in the same line of content as [1].

2) Cited after the article. Put all bibliographical reference after articles, and order according to the author's name, please refer IEEE format. The footer reference format is as follows.

III. Rererences

References in research articles and scholarly articles. For academic and research journals, INTERNATIONAL SCIENTIFIC JOURNAL OF ENGINEERING AND TECHNOLOGY (ISJET). The technology defines referrals according to the IEEE format. All references should be listed at the end of the paper using the following.

Basic format for books:

J. K. Author, "Title of chapter in the book," in *Title of His Published Book,* xth ed. City of Publisher, Country if not USA: Abbrev. of Publisher, year, ch. x, sec. x, pp. xxx–xxx.

Examples:

[1] G. O. Young, "Synthetic structure of industrial plastics," in *Plastics,* 2nd ed., vol. 3, J. Peters, Ed. New York: McGraw-Hill, 1964, pp. 15-64.

[2] W.-K. Chen, *Linear Networks and Systems.* Belmont, CA: Wadsworth, 1993, pp. 123-135.

Basic format for periodicals:

J. K. Author, "Name of paper," *Abbrev. Title of Periodical*, vol. x, no. x, pp. xxx-xxx, Abbrev. Month. year.

Examples:

[3] J. U. Duncombe, "Infrared navigation—Part I: An assessment of feasibility," *IEEE Trans. Electron Devices*, vol. ED-11, no. 1, pp. 34-39, Jan. 1959.

[4] E. P. Wigner, "Theory of traveling-wave optical laser," *Phys. Rev*., vol. 134, pp. A635-A646, Dec. 1965.

[5] E. H. Miller, "A note on reflector arrays," *IEEE Trans. Antennas Propagat*., to be published.

Basic format for reports:

J. K. Author, "Title of report," Abbrev. Name of Co., City of Co., Abbrev. State, Rep. xxx, year.

Examples:

[6] E. E. Reber, R. L. Michell, and C. J. Carter, "Oxygen absorption in the earth's atmosphere," Aerospace Corp., Los Angeles, CA, Tech. Rep. TR-0200 (4230-46)-3, Nov. 1988.

[7] J. H. Davis and J. R. Cogdell, "Calibration program for the 16-foot antenna," Elect. Eng. Res. Lab., Univ. Texas, Austin, Tech. Memo. NGL-006-69-3, Nov. 15, 1987.

Basic format for handbooks:

Name of Manual/Handbook, x ed., Abbrev. Name of Co., City of Co., Abbrev. State, year, pp. xxx-xxx.

Examples:

[8] *Transmission Systems for Communications*, 3rd ed., Western Electric Co., Winston-Salem, NC, 1985, pp. 44-60.

[9] *Motorola Semiconductor Data Manual*, Motorola Semiconductor Products Inc., Phoenix, AZ, 1989.

Basic format for books (when available online):

Author. (year, month day). *Title.* (edition) [Type of medium]. *volume (issue).* Available: site/path/file

Example:

[10] J. Jones. (1991, May 10). *Networks.* (2nd ed.) [Online]. Available: http://www.atm.com

Basic format for journals (when available online):

Author. (year, month). Title. *Journal.* [Type of medium]. *volume (issue),* pages. Available: site/path/file

Example:

[11] R. J. Vidmar. (1992, Aug.). On the use of atmospheric plasmas as electromagnetic reflectors. *IEEE Trans. Plasma Sci.* [Online]. *21(3),* pp. 876-880. Available: http://www.halcyon.com/pub/journals/21ps03-vidmar

Basic format for papers presented at conferences (when available online):

Author. (year, month). Title. Presented at Conference title. [Type of Medium]. Available: site/path/file

Example:

[12] PROCESS Corp., MA. Intranets: Internet technologies deployed behind the firewall for corporate productivity. Presented at INET96 Annual Meeting. [Online]. Available: http://home.process.com/Intranets/wp2.htp

Basic format for reports and handbooks (when available online):

Author. (year, month). Title. Comp any . City, State or Country. [Type of Medium]. Available: site/path/file

Example:

[13] S. L. Talleen. (1996, Apr.). The Intranet Archi-tecture: M anaging information in the new paradigm. Amdahl Corp., CA. [Online]. Available:http://www.amdahl.com/doc/products/bsg/intra/infra/html

Basic format for computer programs and electronic documents (when available online):

ISO recommends that capitalization follow the accepted practice for the language or script in which the information is given.

Example:

[14] A. Harriman. (1993, June). Compendium of genealogical software. *Humanist.* [Online]. Available e-mail: HUMANIST @NYVM.ORG Message: get GENEALOGY REPORT

Basic format for patents (when available online):

Name of the invention, by inventor's name. (year, month day). *Patent Number* [Type of medium]. Available: site/path/file

Example:

[15] Musical toothbrush with adjustable neck and mirror, by L.M.R. Brooks. (1992, May 19). *Patent D 326 189* [Online]. Available: NEXIS Library: LEXPAT File: DESIGN

Basic format for conference proceedings (published):

J. K. Author, "Title of paper," in *Abbreviated Name of Conf.*, City of Conf., Abbrev. State (if given), year, pp. xxxxxx.

Example:

[16] D. B. Payne and J. R. Stern, "Wavelength-switched pas- sively coupled single-mode optical network," in *Proc. IOOC-ECOC,* 1985, pp. 585-590.

Example for papers presented at conferences (unpublished):

[17] D. Ebehard and E. Voges, "Digital single sideband detection for interferometric sensors," presented at the 2nd Int. Conf. Optical Fiber Sensors, Stuttgart, Germany, Jan. 2-5, 1984.

Basic format for patents:

J. K. Author, "Title of patent," U.S. Patent x xxx xxx, Abbrev. Month. day, year.

Example:

[18] G. Brandli and M. Dick, "Alternating current fed power supply," U.S. Patent 4 084 217, Nov. 4, 1978.

Basic format for theses (M.S.) and dissertations (Ph.D.):

J. K. Author, "Title of thesis," M.S. thesis, Abbrev. Dept., Abbrev. Univ., City of Univ., Abbrev. State, year.

J. K. Author, "Title of dissertation," Ph.D. dissertation, Abbrev. Dept., Abbrev. Univ., City of Univ., Abbrev. State, year.

Examples:

[19] J. O. Williams, "Narrow-band analyzer," Ph.D. dissertation, Dept. Elect. Eng., Harvard Univ., Cambridge, MA, 1993.

[20] N. Kawasaki, "Parametric study of thermal and chemical nonequilibrium nozzle flow," M.S. thesis, Dept. Electron. Eng., Osaka Univ., Osaka, Japan, 1993.

Basic format for the most common types of unpublished references:

J. K. Author, private communication, Abbrev. Month, year.

J. K. Author, "Title of paper," unpublished.

J. K. Author, "Title of paper," to be published.

Examples:

[21] A. Harrison, private communication, May 1995.

[22] B. Smith, "An approach to graphs of linear forms," unpublished.

[23] A. Brahms, "Representation error for real numbers in binary computer arithmetic," IEEE Computer Group Repository, Paper R-67-85.

Basic format for standards:

Title of Standard, Standard number, date.

Examples:

[24] IEEE Criteria for Class IE Electric Systems, IEEE Standard 308, 1969.

[25] Letter Symbols for Quantities, ANSI Standard Y10.5-1968.

First A. Author and the other authors may include biographies at the end of regular papers. Biographies are often not included in conference related papers. The first paragraph may contain a place and/or date of birth (list place, then date). Next, the author's educational background is listed. The degrees should be listed with type of degree in what field, which institution, city, state, and country, and year the degree was earned. The author's major field of study should be lower-cased.

The second paragraph uses the pronoun of the person (he or she) and not the author's last name. It lists military and work experience, including summer and fellowship jobs. Job titles are capitalized. The current job must have a location; previous positions may be listed without one. Information concerning previous publications may be included. Try not to list more than three books or published articles. The format for listing publishers of a book within the biography is: title of book (city, state: publisher name, year) similar to a reference. Current and previous research interests end the paragraph.

The third paragraph begins with the author's title and last name (e.g., Dr. Smith, Prof. Jones, Mr. Kajor, Ms. Hunter). List any memberships in professional societies. Finally, list any awards and work for committees and publications. If a photograph is provided, the biography will be indented around it. The photograph is placed at the top left of the biography, and should be of good quality, professional-looking, and black and white (see above example). Personal hobbies will be deleted from the biography. Following are two examples of an author's biography.

Second B. Author was born in Greenwich Village, New York City, in 1977. He received the B.S. and M.S. degrees in aerospace engineering from the University of Virginia, Charlottesville, in 2001 and the Ph.D. degree in mechanical engineering from Drexel University, Philadelphia, PA, in 2008. From 2001 to 2004, he was a Research Assistant with the Princeton Plasma Physics Laboratory. Since 2009, he has been an Assistant Professor with the Mechanical Engineering Department, Texas A&M University, College Station. He is the author of three books, more than 150 articles, and more than 70 inventions. His research interests include high-pressure and high-density nonthermal plasma discharge processes and applications, microscale plasma discharges, discharges in liquids, spectroscopic diagnostics, plasma propulsion, and innovation plasma applications. He is an Associate Editor of the journal *Earth*, *Moon*, *Planets*, and holds two patents.

Mr. Author was a recipient of the International Association of Geomagnetism and Aeronomy Young Scientist Award for Excellence in 2008, the IEEE Electromagnetic Compatibility Society Best Symposium Paper Award in 2011, and the American Geophysical Union Outstanding Student Paper Award in Fall 2005.

Third C. Author received the B.S. degree in mechanical engineering from National Chung Cheng University, Chiayi, Taiwan, in 2004 and the M.S. degree in mechanical engineering from National Tsing Hua University, Hsinchu, Taiwan, in 2006. He is currently pursuing the Ph.D. degree in mechanical engineering at Texas A&M University, College Station.

From 2008 to 2009, he was a Research Assistant with the Institute of Physics, Academia Sinica, Tapei, Taiwan. His research interest includes the development of surface processing and biological/ medical treatment techniques using nonthermal atmospheric pressure plasmas, fundamental study of plasma sources, and fabrication of micro- or nanostructured surfaces.

Mr. Author's awards and honors include the Frew Fellowship (Australian Academy of Science), the I. I. Rabi Prize (APS), the European Frequency and Time Forum Award, the Carl Zeiss Research Award, the William F. Meggers Award and the Adolph Lomb Medal (OSA).

Remark: More detail information, Pleases read Preparation of Papers for INTERNATIONAL SCIENTIFIC JOURNAL OF ENGINEERING AND TECHNOLOGY (ISJET), https://ph02.tci-thaijo.org/index.php/isjet/index

Panyapiwat Institute of Management (PIM)
85/1 Moo 2, Chaengwattana Rd,
Bang Talat, Pakkred, Nonthaburi 11120, Thailand
Tel. +66 2855 1560
https://www.tci-thaijo.org/index.php/isjet/index
https://isjet.pim.ac.th
E-mail: isjet@pim.ac.th